

# Sperm and Cilia Dynamics

I n a u g u r a l - D i s s e r t a t i o n

zur

Erlangung des Doktorgrades

der Mathematisch-Naturwissenschaftlichen Fakultät

der Universität zu Köln

vorgelegt von

Jens Elgeti

aus Bremen

Köln

2006

Berichterstatter: Prof. Dr. Gerhard Gompper  
Prof. Dr. U. Benjamin Kaupp

Tag der letzten mündlichen Prüfung: 26.02.07

# Contents

<b>1</b>	<b>Introduction</b>	<b>9</b>
1.1	Motivation . . . . .	9
1.2	Axoneme . . . . .	10
1.3	Sperm . . . . .	14
1.4	Cilia . . . . .	18
1.5	Theory . . . . .	22
1.5.1	The Beating Axoneme . . . . .	22
1.5.2	Sperm Motility . . . . .	23
1.5.3	Cilia Dynamics . . . . .	24
<b>2</b>	<b>Method</b>	<b>27</b>
2.1	Molecular Dynamics . . . . .	27
2.2	Mesoscopic Hydrodynamics . . . . .	28
2.2.1	Navier-Stokes equation . . . . .	28
2.2.2	Low Reynolds-Number Hydrodynamics . . . . .	29
2.2.3	Multi Particle Collision Dynamics . . . . .	31
2.2.4	Units . . . . .	34
2.2.5	Thermostat . . . . .	34
2.2.6	Poiseuille Flow . . . . .	35
2.2.7	Partially Driven Flow . . . . .	37
2.2.8	Dimensionless Efficiency . . . . .	38
2.2.9	Rod Friction . . . . .	39
2.3	Sperm Model . . . . .	42
2.3.1	Sperm Structure . . . . .	42
2.3.2	Importance of Asymmetry . . . . .	45
2.3.3	Sperm Simulations without Hydrodynamics . . . . .	46
2.3.4	Rocket Model . . . . .	48
2.4	Cilium . . . . .	48

2.4.1	Cilia Structure . . . . .	48
2.4.2	Control Parameters for Cilia . . . . .	51
2.5	Boundary Conditions . . . . .	52
<b>3</b>	<b>Sperm Results</b>	<b>55</b>
3.1	Important Observables . . . . .	55
3.2	Free Movement . . . . .	56
3.2.1	Simulations with Hydrodynamics . . . . .	56
3.2.2	Simulations without Hydrodynamics . . . . .	62
3.2.3	Discussion . . . . .	67
3.3	Confined Movement . . . . .	67
3.3.1	General Observations . . . . .	68
3.3.2	Surface Adhesion . . . . .	69
3.3.3	Regimes of Motion . . . . .	76
3.3.4	Velocity in Thin Films . . . . .	81
<b>4</b>	<b>Cilia Results</b>	<b>83</b>
4.1	How to Characterize Metachronal Waves . . . . .	83
4.2	Extraction of Metachronal Wave Effects . . . . .	88
4.3	Beat Period . . . . .	88
4.4	Auto-Correlation Function . . . . .	91
4.5	Wavelength . . . . .	93
4.6	Orientation of the Metachronal Wave . . . . .	93
4.7	Correlation Anisotropy . . . . .	94
4.8	Correlation Lengths . . . . .	95
4.9	Transport . . . . .	97
4.10	Orientation of Transport . . . . .	101
4.11	Energy and Efficiency . . . . .	103
4.12	Planar Beating . . . . .	107
4.13	Finite-Size Effects . . . . .	107
4.14	Discussion . . . . .	109
<b>5</b>	<b>Conclusion and Outlook</b>	<b>111</b>
<b>6</b>	<b>Acknowledgments</b>	<b>115</b>

<b>7 Appendix</b>	<b>117</b>
7.1 Parallelization . . . . .	117



# Abstract

Sperm cells are propelled in a fluid by an active, snake-like motion of their tail, the flagellum. It is known for some time that sperm cells accumulate at the walls of a container, swimming mostly in clockwise circles. Cilia are hair-like extensions of some cells that propel fluid over its surface by performing a whip-like motion. Cilia appear in many places in nature, e.g. to remove mucus out from the human respiratory system, or on the surface of swimming *Paramecium*. One of the puzzling phenomena observed in large arrays of cilia, is the metachronal wave; neighboring cilia beat with a certain phase difference that leads to wave-like patterns, similar to those observed when the wind blows over a wheat field. Both structures, the flagellum and the cilium, have a very similar underlying structure, the axoneme. This similarity suggests a combined theoretical study.

We constructed a model axoneme that is used for simulations of sperm and cilia. It is modeled as a semi-flexible polymer, on which an active bending can be imposed. Hydrodynamic interactions, which are responsible for the directed motion of the cell and the metachronal wave of cilia, are taken into account by a particle-based, mesoscopic simulation technique (multi-particle collision dynamics). In sperm simulations, the axoneme is subjected to a sinusoidal bending force. The sperm head is modeled as a sphere, chirally displaced from the beat plane of the tail. Arrays of cilia are modeled by attaching several axoneme models to a wall. The activity is imposed by a geometry-dependent bending force.

We demonstrate that the highly simplified sperm model captures the main features of cell motion described above. We unveil how hydrodynamic interactions lead to adhesion to a wall, and we are able to explain this apparent attraction by a combination of thrust and hydrodynamic repulsion of the tail. Furthermore, we find that the chirality is the cause of the directed circular motion. Tuning this chirality, we find two regimes of motion. In one regime sperm swim in tight circles very close to the wall. Without rotation around the longitudinal axis of

the sperm cell, the beating plane stays perpendicular to the wall. In the other regime, the sperm follows large circles and rotates around its own longitudinal axis. In this case the beating plane is on average parallel to the wall. We explain the transition between these two regimes of motion by a dynamic change of the shape of the flagellum.

For cilia, we present, for the first time, a two-dimensional array of autonomously beating cilia, solely coupled by hydrodynamic interactions, that develop a metachronal wave. We show that the metachronal wave enhances velocity and efficiency of solute transport compared to synchronously beating cilia. The transport velocity increases up to a factor of 3.2, when the cilia are packed more densely, while transport efficiency increases almost an order of magnitude. Furthermore, we characterize transport and wave properties as functions of the viscosity, effective stroke direction and cilia spacing. For example, we show that the main correlation direction roughly coincides with the effective stroke direction, and that the beat frequency decreases through metachronal coordination while the energy consumption per beat is largely independent of cilia spacing, effective stroke direction, and metachronal coordination. We believe, that for the fitness of the cell, both the efficiency and especially the transport velocity are essential. The metachronal wave pattern is thus of great functional significance for ciliated cells.

# 1 Introduction

## 1.1 Motivation

Life, as we see it, is deeply connected to motion. Motion is commonly considered to be a “sign of life”. Movement is important from single cells, to higher organisms. There are many kinds of cell motility:

*Cell crawling*, for example, is used by fibroblasts to move across a surface to repair a wound. White blood cells adhere to the wall of the blood vessel and crawl through tissue to combat an infection. Amoebae crawl across surfaces in their search for food. Typical velocities of crawling cells are on the order of  $10\ \mu\text{m}/\text{s}$ . The basic mechanisms of cell crawling are known [2]. First, the cell pushes filopodia, finger-like extensions, in the forward direction. These filopodia adhere to the surface via adhesion molecules (integrin for example). Thereafter, the cell body is dragged across the surface. How exactly these individual steps are performed, however is subject of ongoing research (see Ref. [72] for a review).

Some bacteria use *rotating flagella* to swim through a fluid to find food; *Escherichia coli* is probably the best-known example. This rod-like bacterium has a bunch of roughly  $20\ \mu\text{m}$  long helical threads connected to motor proteins. When the threads rotate counterclockwise, they form a bundle and act as a propeller that moves the bacterium forward. On the other hand, when the rotation of the flagella is clockwise, *E.coli* starts to tumble and to reorientate. The motor creating the necessary torque [84, 80] and the formation of bundles [70, 48] were examined in recent years.

The bacterial flagella should not be mistaken with the eukaryotic flagella described below. In this work the term flagellum always refers to the eukaryotic flagellum.

Sperm use a *beating flagellum* to swim towards the egg. *Paramecium*, a unicellular organism, is covered by thousands of *beating cilia* to propel it through a fluid. Both, cilia and flagella, are built from an axoneme, which is a very univer-

sal structure throughout the animal kingdom. Sperm tails, propelling hairs on a *Paramecium*, small hairs in the respiratory system and many other examples are all constructed essentially in the same way. Furthermore, flagella are of interest for engineering [50] e.g. for micro machines [18]. For example, Dreyfus et al. [18] constructed a chain of magnetic colloids that are moved by an external field in a sinusoidal pattern, and thus create thrust on an attached red blood cell.

The common axoneme structure, its wide appearance in eukaryotic cells, and its potential for engineering makes the understanding the dynamics of cilia and flagella, the hydrodynamics around them, the propulsive forces and collective phenomena a field of research of fundamental interest. We develop a coarse-grained model with only a few parameters. Using computer simulations, we are able to reproduce and study large-scale phenomena of motility. This will be the theme of this work.

## 1.2 Axoneme

The structure underlying cilia and flagella is called the axoneme. The axoneme is constructed from approximately 250 different proteins [42]. Small differences occur between the axonemes of different organisms, but the basic design is the same, which is the "9+2 Structure". Two central microtubules (stiff polymers, the "bones" of the cytoskeleton) are surrounded by 9 double microtubules (see Fig. 1.1). These microtubules are connected by many proteins to create the appropriate elastic properties. At one end, the doublet microtubules emerge from a basal body (see Fig. 1.1) where they form triplets with another microtubule. Motor proteins (dyneins) cause an active bending of the structure by sliding microtubules along each other. The generation of motion is illustrated in Fig. 1.2.

It is not yet fully understood how these motor proteins are controlled. Several models have been proposed (see Sec. 1.5). The "9+2 structure" is enclosed by an extension of the cell membrane, in contrast to bacterial flagella which are bare protein threads extending from the cell.

In the following, the key components of the axoneme are described in more detail.

- *Microtubules* are long and stiff polymers that are found in several other structural units of a cell. Together with other protein filaments, they form

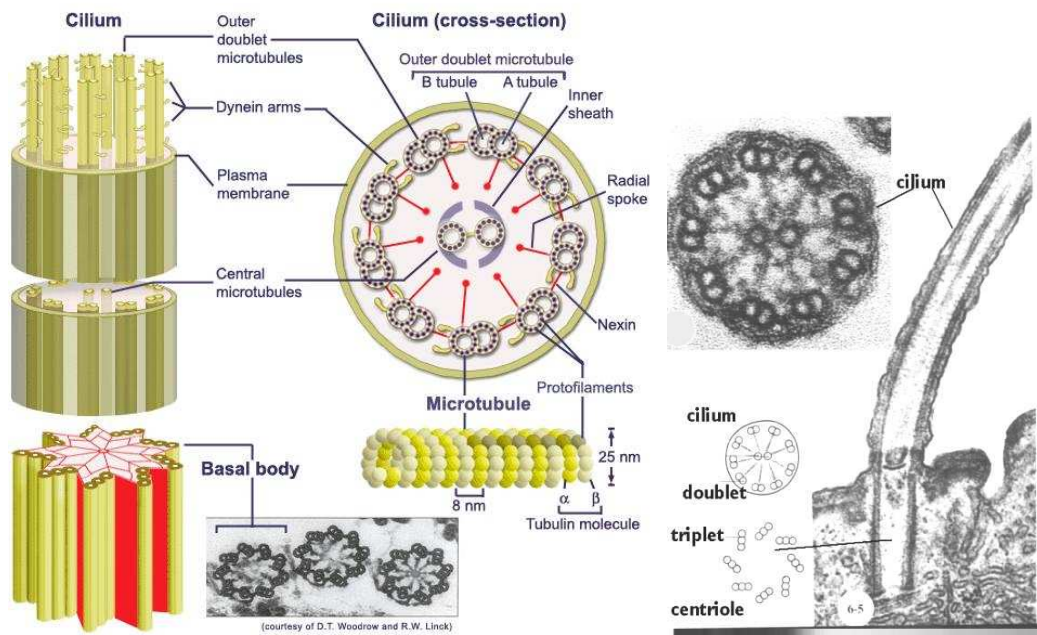


Figure 1.1: Structure of the axoneme

Left: Schematic figure of the axoneme, from <http://www.nyu.edu/classes/ytchang/book/e003.html>

Right: Micrographs of a cilium, from [http://www.cytochemistry.net/Cell-biology/cilia\\_intro.htm](http://www.cytochemistry.net/Cell-biology/cilia_intro.htm)

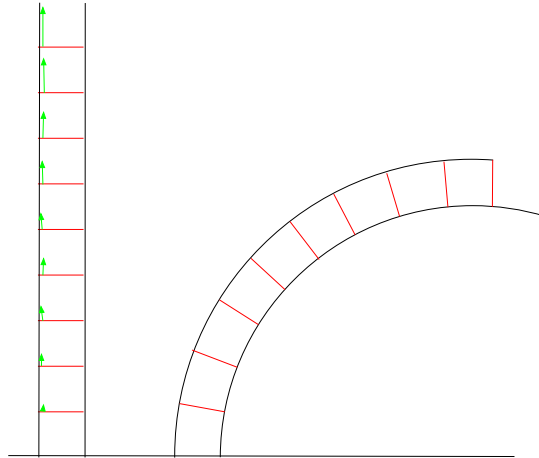


Figure 1.2: *Microtubule sliding leads to bending.* On the left side is a relaxed two dimensional model of the axoneme, in black the two microtubules and in red the motor proteins. The green arrows indicate that the motor proteins will move along the left microtubule upwards about 10% of their current distance from the base. Because the microtubule is attached at the lower end, it is bend as pictured on the right hand side.

the cytoskeleton of the cell. They consist of tubulin monomers that are arranged in a helical fashion to form a hollow tube (see Fig. 1.3). These tubes are about 24 *nm* thick and can be up to millimeters long. Microtubules are rather stiff with a persistence length of several millimeters. Inside a cell, microtubules may be dynamically unstable, constantly polymerizing and depolymerizing. This dynamic instability is used, for example, to form the meiotic spindle [13, 28]. In the axoneme, special proteins keep the microtubules from falling apart. The outer ring of microtubules in the axoneme is formed by doublet microtubules, always two microtubules are interlaced into each other. In a cross section view, doublet microtubules look like three quarters of a circle that is attached to the full circle of a normal microtubule (see the micrograph in Fig. 1.3).

- *Dyneins* are motor proteins that use ATP hydrolysis to move along a microtubule. They are the key active component of the axoneme. More precisely: cilia and flagella have so-called axonemal dyneins that have two different arms extending clockwise from one doublet microtubule to the next.

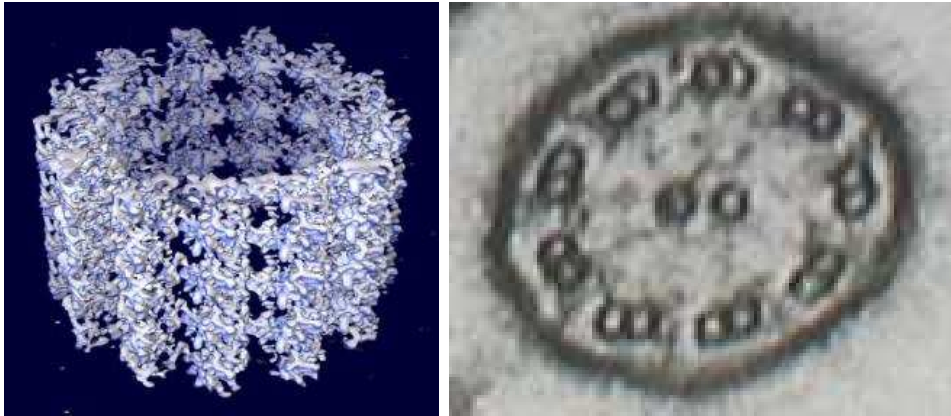


Figure 1.3: Microtubule structure.

Left: 3-D reconstruction of a microtubule from  
<http://en.wikipedia.org/wiki/Microtubule>

Right: An electron micrograph of a cross section of a cilium, from  
[http://www.cytochemistry.net/Cell-biology/cilia\\_intro.htm](http://www.cytochemistry.net/Cell-biology/cilia_intro.htm)

In a cell, a large variety of motor proteins is present to fulfill many different tasks. Motor proteins have been studied intensively in recent years. In a typical experiment, a colloidal particle is attached to one end of the motor protein. In an appropriate solution, the motor proteins run along a microtubule, while a laser tweezer can exert a well-defined force onto the colloid. Thus a velocity versus force measurement is possible [21]. Motor proteins have been described as “Brownian ratchets” [73]. In a spatially periodic yet asymmetric potential, which switches periodically directed motion is possible - even against a net force.

- *Radial spokes* form a class of proteins (about 22 have been identified) that connect the central pair with the outer ring. It is speculated that some of these radial spokes act as regulators for the inner dynein arms [42], but their precise function is still unresolved.
- *Membranes* can self assemble from a solution of amphiphilic molecules. A simple artificial membrane is a lipid bilayer that forms in an aqueous solution by the hydrophobic effect. In cells, membranes are much more complex. Many different kinds of lipids, proteins, glycolipids, cholesterol and other ingredients are embedded into the membrane. A schematic view is shown in Fig. 1.4. In the cell, the main function of membranes is

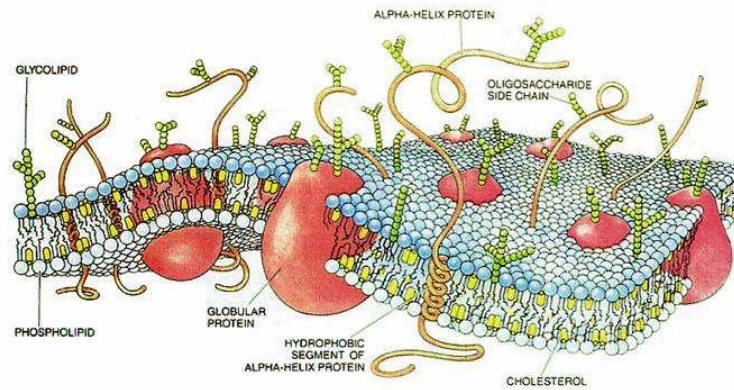


Figure 1.4: Cell Membrane [5].

to provide a barrier between the cytoplasm (the interior of the cell) and the surrounding fluid, but it is also essential for many other processes [2], including ATP synthesis, transport (endocytosis, exocytosis) and adhesion. The membrane seems not to be essential for axoneme dynamics and the generation of flow; Brokaw [7] showed that sperm can swim without a membrane.

- *Many other proteins* and structures can be found in the axoneme. Among others, there are nexin links, protein kinases, fibers, pores, ion channels, receptors etc. Their function varies from beat pattern control and sensory functions to elastic stiffening.

For a more detailed description of the structure of the axoneme, see Ref. [42].

### 1.3 Sperm

Sperm motility has been studied for a long time. Rothschild's review [78] on the sea urchin spermatozoon in 1951 covered the first 27 pages of "Biological Review", while a search for "sperm" in the Web of Science leads to over 50 000 hits. From a physics point of view, the motility of sperm is probably one of the most interesting topics of research. An essay by Brokaw [8] provides a lucid review of the history of sea urchin sperm motility, subtitled "My Favorite Cell".

Although sperm cells from different species look different, they have a similar structure from a theoretical point of view: A long flagellum is attached to a relatively small head (see Fig. 1.5).

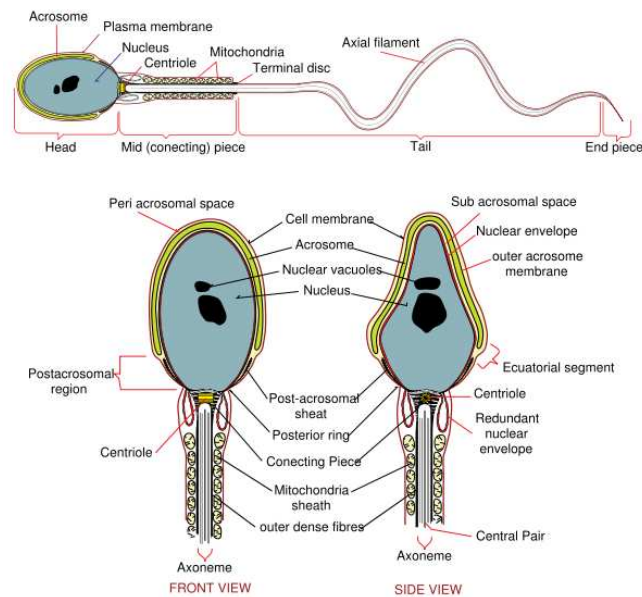


Figure 1.5: Diagram of human sperm,  
from <http://en.wikipedia.org/wiki/Sperm>

Many substructures are present in sperm (see Fig. 1.5). Starting from the tip of the head, called acrosome (used to “dig” into the egg) to the nucleus, where the haploid genetic information is stored, to the flagellum, where in the axoneme many mitochondria are wrapped around the “9+2 structure” to provide ATP as energy source. Chemotaxis, the directed motion in a chemical gradient, is accomplished by a combination of complicated sensory responses involving a cascade of protein-protein interactions. The flagellum is separated into (at least) three parts: the mid piece, the principal piece (which can be subdivided in further pieces), and the end piece.

It is instructive to take a look at the characteristic length scales of, for example, sea urchin sperm [26]. The head appears triangular or conical in shape, about  $3\ \mu\text{m}$  long and  $1\ \mu\text{m}$  thick. The flagellum is much larger; it has a length of roughly  $50\ \mu\text{m}$ . At the surface of the cover slip, the sperm swims with a diameter of  $50\ \mu\text{m}$  [46] (see Fig. 1.6) at a velocity of roughly  $220\ \mu\text{m}/\text{s}$  (although these values depend somewhat on the degree of activity).

Motion of sperm is created by beating of the tail. The beat pattern is, like the overall structure, species-dependent, but on a more global level, the beat patterns are similar [83, 6]. The beat pattern has the form of a traveling bend-

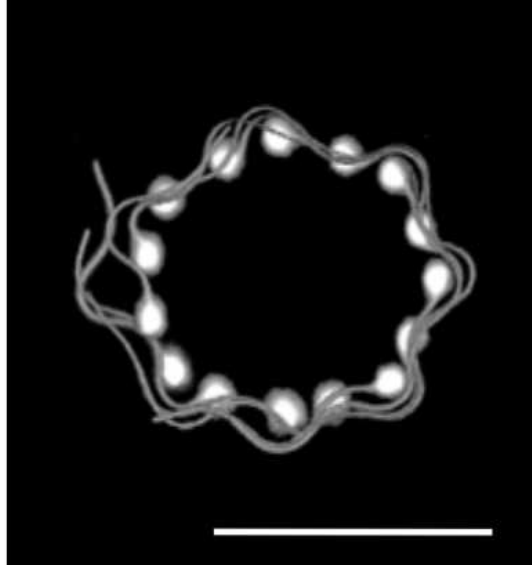


Figure 1.6: Sea urchin sperm, swimming at a surface (from Ref. [46], scale bar is  $50 \mu m$ ).

ing wave, usually from the head to the tip of the tail, but the reverse is also reported. This bending wave can be sinusoidal, but also half circles in opposing directions or meander-like beat patterns have been reported. Typically the flagellum beats essentially in a single plane, although some form of a small aplanar beat component is reported for many species while others might even display an almost helical beat pattern.

In bulk fluid, sperm usually swim on helical trajectories. In confined geometries, like in the droplet between the cover slides under a microscope, surprisingly sperm accumulate at the walls. In 1963, Rothschild [79] observed this phenomenon quantitatively and concluded that some hydrodynamic interactions capture the sperm at the surface. This basic observation is not yet understood.

More recently the problem of sperm adhesion was addressed by Cosson et al. [12] and Woolley [94]. Cosson et al. [12] studied sea urchin sperm using high-speed video microscopy. They observed that parts of the sperm tail close to the surface are out of focus. This was interpreted as an out-of-plane component in the beating pattern. It was further argued that this out-of-plane component generates a force that pushes the sperm towards the surface.

Woolley [94] distinguishes two different forms of surface adhesion of sperm displaying either a planar or a three-dimensional beat pattern. For planar beating sperm, the key observation is the “left-hand rule”: sperm only adhere to a

surface if the left side of the head touches the wall. Woolley assumes that, due to asymmetries, the head acts as a hydrofoil and thereby creates a pressure against the surface in one direction. Sperm with a three-dimensional beat pattern on the other hand adhere if the beating envelope is conically shaped. If one side of the cone is close to the wall, the thrust points towards the surface, thus keeping the sperm at the surface.

Furthermore, once captured at the surface, sperm swim in a circle with a preferred direction of rotation. This circular motion is not just the projection of the helical bulk trajectory. Woolley [94] proposed that the preferred circling direction arises because only one side (“left”) of the head adheres to the surface.

In the case of a three-dimensional beating pattern Woolley argues that, while the sperm is rotating, the head experiences higher viscous friction close to the wall. Thus the resulting forces are turning the sperm in the same direction of its rotation (if observed from the front of the sperm’s head / from outside the observation chamber).

An important question that is beyond of the scope of this work is how chemotaxis induces directed motion of sperm. The group of Kaupp [46, 35, 45, 85] has made significant progress by understanding how binding of a chemical attractant released by the sea urchin egg, leads to changes in the sperm trajectory and thus to chemotaxis. While swimming in circles, the sperm senses the chemoattractant concentration. A calcium influx causes an increase in the curvature of the trajectory after some time delay. Thereafter, the sperm swims straight for a while before swimming in circles again. With the correct match of the velocities and delay times, the sperm is able to swim up gradient, towards the egg.

Although many models that describe the beat pattern of the flagellum have been developed (see Sec. 1.5), no consistent model explaining the different dynamical phenomena on larger length scales has been proposed. In this thesis, we provide a simple model, only considering some basic characteristics of a sperm cell. We are able to reproduce sperm behavior in a qualitative form in bulk fluid as well as in confined geometries. In particular we are able to explain how sperm adhere to a wall due to hydrodynamic repulsion of their tail. Furthermore, our model is flexible enough to implement specific beat patterns and geometries in future studies.

## 1.4 Cilia

Cilia are active hair-like extensions from the cell that can, by performing a whip-like motion, move fluid across the cell surface. They are typically 5-20  $\mu\text{m}$  long and about 250 - 1000  $\text{nm}$  thick.

Probably cilia have already been discovered in 1675 [82] and described as little legs used for propulsion of a unicellular organism. Over the years, more and more details were discovered. Cilia appear in many different forms. For



Figure 1.7: Stentor ciliate, from wikipedia,  
<http://en.wikipedia.org/wiki/stentor%28genus%29>

example *Stentor* (see Fig. 1.7) is a group of filter feeding ciliates named after the Greek herald Stentor due to their trumpet-shaped body. Around the “mouth”, a ring of cilia bundles moves fluid and nutrition inside the body. The *Paramecium* (“Pantoffeltierchen”) is one of the most famous unicellular eukaryotes. Cilia, on

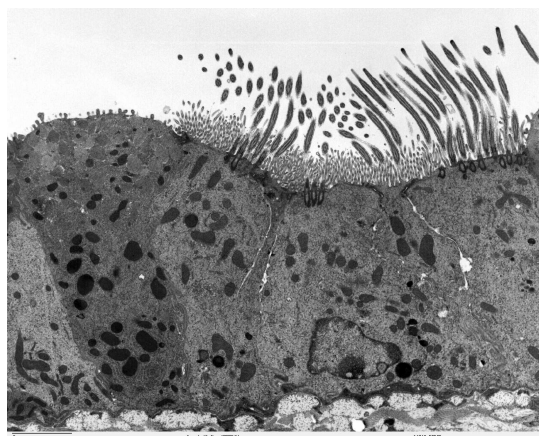


Figure 1.8: Transmission electron microscope image of the lung (mouse). From  
<http://remf.dartmouth.edu/images/mammalianLungTEM/source/12.html>

the surface of *Paramecium* are used for propulsion of the cell through aqueous medium. In the female reproductive tract, the oviduct, large arrays of cilia move the egg. In the lungs of mammals (see Fig. 1.8), cilia propel mucus out of the respiratory system. All these different cilia have a remarkably similar structure, the axoneme. The differences are mainly in size and beating pattern (see Fig. 1.9). While the beat pattern of sperm is relatively symmetric, cilia have clearly distinguishable effective and recovery strokes. The relatively fast effective stroke (also called power stroke) happens in a plane perpendicular to the surface while the cilium is rather straight. In the recovery stroke, the cilium slowly returns back to the initial position, moving more closely at the surface in a plane tilted towards the surface. Due to the asymmetry of this beat pattern, fluid is moved in the effective stroke direction (ESD).

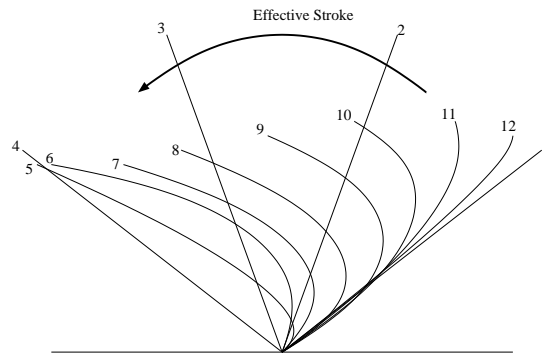


Figure 1.9: Cilium beat pattern, schematic drawing. The effective stroke (1-4) is much faster than the recovery stroke (5-12). Redrawn from [82].

Ciliated cells are often much larger than the cilia itself (see Fig. 1.8). Typically, cilia appear in large arrays. A single organism, like *Paramecium*, is covered by thousands of cilia (see Fig. 1.11). Cilia do not beat randomly or uncoordinated. Instead, they beat in a coordinated wave-like pattern which is called a *metachronal wave* (see Fig. 1.10). The metachronal waves look similar to those when wind blows over a wheat field.

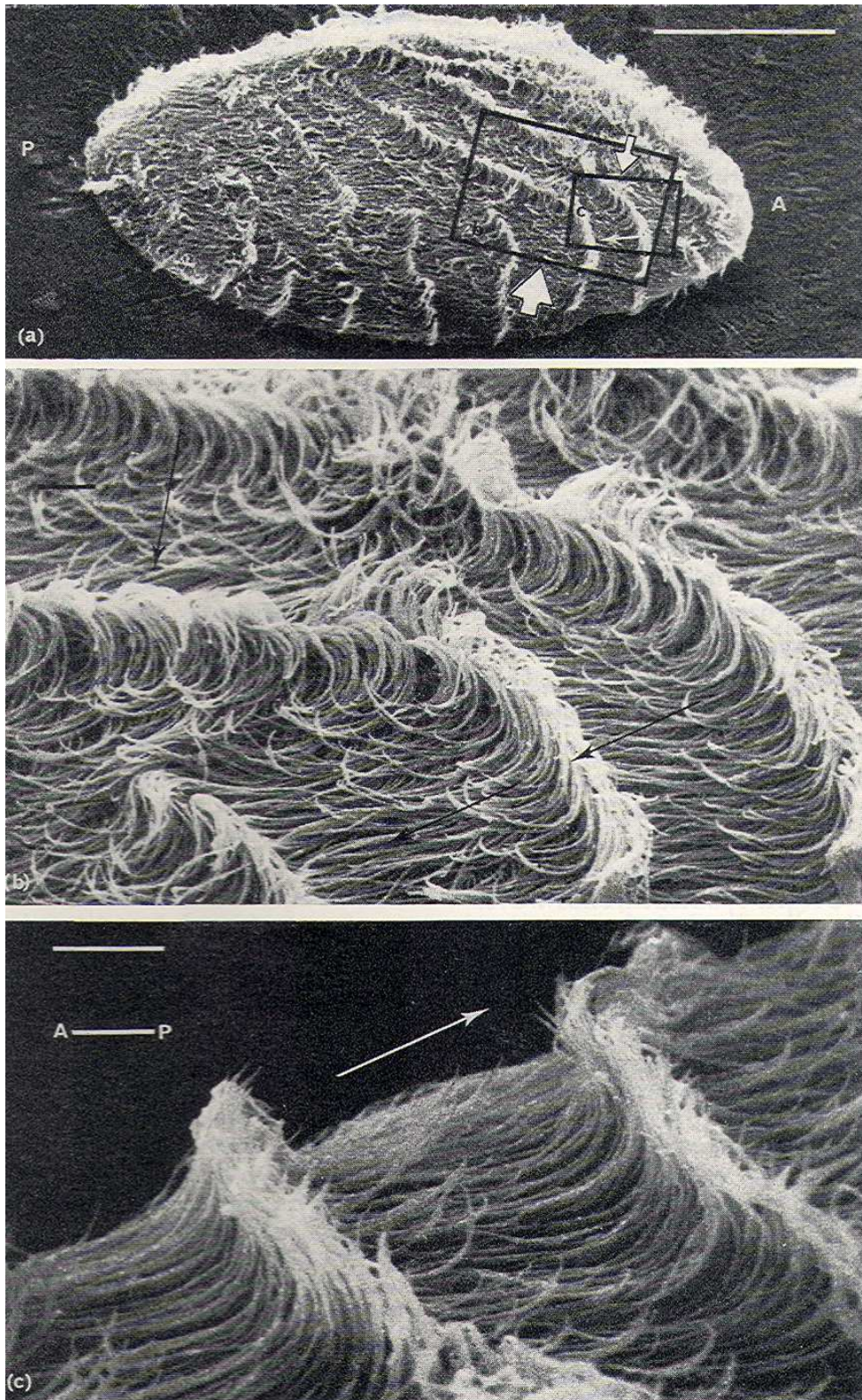


Figure 1.10: Metachronal waves of cilia in *Opalina*, from [86]. (a) Bar= $100\ \mu\text{m}$ , (b) Bar= $10\ \mu\text{m}$ , (c) Bar= $10\ \mu\text{m}$ . Waves travel in the direction of the arrows.

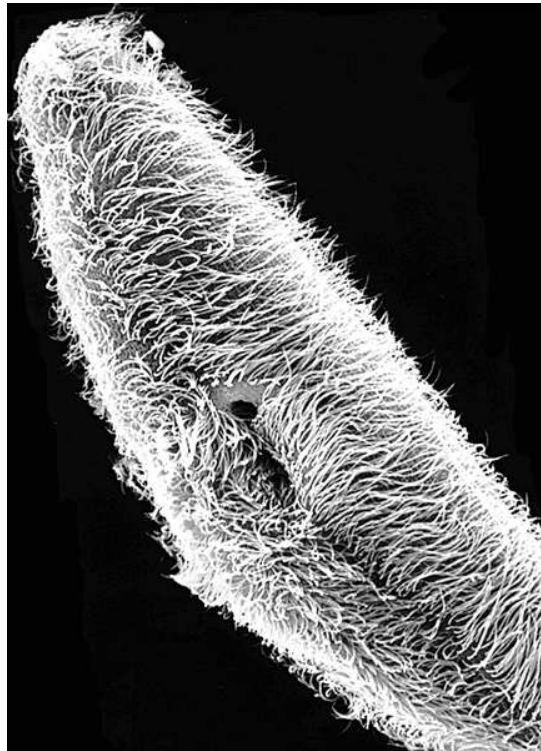


Figure 1.11: Paramecium covered with cilia,  
from <http://www.biomedica.cellbiology.ubc.ca>

The properties of the metachronal wave of the cilia depend strongly on the system. One distinguishes symplectic metachronism where the wave propagates in the direction of the effective stroke, antiplectic metachronism, where the wave travels in the opposite direction, and dexioplectic and laeoplectic metachronism, where it travels perpendicular to the effective stroke [82]. It is known that for certain cilia increased viscosity of the fluid decreases the beat frequency but can also cause erratic behavior [22].

As an example for metachronal waves, consider the work of Gheber et al. [22, 23, 24]. The authors study a monolayer of tissue culture of frog esophagus (the tube that leads from the frog's mouth to the stomach) using optical fibers to get simultaneous data from different points. These mucus propelling cilia are 5-7  $\mu\text{m}$  long and about 600  $\text{nm}$  thick. They beat with about 15 Hz and form a metachronal wave traveling at 90-125° clockwise to the effective stroke direction with a wavelength of 5-9  $\mu\text{m}$ .

## 1.5 Theory

One of the earliest theoretical works on sperm motility is the article by Gray and Hancock (1955) on “The propulsion of sea-urchin spermatozoa” [27]. The propulsive speed of the whole sperm is calculated as a function of the shape and the speed of propagation of the bending waves that are generated by the tail (see Sec. 1.5.2). Several more complex theories have been developed later on. We will discuss a selection in theory of *The Beating Axoneme* (Sec. 1.5.1), *Sperm Motility* (Sec. 1.5.2), and *Cilia Dynamics* (Sec. 1.5.3).

### 1.5.1 The Beating Axoneme

In 1994, Lindemann introduced the “geometric clutch” hypothesis [56]. It has been developed further recently (see for example Ref. [58] and Lindemann’s review [57]). In this model, transverse forces, due to active or passive bending, move adjacent microtubules further apart or closer together. Because in this model the dynein activation probability depends on the distance between the microtubules, a geometrical feedback from the configuration of the axoneme to the active bending force is achieved. Hence the name “geometric clutch”. By adjusting the mechanical properties of the model, different cilia and flagella can be simulated. After further adjustment the model reproduced experiments in which the outer dynein arms were removed, and even predicted two types of arrest behavior that were subsequently experimentally verified.

Brokaw [11] developed a curvature-controlled mechanism for the axoneme. Dyneins are modeled as groups which are switched off whenever the local curvature exceeds a certain preset value. Thereafter, the group on the opposite side is activated. In a series of studies, he was able to describe many different phenomena such as sinusoidal beat patterns of arrest behavior [9, 10, 11]. Both Lindemann [58] and Brokaw [11] implemented hydrodynamics only at the level of an anisotropic friction (see Sec. 1.5.2).

Dillon et al. [16] simulated a two-dimensional axoneme with the immersed boundary method for hydrodynamics. The authors simulated the axoneme as an elastic structure, and dyneins as springs within. The dynein activation is also curvature controlled. The authors do not attempt to reproduce the exact beat pattern of cilia from a specific organism, but define parameter ranges in which beat patterns of both, cilia and flagella, are observed.

The immersed boundary method was introduced by Peskin [68] to model blood

flow in the heart. Here the Navier-Stokes equations are solved numerically on a grid, boundaries are taken into account by  $\delta$ -function forces. The main idea is that the object is modeled by a volume of fluid, and its movement is produced by forces on its surface (see Ref. [69] for details).

Jülicher and Prost [44] showed that competing forces produced by motor proteins lead to instability and oscillations. Hilfinger and Jülicher [36] used this ability of a collection of molecular motors to exhibit spontaneous oscillations [44] and rigorously calculated the dynamics of an actively bending rod [36]. These studies provide a detailed and impressive comparison between theory and experiments on sperm.

To conclude, the overall beat pattern is well reproduced by different models, whereas the details of the beating strongly depend on the individual features of the axoneme. Often the models are able to describe many different beat patterns of different cilia or flagella by small changes in a few parameters.

### 1.5.2 Sperm Motility

Gray and Hancock [27] calculated the swimming velocity of sperm cells. Using the fact that the two friction coefficients for a rod dragged parallel ( $\gamma_{\parallel}$ ) or perpendicular ( $\gamma_{\perp}$ ) to its orientation are different, they calculated the force generated by a moving element of the tail. After assuming a sine-shaped beat-pattern,  $\gamma_{\perp} = 2\gamma_{\parallel}$ , and some other approximations, they calculated the swimming speed as,

$$\bar{v}_x = \frac{\omega\pi b^2}{\lambda} \left( 1 + \frac{4\pi^2 b^2}{\lambda^2} - \sqrt{1 + \frac{2\pi^2 b^2}{\lambda^2} \frac{C_H}{n\lambda\gamma_{\parallel}}} \right)^{-1} \quad (1.1)$$

where  $\omega$  is the angular frequency,  $\lambda$  the wavelength and  $b$  the amplitude of the beat. The number of waves present on the tail is denoted by  $n$ ,  $C_H$  is the drag coefficient of the head. For a spherical head of radius  $a$  and a thin tail of radius  $d$ , it is possible to approximate

$$\frac{C_H}{\gamma_{\parallel}} = 3a \left[ \left( \log \frac{d}{2\lambda} \right) + \frac{1}{2} \right]. \quad (1.2)$$

Because a pre-defined beat shape has been used, the viscosity  $\eta$  does not influence the swimming speed.

Fauci and McDonald [20] simulated a two-dimensional sperm in thin films with the immersed boundary method. They conclude that the sperm's swimming

speed is inversely proportional to the width of the film  $d$ ,

$$\bar{v}_x = \frac{1}{A\left(\frac{d}{b}\right) + B} \quad (1.3)$$

where  $b$  is the beat amplitude and  $A$  and  $B$  are constants. They also observe an effective attraction to the wall. The results strongly depend on the dimensionality. In three dimensions, the fluid can flow around a slender filament, whereas in two dimensions it is confined to one side.

### 1.5.3 Cilia Dynamics

Netz and coworkers [49, 62] studied a cilia-related model in form of an elastic rod. In the study by Netz and Manghi [62], the rod is grafted to a rotary motor. Due to the hydrodynamic drag the rod bends and thus creates a flow away from the plane to which it is attached.

The study by Kim and Netz [49] is more closely related to cilia. The rods are attached to an angular motor. During the effective stroke, a rather weak torque forces the rod to move in one direction while its shape is essentially a straight rod. The high torque during the recovery stroke bends the rod, and thus less fluid is transported than during the effective stroke. This is in contrast to the biological situation, but it might be helpful for engineering of micropumps.

Kim and Netz [49] define a dimensionless efficiency

$$\epsilon = (D/a)/(E/k_bT) = (\bar{v}/a)/(\partial_t E/k_bT) \quad (1.4)$$

where  $D$  and  $E$  are the pumping distance and energy per beat cycle, respectively, and  $a$  is the rod diameter. They find a line of highest efficiency in the persistence-length versus torque parameter space.

Jülicher and Vilfan [91] presented a model where a cilium is represented by a single sphere on a tilted elliptical path near a planar surface. The sphere is driven by a predefined tangential force while hydrodynamic interactions are taken into account by Oseen tensor calculations. Because wall friction reduces the amount of pumped fluid when the sphere is closer to the wall, a net fluid flow results. Modeling two cilia, they were able to identify areas in parameter space where synchronization occurs and calculate the phase lag explicitly.

Lagomarsino, Jona and Bassetti [51] simplified the cilium to a *rower*. A rower can be considered as a point particle with a power and recovery stroke. In the effective stroke, its hydrodynamic drag coefficient is increased and the potential

is switched to move the particle in another direction compared to the recovery stroke. This way the rowers can generate a net flow. A geometric feedback is achieved by switching between the two strokes when a certain displacement is reached. Hydrodynamic interactions are modeled by the Oseen tensor, but no walls are taken into account. The hydrodynamic interactions and the geometric feedback together allow a coupling and synchronization of the rowers. In the continuum limit, in which the model can be studied analytically, the authors only find a stable metachronal wave if the hydrodynamic interaction is negative (i.e. hydrodynamic forces are attractive). But in simulations they find also short-wavelength traveling wave packets where neighbors beat in an anti-correlated fashion.

Gueron and Levit-Gurevich [32, 33, 31, 30] modeled the cilium as a slender, elastic filament. Switching between effective and recovery strokes is defined by the curvature of the cilium. Hydrodynamic interactions are taken into account by a slender body theory [34], which in turn incorporates hydrodynamics with a Oseen tensor approximation. In two dimensional studies [30], where all movement is restricted to one plane, they find an antiplectic metachronal wave; the beat frequency decreases with increasing viscosity and distance between cilia. Furthermore they calculated the energy expenditure per effective stroke to be  $9 \cdot 10^{-16}$  J which decreases to  $3 \cdot 10^{-16}$  J for 100 densely packed cilia in a row. During the recovery stroke the energy expenditure is  $2 \cdot 10^{-16}$  J [31], independent of the number of cilia. The three-dimensional model also includes effects of ATP concentration [32], but the cilium is not allowed to twist. Simulations of  $5 \times 5$  cilia arrays show a metachronal pattern, but a detailed analysis of the metachronal wave was not presented. In the most recent model [33], a twist of the cilium is introduced and singularities in the equations of motion are removed. This model has not yet been used to study cilia dynamics systematically.



## 2 Method

Our goal is to find a rather universal model to simulate the large scale dynamics of flagella and cilia. The beat pattern is treated as an input parameter, and we study the large scale dynamics resulting from it. We do not simulate flagellar beating on a molecular level, but prefer a coarse grained description. Therefore, we treat the axoneme as an active crane-like polymer and the fluid around it with the mesoscale simulation technique MPCD. Details, like the beat pattern, axoneme length, boundary interaction, etc. can be subsequently adjusted to the specific system or model.

### 2.1 Molecular Dynamics

In a coarse-grained description, a group of atoms is represented by a bead or monomer, a point particle with a certain mass and well defined interactions. The movement of this particle is treated classically, i.e. it follows Newton's equations of motion,

$$m_i \frac{d^2}{dt^2} \vec{r}_i = \vec{F}_i. \quad (2.1)$$

where  $m_i$ ,  $\vec{r}_i$  and  $\vec{F}_i$  are the mass, position, and force of monomer  $i$  respectively, and  $t$  denotes the time. In molecular dynamics, these equations are solved in discrete time steps. The straightforward discretization (known as the Euler algorithm) is known to be inefficient. Very small time steps are needed to get reasonably accurate results. Many algorithms have been proposed with different success. Here we use the well established Velocity Verlet Algorithm. Velocities and particle positions are updated according to the rule (see for example Ref. [4]):

$$\vec{r}_i(t + \Delta t) = \vec{r}_i(t) + \vec{v}_i(t)\Delta t + \frac{\Delta t^2}{2m_i} \vec{F}_i(t) \quad (2.2)$$

$$\vec{v}_i(t + \Delta t) = \vec{v}_i(t) + \left( \vec{F}_i(t) + \vec{F}_i(t + \Delta t) \right) \frac{\Delta t}{2m_i}. \quad (2.3)$$

This algorithm has proven to be rather stable and efficient. Its main advantage is the time reversal symmetry and accuracy of  $O(\Delta t^4)$ . The time step  $\Delta t$  has to be sufficiently small to guarantee energy conservation. In our simulation, energy conservation is not so critical, because we couple the system to a heat bath thus long term energy stability is not as critical. The time step  $\Delta t$  must be small enough to allow correct integration of Newton's equations. We used  $\Delta t = 0.001$  in most simulations presented here, and used the energy fluctuations of the molecular dynamics to ascertain that the time step is sufficiently small.

## 2.2 Mesoscopic Hydrodynamics

Hydrodynamic interactions are forces mediated by a surrounding fluid (or gas, then also called aerodynamics). In principle they arise from the movements of fluid particles and their interactions. We encounter them frequently in every day life. Whether it is wind slowing down a cyclist, pumping of the heart, water sprinkling from the garden hose or birds flying in the air, its all hydrodynamics. In many biological systems hydrodynamics play an important rule, and is essential in this work.

### 2.2.1 Navier-Stokes equation

The macroscopic hydrodynamics have been intensively studied on the basis of the Navier-Stokes equation<sup>1</sup> [54]:

$$\rho \frac{\partial \vec{v}}{\partial t} + \rho(\vec{v}\vec{\nabla})\vec{v} = \eta \nabla^2 \vec{v} - \nabla p + \vec{f}_{ext} \quad (2.4)$$

where  $\rho$  and  $\vec{v}$  are the fluid density and velocity field.  $p$  is the pressure and  $\vec{f}_{ext}$  is the external force density. The Navier-Stokes equation is derived explicitly from the standard Newtonian equations of motion, assuming that different "fluid particles" moving beside each other experience friction depending on the velocity gradient and the viscosity  $\eta$  (the "friction coefficient" of the fluid). Together with the continuity equation these equations fully determine the flow of an isothermal incompressible fluid. Thermal fluctuations however are not included.

---

<sup>1</sup>for incompressible flow and without thermal fluctuations

By rescaling with a typical length scale  $l$  and velocity scale  $u$ ,

$$\begin{aligned} t' &= tv/l \\ v' &= v/u & x' &= x/l \\ p' &= \frac{lp}{\eta u} & f' &= \frac{l^2 f}{\eta u} \end{aligned}$$

the Navier-Stokes equation can be rewritten to a dimensionless form.

$$\Re \left( \frac{\partial \vec{v}}{\partial t} + (\vec{v} \vec{\nabla}) \vec{v} \right) = \nabla^2 \vec{v} - \nabla p + \vec{f}_{ext} \quad (2.5)$$

The primes ' have been omitted for simplicity. The dimensionless Reynolds number

$$\Re = \frac{\rho ul}{\eta} \quad (2.6)$$

describes the ratio between viscous and inertia forces. It is an important parameter to characterize the type of flow; if the boundary conditions and the Reynolds number are the same, the flows are similar. The higher the Reynolds number, the more important are the kinetic, nonlinear terms, therefore the transition to turbulence is characterized by a system-specific Reynolds number.

Solving the Navier-Stokes equation for complex fluids and biological systems can be nearly impossible because of the complications that arise from coupling the Navier-Stokes equation to the immersed particles and complex boundary conditions. Thus other approaches are needed.

### 2.2.2 Low Reynolds-Number Hydrodynamics

In typical mesoscale systems, length scales are in the order of micrometers, velocities in the order of a few hundred  $\mu m$  per second. With the viscosity of water of 0.001 kg/ms, the Reynolds number is in the order of  $10^{-4}$ . Thus the kinetic term  $\left( \frac{\partial \vec{v}}{\partial t} + (\vec{v} \vec{\nabla}) \vec{v} \right)$  in eq.(2.4) can be omitted, which simplifies the Navier-Stokes equation to the Stokes equation (or creeping flow equation):

$$\vec{\nabla} p - \eta \nabla^2 \vec{v} = \vec{f}_{ext} \quad (2.7)$$

Because the equation is now linear, solutions can be superimposed. The Oseen tensor  $\mathfrak{T}$  and the pressure vector  $\vec{g}$  are the Green's functions for the creeping flow

equation (2.7). If the Oseen tensor is known, the velocity field can be calculated via

$$\vec{v}(\vec{r}) = \int \mathfrak{T}(\vec{r} - \vec{r}') \vec{f}_{ext}(\vec{r}') d\vec{r}' \quad (2.8)$$

and the pressure via,

$$p(r) = \int \vec{g}(\vec{r} - \vec{r}') \cdot \vec{f}_{ext}(\vec{r}') d\vec{r}'. \quad (2.9)$$

For the bulk fluid, and for a single wall, the Oseen tensor is known. The explicit expression for the bulk fluid Oseen tensor [15]

$$\mathfrak{T}(\vec{r}) = \frac{1}{8\pi\eta r} \left( \mathbf{1} + \frac{\vec{r} \otimes \vec{r}}{r^2} \right) \quad (2.10)$$

shows the long range  $1/r$  dependence of hydrodynamic interactions. (Here  $\otimes$  represents the dyadic product, the result is therefore a tensor with the components  $(\vec{r} \otimes \vec{r})_{ij} = r_i r_j$ .) Thermal fluctuations can be included for Brownian dynamics simulations [64], but require the inversion of the Oseen tensor to satisfy the fluctuation-dissipation relation. This approach is widely used in many mesoscale hydrodynamic simulations.

But also Oseen tensor calculations have their disadvantages. The main disadvantage is that, computation times due to the matrix inversion are of the order  $N^3$  (where  $N$  is the number of beads) which limits Brownian dynamics simulations with Oseen tensor hydrodynamics to date to a few hundred particles. Because we want to model large arrays of cilia, and probably several interacting sperm, we used a more suited algorithm presented below.

In order to overcome such problems, many mesoscopic simulation techniques have been developed. Here a distinction can be made between lattice methods (e.g. Lattice Boltzman [63, 52]) and continuum methods (dissipative particle dynamics (DPD) [37, 19, 29], MPCD (as introduced below) and others, see Ref. [74] for an instructive description). Without going into detail of the advantages and disadvantages of all these methods, we will explain our method of choice, multi particle collision dynamics (MPCD). Its main advantages are explicit local energy and momentum conservation, straightforward coupling to immersed objects, easy implementation of complex boundary conditions and computational efficiency.

On the other end of the description of complex systems are atomistic simulations with explicit solvent. However, due to the size of micro biological systems,

typically several  $\mu m$ , the number of particles ( $10^{10} - 10^{16}$ ) makes this impossible. Atomistic simulations can be a good option for smaller length scales.

### 2.2.3 Multi Particle Collision Dynamics

Multi-particle collision dynamics (MPCD) was introduced by Malevanets and Kapral in 1999 [60]. MPCD is a particle-based off-lattice method to simulate a hydrodynamic solvent.

The fluid is represented by a number  $n$  of point particles with positions  $r_i$  and velocities  $v_i$  that vary continuously in phase space. The dynamics of these particles evolve in two steps:

- The streaming step, in which particles propagate freely according to their velocities for a collision time step  $h$

$$\vec{r}_i(t+h) = \vec{r}_i(t) + h\vec{v}_i(t). \quad (2.11)$$

- The collision step, where the particles are sorted into boxes and their relative velocities to the center of mass are rotated in a random direction by a preset angle,

$$\vec{v}_i(t+h) = \vec{v}_{cm}(t) + \mathfrak{R}(\vec{v}_i(t) - \vec{v}_{cm}(t)), \quad (2.12)$$

where  $\mathfrak{R}$  is the random rotation matrix and  $v_{cm}$  is the center of mass velocity of the box containing particle  $i$ . The box lattice constant is called  $a$ .

The random rotation matrix rotates a vector by a constant angle  $\alpha$  around a random direction. This direction can either be chosen randomly from one of the six coordinate axes (this work) or from the surface of the unit sphere. Both lead to very similar transport coefficients [90]. Ripoll, Mussawisade, Winkler and Gompper [75, 76] showed that  $\alpha \approx 130^\circ$  in combination with a small time step  $h$  leads to high Schmidt numbers (the ratio between viscous and diffusive momentum transport), i.e. fluid-like behavior. Thus we chose  $\alpha = 130^\circ$  in all our MPCD simulations.

From the algorithm, we see that energy and momentum are conserved. The streaming step obviously does not change either momentum or energy. The same

can be shown for the collision step by a short calculation. For the momentum in each box:

$$\vec{P}(t+h) = \sum_{i \text{ in box}} m_i \vec{v}_i(t+h) \quad (2.13)$$

$$= \sum_{i \text{ in box}} m_i \left[ \vec{v}_{cm}(t) + \mathfrak{R}(\vec{v}_i(t) - \vec{v}_{cm}(t)) \right] \quad (2.14)$$

$$= \sum_{i \text{ in box}} m_i \vec{v}_{cm}(t) + \underbrace{\mathfrak{R} \sum_{i \text{ in box}} m_i (\vec{v}_i(t) - \vec{v}_{cm}(t))}_{=0} \quad (2.15)$$

$$= \vec{P}(t) \quad (2.16)$$

Similarly, we can deduce the energy  $E$  conservation:

$$E(t+h) = \sum_{i \text{ in box}} \frac{m_i}{2} v_i^2(t+h) \quad (2.17)$$

$$= \sum_{i \text{ in box}} \frac{m_i}{2} (v_{cm}(t) + \mathfrak{R}(v_i(t) - v_{cm}(t)))^2 \quad (2.18)$$

$$(2.19)$$

using the orthogonality of  $\mathfrak{R}$

$$E(t+h) = \sum_{i \text{ in box}} \frac{m_i}{2} v_i(t)^2 \quad (2.20)$$

$$= E(t) \quad (2.21)$$

The collision step, being on a lattice, breaks Galilean invariance. Translational symmetry is via the Noether theorem connected to Galilean invariance, but the lattice breaks this symmetry. Another way to phrase this is that two particles, being in the same box in one frame of reference, are in a different box in a different frame of reference. To restore symmetry, and thus Galilean invariance, Ihle and Kroll [39] introduced a “random shift” - a displacement of the grid of collision boxes by a random vector where each component is chosen from the interval  $[0, a)$ . Thus for the two particles to be in different boxes due to motion relative to the lattice just resembles a different result in drawing the random vector. Ihle and Kroll proved in Ref. [40] that this addition restores Galilean invariance to the MPCD algorithm.

For the implementation of walls, i.e. no-slip boundary conditions, particles are bounced back, i.e. their velocity is inverted when they hit a wall. However

this procedure is not sufficient to create no-slip boundary conditions [53]. The wall has to be considered in the collision step as well. If the wall cuts a box in half, only half as many particles are inside the box on average. During the collision step, these particles should somehow collide with some of the particles of the wall. This can be done in the following way:

If during the collision step boundary cells are only partially filled (i.e. the number of particles in the cell  $\rho(i)$  is less than the average number of particles  $\rho$  in the cell), virtual particles are added. Because the wall particles should have a finite temperature, these virtual particles have Gaussian distributed velocities (i.e. energies distributed according to a Maxwell-Boltzmann distribution) and are generated independently for each step. Because the sum of Gaussians is again a Gaussian distribution this can be simplified by adding a random vector whose components are drawn from a Gaussian distribution of zero average and variance  $(\rho(i) - \rho)k_B T$ . This scheme, introduced by Lamura, Gompper, Ihle and Kroll [53], has proven to provide nearly perfect no-slip walls.

The viscosity can be calculated analytically with a molecular-chaos assumption [47, 41, 90],

$$\eta = \eta_{coll} + \eta_{kin} \quad (2.22)$$

$$\eta_{coll} = \frac{m(1 - \cos \alpha)}{18ha}(\rho - 1) \quad (2.23)$$

$$\eta_{kin} = \frac{k_B T h \rho}{a^3} \left( \frac{5\rho}{(4 - 2 \cos(\alpha) - 2 \cos(2\alpha))(\rho - 1)} - \frac{1}{2} \right), \quad (2.24)$$

where  $\eta_{coll}$  is the collisional, and  $\eta_{kin}$  the kinetic contribution to the total viscosity. These analytic expressions allow to test the implementation of the algorithm. Besides checking the obvious conservation of energy and momentum, the viscosity can be measured. We perform this test in the Poiseuille flow (see Sec. 2.2.6). For a more detailed description of the method see e.g. Refs. [93, 76].

*Coupling of the fluid* to polymers or other immersed particles is straightforward. Polymers, modeled on a coarse-grained level by monomer beads connected by harmonic springs, are simulated by standard molecular dynamics described above. The polymers can be coupled readily to the MPCD fluid by including the monomers in the collision step [61]. This has been shown [93, 76] to reproduce the hydrodynamic behavior of polymers as described by Zimm dynamics.

Furthermore, with MPCD hydrodynamics can be turned off and on easily. This is useful to extract the effects of hydrodynamics in a given system. *Simulations without hydrodynamics* are performed by assigning each monomer an

individual collision box. Within each of these collision boxes are  $\rho$  particles with Gaussian distributed velocities similar to the virtual particles used for no-slip walls. The collision step and the molecular dynamics for the monomers are not altered. With this scheme, hydrodynamic interactions are not present, but the thermodynamic properties are the similar. Thus, we are able to simulate the same systems with and without hydrodynamics.

Because its introduction in 1999 [60], MPCD has been successfully applied to study different physical systems. Ripoll, Winkler and Gompper examined the behavior of star polymers in shear flow [77], and together with Mussawisade they studied rod-like colloids in shear flow [92]. Noguchi and Gompper used MPCD to investigate vesicles in shear flow [65] and red blood cells in capillary flows [66]. Ali, Marenduzzo and Yeomans applied MPCD to the packing of polymers in viral capsids [3]. To analyze the influence of hydrodynamics on sedimentation of colloids, Padding and Louis [67] also used MPCD. Tucci and Kapral expanded the method to study reaction-diffusion fronts [88]. The group of Ohashi extended MPCD to multiphase fluids [43] and ternary amphiphilic fluids [81]. To describe a fluid with a non-ideal equation of state, MPCD was expanded by Tüzel, Ihle, and Kroll [89].

### 2.2.4 Units

For convenience, we rescaled time and distances to dimensionless units via  $x' = x/a$  and  $t' = t\sqrt{k_bT/ma^2}$ . This is equivalent to choosing  $a = 1$ ,  $k_B T = 1$ ,  $m = 1$ , resulting in the mean free path  $\lambda_p = h\sqrt{k_bT/m} = h$ . All simulation results will be given in these dimensionless units.

The dynamic regimes of the MPCD fluid depends on the input parameters, especially the rotation angle  $\alpha$ , the particle density  $\rho$  and the collision time  $h$ . We choose  $\alpha = 130^\circ$ ,  $0.01 \leq h \leq 0.1$ , and  $\rho = 10$ , because it has been shown [76] that this leads to fluid-like behavior.

### 2.2.5 Thermostat

The computational advantage of MPCD arises from the reduced number of degrees of freedom; however, this causes a lower heat capacity. Thus, a relatively small energy input can lead to a large temperature increase. To avoid this problem, we couple the particles to a heat bath.

In spatially homogeneous simulations, like the one for sperm, we simply rescale the velocities by a global factor, so that

$$\vec{v}_i \rightarrow \vec{v}_i \sqrt{T_0/T} \quad (2.25)$$

where  $T_0$  is the desired temperature,  $T$  the calculated temperature of the system, defined by (in 3 dimensions)

$$k_B T = \frac{2}{3N} \sum_i \frac{m_i}{2} v_i^2. \quad (2.26)$$

The simulations of beating cilia produce a relatively constant input of energy to some parts of the total fluid. A global thermostat would thus lead to an unphysical temperature and density gradient. This problem can be avoided by applying a layered thermostat. The velocities are rescaled as above, but the temperature is determined independently for each fluid layer. Typically the temperature rescaling is done after a few collision steps, such that the temperature increases no more than a few percent between the rescaling.

### 2.2.6 Poiseuille Flow

As an example for a MPCD simulation, we consider Poiseuille flow. Between two infinite parallel plates (at  $z = d/2$  and  $z = -d/2$ ) with distance  $d$ , a stationary flow follows a constant pressure gradient  $\partial_x p = -\rho g$  in  $x$  direction, where  $g = -\partial_x p / \rho$  is the acceleration due to the pressure gradient.  $g$  can be considered as a gravitational field providing the pressure gradient. The flow can be calculated analytically assuming stationary, non-turbulent flow.

For the analytical solution, we use the Navier-Stokes equation (2.4) and thus neglect thermal and density fluctuations. In a stationary flow,  $\frac{\partial \vec{v}}{\partial t} = 0$ . Due to symmetry, all velocity components in  $y$  and  $z$  direction are vanishing. Also due to symmetry,  $v_x$  only depends on the distance from the wall  $\vec{v} = v_x(z)$ . Thus

$$(\vec{v} \cdot \vec{\nabla}) \vec{v} = v_x \partial_x v_x = 0 \quad (2.27)$$

This simplifies the Navier-Stokes equation (2.4) to

$$\eta \Delta v_x = \partial_x p \quad (2.28)$$

The solution is a parabolic flow profile

$$v_x(z) = \frac{\rho g}{2\eta} \left( \left( \frac{d}{2} \right)^2 - z^2 \right) \quad (2.29)$$

where the origin is located in the middle between the plates in the  $x - y$  plane. Thus, the flow profile of the Poiseuille flow can be used to determine the viscosity.

Figure 2.1 shows a plot of the velocity profile measured in a simulation with a fitted parabolic flow profile (fit to Eq. (2.29) via  $\eta$  and  $d$ ). Even with virtual particles, there is still a small slip at the walls. This small slip is also visible in Fig. 2.1; for determining viscosity, the slip has to be taken into account by allowing to fit via the channel width  $d$ . In Fig. 2.2 we compare the resulting viscosity  $\eta$  (as a function of the time step  $h$ ), with the theoretical prediction of Eq.(2.22). It is noteworthy, that the excellent match between theory and simulation results was obtained without adjusting parameters.

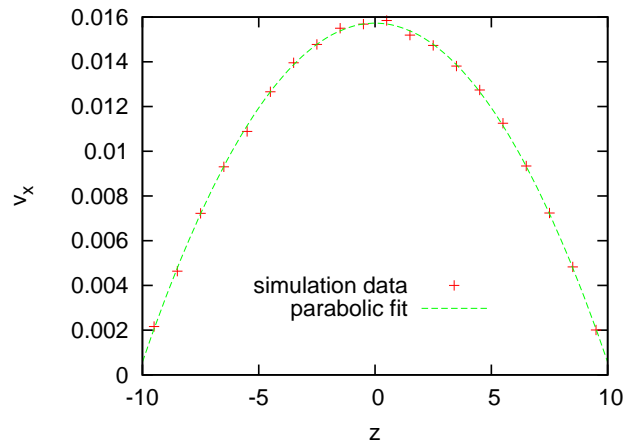


Figure 2.1:  $v_x$  as a function of  $z$  for the Poiseuille flow. Simulation performed with a system size of  $20^3$  boxes,  $\rho = 10$ ,  $h = 0.05$ ,  $g = 0.005$ .

From Eq.(2.29) further quantities can be calculated and compared with the simulation. We will use these quantities when studying fluid transport by cilia. The average velocity  $\bar{v}$  in  $x$  direction in the channel is

$$\bar{v} = \frac{1}{d/2} \int_0^{d/2} v(z) dz = \frac{\rho g}{12\eta} d^2 = \frac{f_x}{12\eta} d^2. \quad (2.30)$$

where  $f_x = \rho g$  as the  $x$ -component of the force density  $\vec{f}$ . The power consumption  $P$  per volume can be obtained as

$$P = \int \vec{f} \cdot \vec{v} dV. \quad (2.31)$$

$$\Rightarrow \frac{1}{V} P = \frac{1}{V} \int \vec{f}(\vec{r}) \vec{v}(\vec{r}) dV = \frac{\vec{f}}{d} \int_0^d \vec{v}(z) dz = 12\eta \bar{v}^2 d^{-2} \quad (2.32)$$

Eqs.(2.30) and (2.32) also agree well with simulation results (not shown).

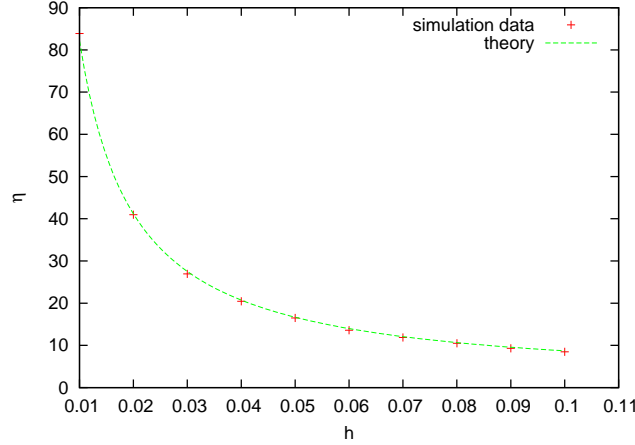


Figure 2.2: Viscosity  $\eta$  as a function of the time step. System size is  $20^3$  boxes,  $g = 0.005$ , theory is a plot of eq.(2.22), without fitting parameters.

### 2.2.7 Partially Driven Flow

As another example, we consider a flow that is a more realistic model of the flow generated by beating cilia. In this flow between walls at  $z = 0$  and  $z = d$ , the fluid is only accelerated in a layer at the bottom (and again only in  $x$ -direction), i.e.  $f_{ext}(z) = g \Theta(d_a - z)$ , where  $\Theta(x)$  is the Heaviside function and  $d_a$  is the width of the acceleration layer. The idea is that the cilia at the bottom of the fluid film propel the fluid, while the layer above just drags along, thus  $d_a$  can be interpreted as the cilia length.

Making the same assumptions as for the Poiseuille flow, we can simplify the Navier-Stokes equation to

$$\eta \partial_z^2 v_x = -f_{ext} = -g \Theta(d_a - z) \quad (2.33)$$

Integration leads to

$$\partial_z v_x(z) = \frac{-g}{\eta} [(z - d_a) \Theta(d_a - z) + C_1] \quad (2.34)$$

$$v_x(z) = \frac{-g}{\eta} \left[ \frac{(z - d_a)^2}{2} \Theta(d_a - z) + C_1 z + C_2 \right] \quad (2.35)$$

Applying the boundary conditions  $v(0) = 0$  and  $v(d) = 0$ , we obtain

$$v_x(z) = \frac{g}{\eta} \left[ \frac{-(z - d_a)^2}{2} \Theta(d_a - z) - \frac{d_a^2}{2d} z + \frac{d_a^2}{2} \right] \quad (2.36)$$

Thus, the average velocity becomes

$$\bar{v} = \frac{1}{d} \int_0^d v(z) dz = \frac{gd_a^2(3 - 2d_a/d)}{12\eta} \quad (2.37)$$

The power consumption per area  $A$  is

$$\frac{P}{A} = \int \vec{f} \vec{v} dz = \frac{g^2 d_a^3}{12\eta} \left[ 4 - 3 \frac{d_a}{d} \right] \quad (2.38)$$

The limit  $d \rightarrow d_a$  is the Poiseuille flow. The limit  $d \rightarrow \infty$  is a semi-infinite system, where  $P/A$  can be calculated to be

$$\frac{P}{A} = \frac{16}{3} \frac{\bar{v}^2 \eta}{d_a}. \quad (2.39)$$

Figure 2.3 shows the velocity and force space dependence for  $d_a/d = \frac{1}{2}$ .

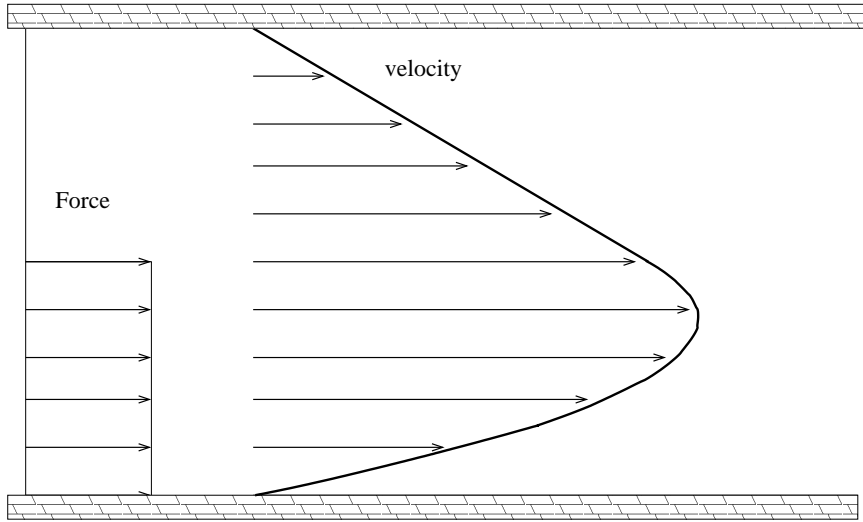


Figure 2.3: Schematic drawing of a partially driven flow with  $\frac{d_a}{d} = \frac{1}{2}$ . The arrows on the left-hand depict the force's space dependence; the resulting velocity profile is indicated on the right hand.

### 2.2.8 Dimensionless Efficiency

In both, the Poiseuille flow and the partially driven flow, the average velocity scales with  $g$ , and the power consumption per area is proportional to  $\bar{v}^2 \eta / d_a$ . We use the result from the partially driven flow for the limit  $d \rightarrow \infty$ , Eq. (2.39), to define a dimensionless efficiency

$$\epsilon = \frac{16}{3} \frac{\bar{v}^2 \eta A}{d_a P}. \quad (2.40)$$

When applied to cilia, we take  $d_a$  to be the cilia length.

This definition of efficiency has several advantages:

- It is dimensionless; therefore it is invariant under all transformations of length and time scales.
- It fulfills the expectations that the efficiency should increase with velocity and decrease with power consumption.
- It is independent of the area covered by cilia.

Thus the efficiency depends only on the type of flow. For example, the efficiency of the partially driven flow only depends on the ratio  $d_a/d$

$$\epsilon = \frac{\left(2 - \frac{4}{3} \frac{d_a}{d}\right)^2}{\left(4 - 3 \frac{d_a}{d}\right)}. \quad (2.41)$$

This leads to  $\epsilon = 1$  in the limit of  $d \rightarrow \infty$ , and  $\epsilon = 4/9$  in the limit of the Poiseuille flow.

When interpreting this efficiency for cilia systems, it is important to note that it leads to rather low efficiencies because  $\epsilon = 1$  is defined by a semi-infinite system, where the flow is generated by an artificial gravitational field parallel to the wall.

### 2.2.9 Rod Friction

As mentioned in Sec. 1.5.2, it is important for the sperm propulsion that the friction of a slender rod or filament is lower parallel to its orientation than perpendicular. Intuitively it is obvious that dragging a rod perpendicular rather than parallel to its orientation is more difficult, and the physical origin of this behavior is easy to understand. If moved parallel to its orientation, most of the rod can travel in the wake of the tip, thus reducing friction.

We define rod-drag coefficients for Stokes flow by

$$F_{\parallel} = \gamma_{\parallel} v_{\parallel} \quad (2.42)$$

$$F_{\perp} = \gamma_{\perp} v_{\perp} \quad (2.43)$$

with the subscript  $\parallel$  for vector components parallel to the rod, and  $\perp$  for perpendicular components. These friction coefficients are related to the diffusion

coefficients  $D_{\parallel,\perp}$  via

$$\gamma_{\parallel,\perp} = \frac{k_B T}{D_{\parallel,\perp}} \quad (2.44)$$

Calculating the diffusion coefficients for a rod-like colloid of finite length is not trivial, but approximations can be found in the literature. Tirado, Martinez and Garcia de la Torre [87] reviewed some theoretical approaches. The different theories agree on

$$\frac{2\pi\eta L_r D_{\parallel}}{k_B T} = \ln(L_r/d_r) + \nu_{\parallel} \quad (2.45)$$

$$\frac{4\pi\eta L_r D_{\perp}}{k_B T} = \ln(L_r/d_r) + \nu_{\perp}. \quad (2.46)$$

wherein  $L_r$  is the length, and  $d_r$  the diameter of the rod. Differences between theories are found concerning the correction functions  $\nu_{\perp/\parallel}$ . One approximation for  $2 < L_r/d_r < 30$  which has been used for simulations of rods in the nematic phase [59], is

$$\nu_{\perp} = 0.839 + 0.185d_r/L_r + 0.233 (d_r/L_r)^2 \quad (2.47)$$

$$\nu_{\parallel} = -0.207 + 0.980d_r/L_r - 0.133 (d_r/L_r)^2 \quad (2.48)$$

For understanding simulation results and construction of simulations without hydrodynamics, but with anisotropic friction, we performed simulations to calculate  $\gamma_{\perp}$  and  $\gamma_{\parallel}$ .

For this purpose we kept the structure in the center of a simulation box and exposed the structure to a constant flow. The friction coefficients were determined by averaging the momentum that is transferred onto the structure. A constant flow is achieved by assigning Gaussian-distributed velocities, with an average of  $\bar{v}$  in x direction, to particles in the front of the simulation box.

First, we checked whether the force was linear in  $\bar{v}$ . Figure 2.4 shows that the force is linear with  $\bar{v}$  at least up to  $\bar{v} \approx 0.3$ . We chose  $\bar{v} = 0.1$ , well within the linear regime for the remaining simulations.

Figure 2.5 shows as an example the parallel friction coefficient  $\gamma_{\parallel}$  as a function of scaled inverse linear system size ( $L_r/s_x$ ). To determine friction coefficients, we fitted a simple linear function to the data (see Fig. 2.5), and used the extrapolation to  $(L_r/s_x) = 0$ , which is equivalent to the infinite system. It is not obvious that the friction coefficients should be linear in system size, therefore, error bars are difficult to estimate, but in the order of 5% (better for  $\gamma_{\perp}$ ).

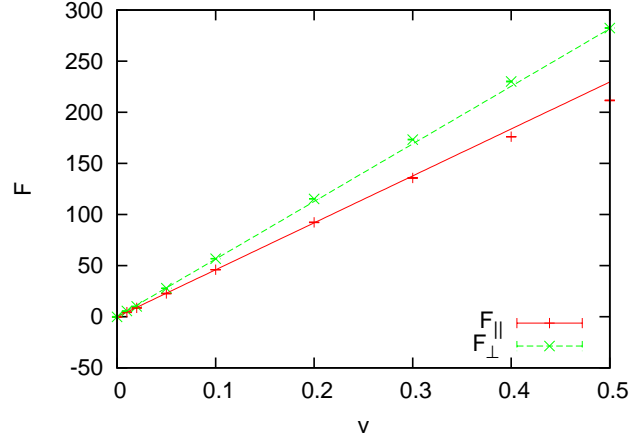


Figure 2.4: The force is linear in the velocity up to  $\bar{v} \approx 0.3$ . System size is  $(10a)^3$ ,  $h = 0.05$ , rod length is  $5a$  and measurements have been averaged over 100 000 MPCD steps.

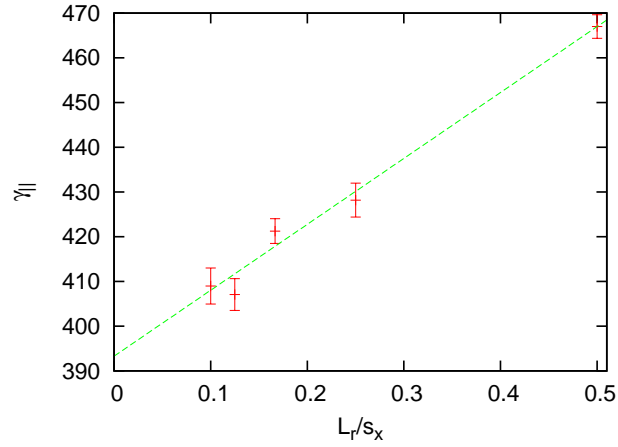


Figure 2.5:  $\gamma_{\parallel}$  as a function of inverse linear system size  $L_r/s_x$ . System size  $s_x$  varying between  $(10a)^3$  and  $(50a)^3$ .  $h = 0.05$ , rod length is  $5a$  and results have been averaged over 100 000 MPCD steps.

Considering the strong finite-size effects, and that the polymer rods are penetrable for the fluid, the agreement with theory is surprisingly good (see Fig. 2.6). The fit in Fig. 2.6 resulted in a rod diameter of  $d_r \approx 1.8$ , which is quite

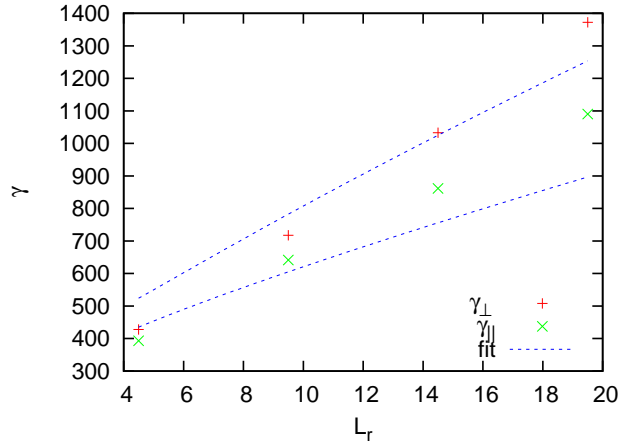


Figure 2.6:  $\gamma_{\parallel}$  and  $\gamma_{\perp}$  as a function of rod length  $L_r$ . The blue line is a fit of the theory (Eq.(2.45) and Eq.(2.46)).  $d_r \approx 1.8$  was obtained by fitting Eq.(2.46) to  $\gamma_{\perp}$ , this value was then used to plot Eq.(2.45). Points are results of finite size fits, see text.

reasonable, considering that the monomers have roughly a hydrodynamic diameter of  $1a$ . Furthermore, we see from Fig. 2.6 that at these low aspect ratios the approximation  $\gamma_{\perp}/\gamma_{\parallel} = 2$  does not hold.

## 2.3 Sperm Model

In this section, we describe how we simulate sperm motility. This model incorporates hydrodynamics by coupling it to an MPCD solvent as explained in Sec. 2.2.3. Furthermore, we explain how the model is simulated without hydrodynamics, and a further simplification, the so-called rocket model.

### 2.3.1 Sperm Structure

Using the method described above for polymers, we simulate the axoneme as a crane-like structure (see Fig 2.7). Three semi-flexible rods, each consisting of 100 monomers, are arranged in a triangular cross section. The distance between the rods and the distance between monomers within a rod is half a box length

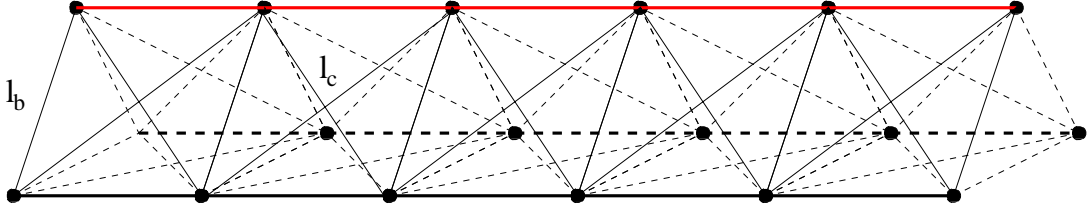


Figure 2.7: Model axoneme. The axoneme is modeled as three polymer rods, interconnected by harmonic springs. The bond lengths in one rod, marked red, are changed to introduce local bending moment.

(bond length  $l_b = 0.5a$ ). The rod length is kept nearly constant by a strong harmonic potential between neighboring monomers,

$$U = \frac{1}{2}K_1(|\vec{r}_{i,i+1}| - l_b)^2.$$

with  $K_1 = 200\,000 k_B T/a^2$ . The stiffness is taken into account by a bending potential,

$$U = -K_b \sum_i \Delta \vec{r}_i \cdot \Delta \vec{r}_{i+1}$$

where  $\Delta \vec{r}_i = \vec{r}_{i+1} - \vec{r}_i$  are the bond vectors. Furthermore, the rods are interconnected by harmonic springs

$$U = \frac{1}{2}K_2(|\vec{r}_{i,j}| - l_{b/c})^2.$$

with  $K_2 = 20\,000 k_B T/a^2$  between neighbors (bond length  $l_b = 0.5a$ ) and next-nearest neighbors (bond length  $l_c = \sqrt{2}l_b$ ) as indicated in Fig. 2.7.

In a real axoneme, active bending is generated by motor proteins (dynein), i.e. connecting proteins that move along a neighboring microtubule (see Sec. 1.2). This movement is translated into a change in the length of bonds on one side of the structure (the red rod in Fig. 2.7) thus imposing a local bending moment. In the simulation of sperm, the propulsion is achieved by imposing a sinusoidal propagating bending wave along the axoneme,

$$l(t, x) = l_b + A \sin(kx - \omega t)$$

where

$l_b$  = relaxed bond length

$A$  = amplitude of length change, i.e. beat strength

$k$  = wave number

$x$  = distance along the axoneme

$\omega$  = beat frequency

$t$  = time

This treatment is equivalent to a sinusoidal beat pattern, as used in other models [27]. The activity parameters are chosen such that a natural beating pattern was roughly reproduced. MPCD resolves hydrodynamics roughly on the length scale or the box size  $a$ . This is why  $l_b = 0.5a$  provides a sufficiently dense distribution of monomers along the rod.

In order for our model to be reasonably realistic, we used the parameters of sea urchin sperm as a guide. The sperm is roughly  $50 \mu m$  long and has a beating amplitude of roughly  $4 \mu m$ . Typically about 1.5 waves are present on the axoneme at a given time. Therefore we chose  $A = 0.1l_b$  and  $k = 0.15/l_b$  such the beating amplitude is about  $2.5a$  and 1.5 waves are present on the tail.

The time scale of the simulation is set by  $\omega = 0.1\sqrt{k_B T/m a^2}$  (the higher  $\omega$ , the faster the sperm will move); at the same time  $\omega$  sets the rate of energy input at the sperm tail. Therefore,  $\omega$  has to be a compromise between computational efficiency and constant temperature throughout the system.

The head of the sperm is modeled by a sphere, constructed of 163 monomers, which is attached to the front of the axoneme structure. The sphere has a radius of  $r_h = 2a$  and is held together by harmonic springs (with  $K_{h1} = 10\,000 k_B T/a^2$  between center and head monomers, and  $K_{h2} = 100\,000 k_B T/a^2$  between neighboring monomers). Furthermore, we bend the front part (first 15 bonds) of the axoneme along a different rod than the beating rod to introduce chirality. The simulation input parameter is the length  $\Delta l$  by which the bonds are shortened, but for simplicity we convert it to the angle formed by the bend between the tangent to the structure at the head and after the bend. This is called the bending parameter  $b$ . In Fig. 2.8, different bending parameters are illustrated.

A short calculation leads to a simple linear dependence of the bending param-

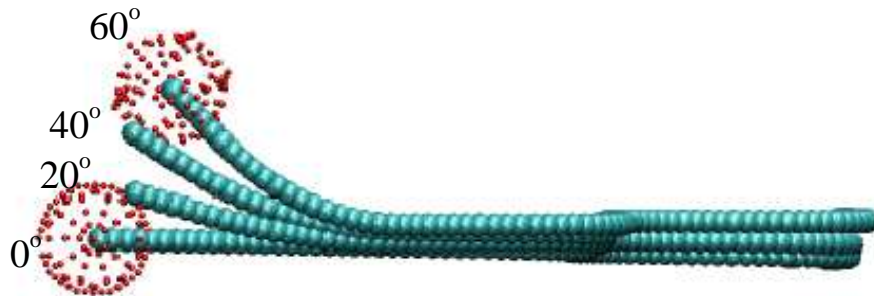


Figure 2.8: Sperm with bending parameters  $b = 0^\circ$ ,  $20^\circ$ ,  $40^\circ$ , and  $60^\circ$ . For clarity, only one rod is displayed, plus the sperm head for  $b = 0^\circ$  and  $b = 60^\circ$ . Visualization using VMD [38].

eter on the length change,

$$b = \frac{2l}{\sin(\pi/3)l_b} \Delta l \quad (2.49)$$

which implies  $b = 34.6\Delta l$ .

Finally, the “relaxed” ( $\omega = 0$ ) structure looks like a sperm. Figure 2.9 shows a snapshot of the relaxed sperm.

To summarize, we model the sperm by a crane-like structure that enables us to impose active bending. In front is a spherical head of  $2a$  radius, thus covering the first 5 monomers of the rod structure, one more bond is left undisturbed for straight attachment. Along the following 15 bonds, we bent the structure for chirality, while a sinusoidal bending wave propagates along the rest of the tail. The bending parameter will turn out to be of great importance, strongly affecting the sperm behavior.

### 2.3.2 Importance of Asymmetry

Obviously, the helical motion is caused by the chirality of the sperm. It is important to note that not just any asymmetrical beating is sufficient to cause a helical trajectory, i.e. the sperm has to have a handedness. A sperm only asymmetric inside the beating plane would swim in a circle within the beating plane, whereas sperm only asymmetric in  $z$ -direction would follow a circle perpendicular to the beating plane. The combination of both causes the helical motion. This asymmetry does not necessary require to be an asymmetric attachment of

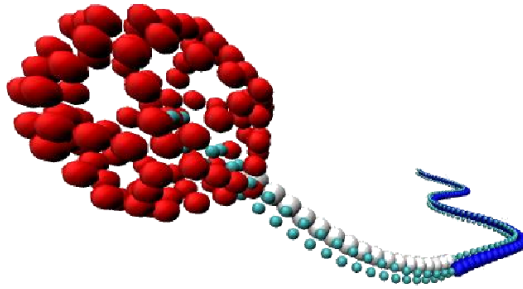


Figure 2.9: Complete sperm model. In this picture, the monomers are represented by small spheres. The dark blue monomers represent the rod where bond lengths are periodically changed to impose a propagating bending wave along the axoneme. In a different rod, the first 15 bonds (gray) are shortened to introduce chirality. In parts of rods where the bond length is not altered, the monomers are colored cyan. Visualization using VMD [38].

the head. Asymmetry within the beating pattern (including an out of the plane beat) for example could lead to a similar behavior.

The orientated circular motion at the walls also requires chirality. Achiral sperm will still be captured by the surface, but the handedness of the circular path (in our case clockwise when viewed from inside the observation chamber, but this can be reversed by changing the direction of the chirality) is only possible with chiral sperm.

### 2.3.3 Sperm Simulations without Hydrodynamics

In order to identify the role of hydrodynamic interactions, we also performed simulations without MPCD. For the propulsion of sperm, the friction coefficient of a rod has to be anisotropic, i.e. a rod slides more easily along its orientation than perpendicular to it, i.e.  $\gamma_{\parallel} < \gamma_{\perp}$  (see Secs. 1.5.2 and 2.2.9 for details). As explained in Sec. 2.2.9, this is a hydrodynamic effect. However, in the way presented below, we can separate the anisotropic friction from other, more complicated, hydrodynamic effects.

Therefore, we model the sperm as before, but, instead of the MPCD fluid, we add a friction force proportional to the particle velocity obtained from Eq.

(2.42),

$$\vec{F} = -\gamma\vec{v}_\perp + \frac{\gamma_\parallel}{\gamma_\perp}\gamma\vec{v}_\parallel, \quad (2.50)$$

wherein the parallel direction is defined by the difference vector between the adjacent monomers in the rod. In order to distinguish between magnitude of friction ( $\gamma$ ) and friction anisotropy ( $\gamma_\parallel/\gamma_\perp$ ), we separated the two parameters in Eq. (2.50). We have seen in Sec. 2.2.9 that the ratio  $\gamma_\parallel/\gamma_\perp$  strongly depends on the length of the structure. This implementation allows us to use ratios derived from the MPCD simulation, or the theoretical value for long slender filaments

$$\lim_{l/d \rightarrow \infty} \gamma_\perp/\gamma_\parallel = 2. \quad (2.51)$$

In Sec. 2.2.9 we have determined the total friction coefficients of a rod,  $\gamma_\parallel$  and  $\gamma_\perp$ . For these simulations,  $\gamma$  is the effective friction coefficient of a monomer. Because  $\gamma_\parallel$  and  $\gamma_\perp$  roughly scale with the rod length  $L$ , and thus with the number of monomers  $N$ , we simply divide  $\gamma_\perp$  by  $N$  and obtain  $\gamma \approx 10$  as an order of magnitude value for the friction coefficient.

The friction on the head monomers can be estimated by dividing the friction coefficient of a sphere  $6\pi\eta r_h$ , divided by the number of monomers. Because this approximation leads to the same order of magnitude, we use

$$\vec{F} = -\gamma\vec{v}. \quad (2.52)$$

A difference in the quantitative behavior to simulations with hydrodynamics is expected because MPCD takes into account the curvature of the tail, thermal fluctuations and hydrodynamic interaction with the wall. Furthermore, the model without hydrodynamics assumes, due to its way of implementation, a different ratio between the drag of the head and the tail compared to the MPCD version.

Nevertheless, changes in the qualitative behavior should mainly be due to hydrodynamic interactions. The model presented here does not include thermal fluctuations, which also influence the trajectory. This provides the opportunity to get sperm trajectories without fluctuations, making the trajectory analysis easier. Additionally, the time saved by not computing MPCD steps allows us to simulate a larger range of parameters.

### 2.3.4 Rocket Model

In order to better understand the various effects contributing to sperm hydrodynamics we simplify the sperm even further by reducing it to a self-propelling rod. No head is added to the crane like structure and it is propelled by adding a predefined momentum increment, directed towards one end of the rod to each monomer.

As this model is much simpler, it is also more general and it may also capture dynamics of other self-propelling organisms or particles, which are of independent current interest. Artificial microscopic swimmers [18] have been realized experimentally by attaching magnetic colloids to a red blood cell. Theoretical studies include the formation of collective patterns [17] and kinetic phase transition [14] or descriptions of possible realizations [25].

We simulated this rocket both with and without hydrodynamics. In the first case momentum is conserved by subtracting the same momentum increment added to the rod from the surrounding fluid particles. Because the rocket model with hydrodynamics did not result in qualitative different behavior, only few simulations were performed. In the simulations without hydrodynamics, we used the scheme to turn off hydrodynamics described in Sec. 2.2.3.

## 2.4 Cilium

### 2.4.1 Cilia Structure

To model cilia we use the same axoneme structure as for the sperm (see Sec. 2.3), just shortened to a length of 20 monomers ( $10a$ ). Figure 2.10 illustrates the cilia model. The crane-like axoneme model represents a single cilium. Instead of attaching a head, the cilia are grafted to a no-slip wall at  $z = 0$  by fixing the position of the lower two monomers of each rod. A second wall at  $z = 20a$  confines the simulation in  $z$  direction. In studies of multi-cilia arrays they are arranged on a square lattice, with the lattice vectors pointing in  $x$  and  $y$  direction.

The beat pattern of cilia is very different to that of sperm. We are interested in studying metachrony, thus a feedback of the hydrodynamic flow to the beat pattern is essential. As in the sperm simulations, we do not intend to model the axoneme dynamics. The beat pattern, which is more complicated than in the

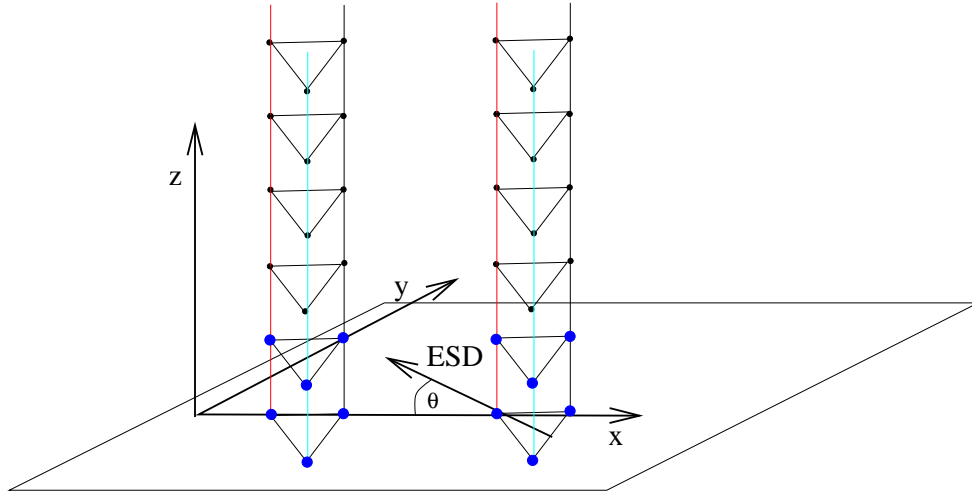


Figure 2.10: Cilia model structure. The crane-like axoneme model represents a single cilium. Lengths of red bonds are changed for activity, thus determining the effective stroke direction (ESD, angle  $\Theta$ ). Position of the lowest monomers (blue and thicker) is fixed. The first seven bonds of the cyan rod are shortened during an aplanar recovery stroke.

sperm simulation, is an input parameter; it is designed such as to closely mimic the beat pattern observed experimentally.

As in the sperm model, the beat pattern is implemented by a local length change of the bonds of one rod (see Fig. 2.10). We use the experimental results and theoretical findings mentioned in Sec. 1.4 and 1.5 to develop a realistic beat shape. The beat pattern is divided in two strokes, the *effective stroke*, and the *recovery stroke*, as explained in the following.

The different strokes are controlled by the bending point  $i_0$ . In the *effective stroke* the bending point is at  $2a$  from the bottom (5th monomer,  $i_0 = 5$ ), and the bond length is

$$\frac{l(i)}{a} = \frac{l_b}{a} - \frac{3}{5(i - i_0)^2} \quad (2.53)$$

where  $i$  is the monomer number, and  $l_b/a = 0.5$  is the bond length for the non-active rod. This also shows why  $i_0$  is called the bending point, the spontaneous curvature is maximal at  $i_0$ , rapidly decreasing away from  $i_0$ . The idea for arises from pictures of the beat pattern of cilia, where in the effective stroke a strong bent is seen at the bottom, and a relatively straight cilium otherwise.

In the *recovery stroke* the bending point moves upwards along the cilium with a constant speed of one monomer per 10 MPCD time units. Additionally, we drive the cilium in the opposite direction as in the effective stroke. The active rod is stretched according to

$$l(i) = l_b + a_1 l_b \left( \frac{n_r - 1 - i}{n_r} \right)^{a_2} \quad (2.54)$$

for  $i < i_0 - 1$ , where  $n_r$  is the number of monomers in on rod,  $a_1 = 0.3$  and  $a_2 = 2.5$  are parameters chosen such as to resemble a realistic beat. Combined we obtain

$$\frac{l(i)}{a} = \begin{cases} \frac{l_b}{a} + a_1 \frac{l_b}{a} \left( \frac{n_r - 1 - i}{n_r} \right)^{a_2} & \text{if } (i < i_0 - 1) \\ \frac{l_b}{a} - \frac{3}{5(i - i_0)^2} & \text{if } (i \geq i_0 - 1) \end{cases}. \quad (2.55)$$

Again this scheme is motivated by observations from real beat patterns. The bent seen in the effective stroke moves upwards along the axoneme, and bent in the opposite direction is located at the bottom.

*Switching* between different strokes is controlled by the curvature of the cilium. The curvature of the cilium is measured by the contour-length difference between the active rod and the passive rods,

$$\Delta l = 2l_{r1} - l_{r2} - l_{r3} \quad (2.56)$$

where  $l_{r1}$  is the contour length of the active rod (i.e. the rod where the bond lengths are changed) and  $l_{r2,3}$  the contour lengths of the two passive rods. If during the effective stroke  $\Delta l < \Delta l_{min}$  the cilium is switched to recover stroke, and the midpoint is moved to  $i_0 = 7$ . Whereas in the recovery stroke  $\Delta l > \Delta l_{max}$  switches the cilium back to the effective stroke. We chose  $\Delta l_{min} = -1$  and  $\Delta l_{max} = 0.6$ . This bending-dependent switching is motivated by the theoretical works presented in Sec. 1.5

Large stress can lead to a kink-like defect in the model cilium with strong local curvature. Real motor proteins have a *stall force*, a force at which the motor protein does not move foreword anymore. Implementing the analogue of such a stall force into our model also solves the problem of kink defects. Because length changes represent in our model the motor protein activity, the stall force is represented by a maximum length change  $\Delta l_{max} = 0.015$ . If the newly calculated length differs more than  $\Delta l_{max}$  from the actual length  $l_a$ ,  $l(i)$  is set to  $l_a \pm \Delta l_{max}$ .

Because in the case of  $\Delta l > \Delta l_{max}$  we do not want the rods to slide backwards, we have to compare  $l(i)$  from the last iteration ( $l_{old}$ ) with the new one before ( $l_{new}$ ) and after ( $l_{stall}$ ) the application of the stall mechanism:

- If  $l_{new} = l_{old}$  the motor was not activated, thus  $l(i) = l_{old}$ .
- If  $l_{new} > l_{old}$  but  $l_{stall} < l_{old}$  (or vice versa) the motor proteins stall and the bond length stays at its previous value. Thus also in this case  $l(i) = l_{old}$ .

Fig. 2.11 shows the beat of a single cilium which results from this model. It closely resembles the schematic experimental drawing (see Fig.1.9).

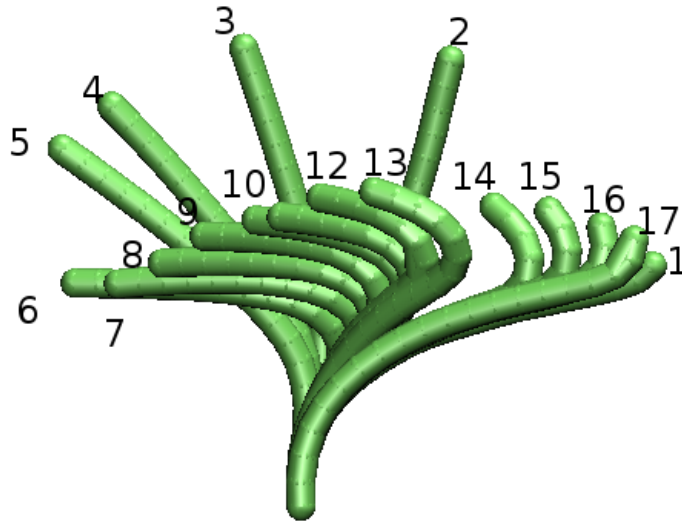


Figure 2.11: Beat cycle of isolated cilia. Each frame is 10 time units apart. System size is  $20^3$  boxes, otherwise as in the reference system. Visualization using VMD [38].

We also studied aplanar beating of the cilium. In this case we have shortened the first seven bonds of a second rod during the recovery stroke by the aplanarity parameter  $a_{apl}$ , similar to the asymmetry parameter in sperm (see Fig. 2.10).

### 2.4.2 Control Parameters for Cilia

The cilia simulations have many different input parameters. Here we will focus on the following:

- *System size* is crucial in cilia simulations. Typically we simulate square arrays of cilia with periodic boundary conditions in the  $x$  and  $y$  directions. Because we also study long-range synchronization, finite-size effects are expected. Also, because the cilia are arranged on a lattice, there are lattice effects restricting the  $\vec{k}$  vector. If not noted otherwise, system size is  $20 \times 20$  cilia, as in the reference system defined below.
- $\Theta$  is the angle between the effective stroke and the negative  $x$  direction. In the reference system  $\Theta = 45^\circ$  (see Fig. 2.10).
- The *fluid viscosity*  $\eta$  changes the cilia behavior. For an experimental study see Ref. [22]. The viscosity in MPCD can be changed by changing the collision angle, or the time step. (See Poiseuille Flow, Sec. 2.2.6). In the reference system, and most other simulations, we use the time step  $h = 0.05$ , corresponding to  $\eta = 16.5 \frac{\sqrt{k_B T m}}{a^2}$ . Within this work we change the viscosity solely by changing the time step  $h$ .
- The *aplanarity parameter*  $a_{apl}$  measures how much the recovery stroke is out of the beating plane of the effective stroke. Like the bending parameter for sperm, it measures by how much the first seven bonds are shortened.  $a_{apl} = 0.05$  in the reference system.
- *Cilia spacing*  $d_c$  is the distance between neighboring cilia on the lattice.

A *reference system* is defined from which we deduce other simulations. Simulations presented here will have the same parameters as the reference system except when mentioned otherwise. The reference system is a simulation of  $20 \times 20$  cilia,  $5a$  apart. The system size in  $x$  and  $y$  direction is adapted to the number of cilia and their spacing. The distance to the top wall is  $20a$ , thus the reference system-size is  $100^2 \times 20$  boxes. With 10 fluid particles per box ( $\rho = 10$ ) and a time step of  $h = 0.05$ ,  $\eta = 16.5$ . The viscosity is changed by scaling the time step  $h$  in MPCD appropriately. The aplanarity parameter is  $a_{apl} = 0.05$  and the effective stroke direction  $\Theta = 45^\circ$ .

## 2.5 Boundary Conditions

For the *sperm simulations* all particles (fluid and monomers) experience periodic boundary conditions in  $x$  and  $y$  direction. In the case of a sperm in bulk solution,

we employ periodic boundary conditions also in  $z$ -direction. The confined case is defined by solid walls at  $z = 0 a$  and  $z = 50 a$ . Here we apply no slip boundary conditions at the walls. Furthermore the monomers experience a purely repulsive shifted and truncated Lennard-Jones potential (range  $\sigma = 0.223 a$ , cutoff  $0.25 a$ ) with the walls. Simulations with different boundary conditions have been performed, but do not lead to qualitative different behavior. The size of the simulation box is  $75 \times 75 \times 50$  boxes ( $70 \times 70 \times 70$  boxes in the free case), each containing 10 solvent particles on average. So we have a total of 2.8 million (3.4 million) particles.

For the *cilia simulations* we always use periodic boundary conditions in  $x$  and  $y$  direction and hard, no-slip, walls at  $z = 0 a$  and  $z = 20 a$ . The lateral system size is adapted to fit the cilia with a given spacing.



# 3 Sperm Results

In this chapter we present the results for the simulation of the hydrodynamic behavior of sperm. We begin with defining important quantities, then we turn our attention to the sperm motion in bulk fluid. Finally, we present the results for the motility of sperm in confinement.

## 3.1 Important Observables

Several quantities are important to understand the results:

- The *bending parameter*  $b$  introduced in Sec. 2.3.1 represents the key control parameter. It defines how much the head is bent compared to a straight sperm (see Fig 2.8).
- The *director*  $\vec{d}$  is defined as the vector from the end of the tail to the center of the sperm's head.
- The *director angle*  $\alpha_d$  is defined as the angle between the director and the wall. A director angle  $\alpha_d = 0$  indicates parallel alignment. With a positive  $\alpha_d$  the director points towards the surface, with a negative  $\alpha_d$  away from the surface.
- The *beating plane* is the plane in which the tail performs its sinusoidal motion. In Fig. 2.9, the beating plane is almost horizontal. Its normal vector  $\vec{n}$  is determined by averaging the difference vectors of equivalent monomers of the two non-active rods. In Fig. 2.9. the normal vector  $\vec{n}$  is pointing upwards.
- The *wall angle*  $\alpha_w$  is the angle between the wall normal  $\vec{e}_z$  and the normal of the beating plane  $\vec{n}$  seen from behind the sperm, I.e. it is the angle between  $\vec{e}_z$  and the projection of  $\vec{n}$  onto the plane spanned by  $\vec{e}_z$  and  $\vec{e}_z \times \vec{d}$  and  $\vec{e}_z$ . This complicated construction has the advantage that the

result is independent of the constant tilt of the sperm towards the wall. This allows us to determine the orientation of the beating plane towards the wall, independent from the director angle  $\alpha_d$ .

## 3.2 Free Movement

In a bulk fluid, most sperm swim along helical trajectories [26], the handedness depending on the species. In the following section, we will study the origin of this helical movement.

### 3.2.1 Simulations with Hydrodynamics

In bulk fluid, we observe that sperm follow a right-handed helical trajectory (see Fig. 3.1). This helical motion strongly depends on the bending parameter. Figure 3.1 shows a typical simulation snapshot of a model sperm with a bending parameter of  $60^\circ$ . The trajectory of the sperm's head clearly is helical.

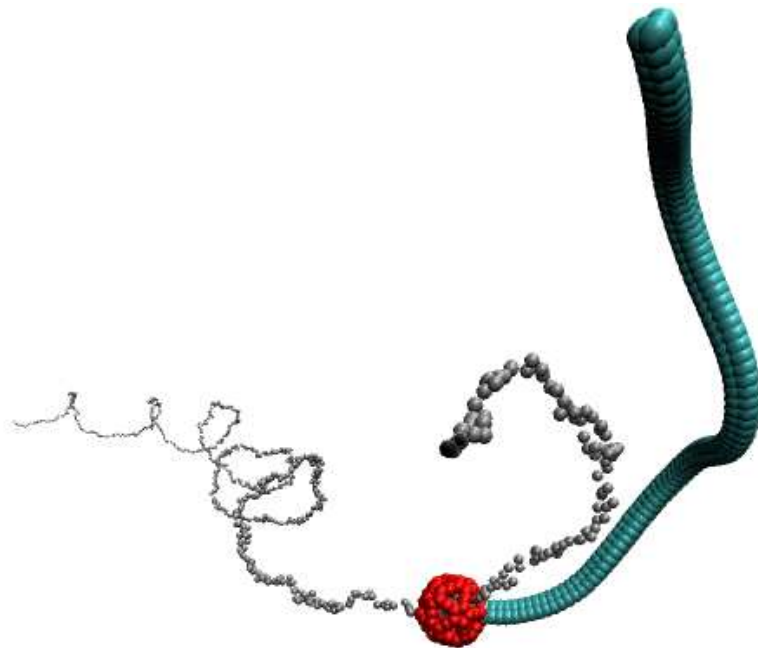


Figure 3.1: Without walls the sperm swims in a helical motion. The sperm (in cyan and red) has a bending parameter of  $60^\circ$ , the gray helix is the trajectory of the sperms head. Visualization using VMD [38].

We observe two different kinds of trajectories. Weakly bent sperm swim on a narrow helix. The tail is always close to the trajectory, just the head performs some sideways motions. Strongly bent sperm swim in a larger helix with the head near the center of the helix and the tail pointing outward (see Fig. 3.1).

To distinguish these two regimes, we fit a helix to the trajectory of the sperm's head, thus gaining access to all helix parameters. The trajectory is rather noisy on all length scales, making a fit difficult and error prone. When the helix radius is small, the fit is especially difficult, sometimes mistaking the wiggling of the head for the helical movement. Thus, some parameters, especially the pitch and curvature, can be only determined for stronger bent sperm, . The curvature can be determined in other ways as well, but for weakly bent sperm, it is still difficult because, due to the helix shape and thermal fluctuations, the curvature depends strongly on the length scale used.

As by eye judgment, we find a “weakly bent regime” ( $b < 40^\circ$ ) where the trajectory is almost straight, just the head circles around a roughly straight line, making the fit difficult and inaccurate. In the “strongly bent regime” ( $b > 40^\circ$ ), we obtain a helix whose radius increases with the bending parameter  $b$ . In Fig. 3.2, we plot the radius of the trajectory  $R_h$  as obtained by a helix fit. The finite values for small bending parameters ( $R_h(0) \approx 1 a$ ) are, as mentioned above, due to the oscillating movements of the head.

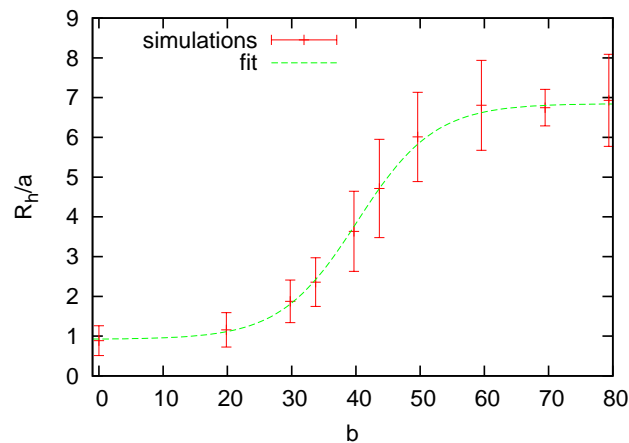


Figure 3.2: Helix radius  $R_h$  as a function of bending parameter  $b$  as obtained by a helix fit. The dashed line is a fit to a translated and stretched hyperbolic tangent.

The curvature obtained from the helix fit is, due to fluctuations, prone to

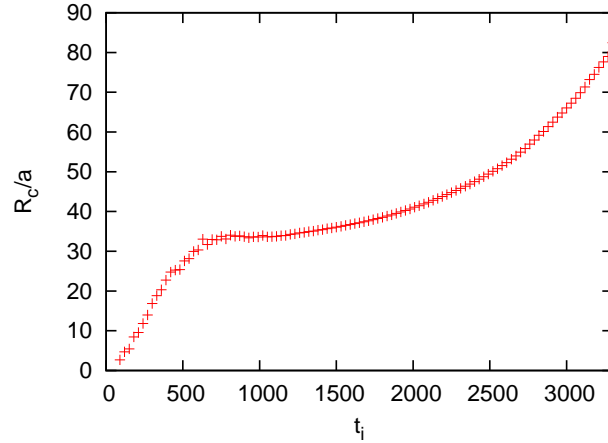


Figure 3.3: The radius of curvature  $R_c$  as a function of time interval  $t_i$  for a free-swimming sperm with bending parameter  $b = 50^\circ$ .

systematic errors. For weakly bent sperm, the helix fit results in narrow helix, although it is just the wiggling head. The curvature of the trajectory, seen on a larger length scale, has to be determined independently. For this purpose, we used a three-point analysis. We choose a time interval  $t_i$  and then averaged the circles defined by the three points  $\vec{r}(t - t_i)$ ,  $\vec{r}(t)$ ,  $\vec{r}(t + t_i)$ . Performing this average for several time intervals  $t_i$ , provides a radius of curvature as a function of the time scale. Fig. 3.3 shows a typical plot of the radius of curvature,  $R_c$ , as a function of the time interval. On a short time scale, the radius of curvature is determined by the fluctuations. The larger values of the radius of curvature for long time scales are due to the helical shape of the trajectory. The intermediate time scales can be used for estimates of the radius of curvature. In the regime of bending parameters, where the curvature can also be determined from a helix fit, the two estimates roughly agree. Errors are of the order of 10%.

These curvature estimates have been used in Fig. 3.4. The curvature also shows the difference between weakly and strongly bent sperm. It increases monotonically with the bending parameter  $b$ , with a stepwise increase at  $b \approx 45^\circ$ .

The pitch  $l_p$  of the helix can only be defined for  $b > 40^\circ$ . It is roughly constant and about an order of magnitude larger than the helix radius (see Fig. 3.5). This means that even at the highest bending parameter studied, the helix is rather stretched. This fits well with velocity measurements (see Fig. 3.6): The velocity along the center of the helix is not much smaller than the velocity along the trajectory.

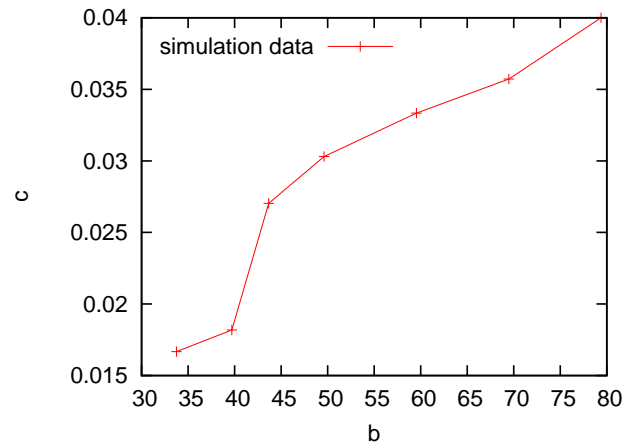


Figure 3.4: The curvature  $c = 1/R_c$  of the trajectory versus bending parameter  $b$  (degrees)

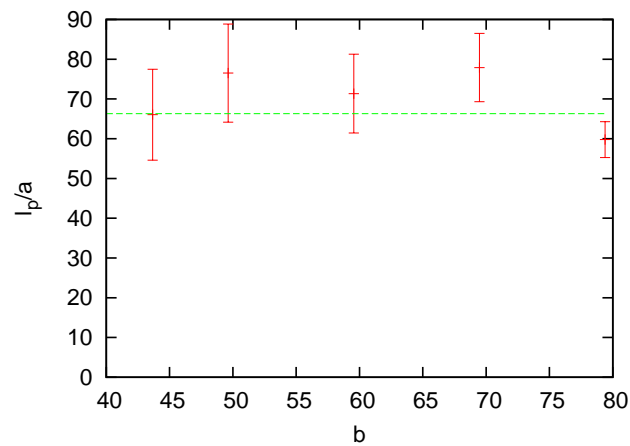


Figure 3.5: The pitch  $l_p$  of the trajectory versus bending parameter  $b$  (degrees). The pitch can only be defined for  $b > 40^\circ$ .

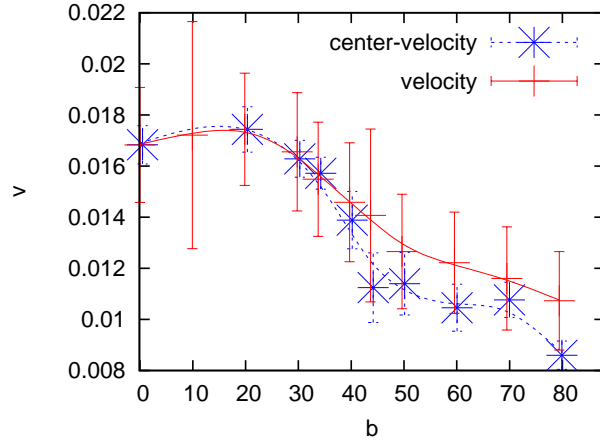


Figure 3.6: Velocity along the center of the helix (blue) and along the trajectory (red)

The two regimes of motion can be distinguished by the director auto-correlation function.

$$G_s(t) = \frac{\langle \vec{d}(t_0) \cdot \vec{d}(t_0 + t) \rangle_{t_0}}{\langle \vec{d}(t_0)^2 \rangle_{t_0}} \quad (3.1)$$

Typically, the sperm director points along the tangent of the trajectory as expected. In a perfect circular motion, the director autocorrelation function is  $G_s(t) = \cos(\omega t)$ . As the circular motion gets stretched to a helix, the amplitude reduces and a constant term is added. Therefore, the amplitude of the autocorrelation function oscillations provides a good measure how helical the movement is.

As an example, consider a perfect helix. Under the assumption that the director is parallel to the tangent of the curve, the director auto-correlation function can be calculated analytically. Suppose, without loss of generality, that the helix has the form

$$\vec{r}(t) = \begin{pmatrix} R_h \cos(\omega t) \\ R_h \sin(\omega t) \\ vt \end{pmatrix} \quad (3.2)$$

Then  $G_s(t)$  is easily calculated to be

$$G_s(t) = \frac{\omega^2 R_h^2 \cos(\omega t) + v^2}{\omega^2 R_h^2 + v^2} = \frac{\cos(\omega t) + 4\pi^2 c^2}{1 + 4\pi^2 c^2} \quad (3.3)$$

wherein  $c = \frac{v}{2\pi\omega R_h} = \frac{l_P}{R_h}$ , which is the ratio between pitch  $l_P$  and the helix radius  $R_h$ . Of course these relations require that  $\vec{d}$  is parallel to the tangent vector of a helical trajectory.

Furthermore, thermal fluctuations influence the director auto-correlation function. Eventually fluctuations will change the path as well, decreasing the auto-correlation function by a factor  $\exp(-t/\tau)$ , where  $\tau$  is a decay time. Combining these contributions, we expect a director auto-correlation function of the form

$$G_s(t) = e^{-t/\tau}(A_G \cos(\omega t) + c_1) \quad (3.4)$$

The amplitude  $A_G$  of the oscillations of the director auto-correlation function provides a good measure to distinguish the regimes of motion. For the helix parametrization presented above in eq.(3.2),  $A_G = (1 + 4\pi^2 c^2)^{-1}$ .

Figure 3.7 shows a plot of the director auto-correlation function for two different bending parameters. A small change from  $b = 33^\circ$  to  $b = 40^\circ$  causes oscillations of  $G_s$ .

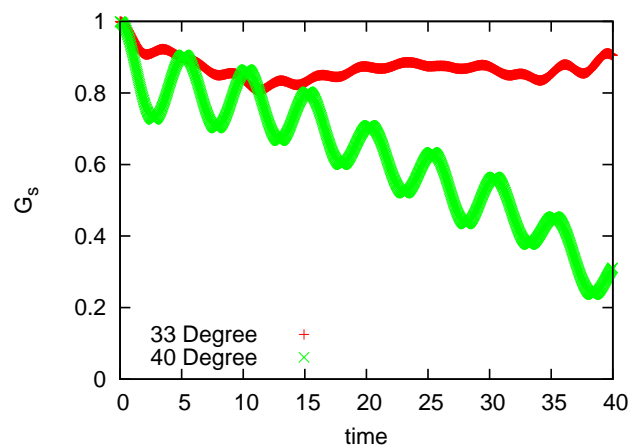


Figure 3.7: Strongly bent sperm show oscillations of the auto-correlation function  $G_s$ , whereas weakly bent sperm do not.

To show the transition between narrow and wide helices, we fit Eq. (3.4) to the simulation data via the decay time  $\tau$ , the amplitude  $A_G$ , and some constant  $c_1$ . A plot of the amplitude  $A_G$  versus bending parameter shows the transition very clearly (see Fig. 3.8).

The reason for this transition seems to be that when the bending of the sperm is large enough, the force on the head is sufficient to bent it even more, thus causing a rapid change in curvature. A more detailed discussion is given in Sec. 3.2.3 below.

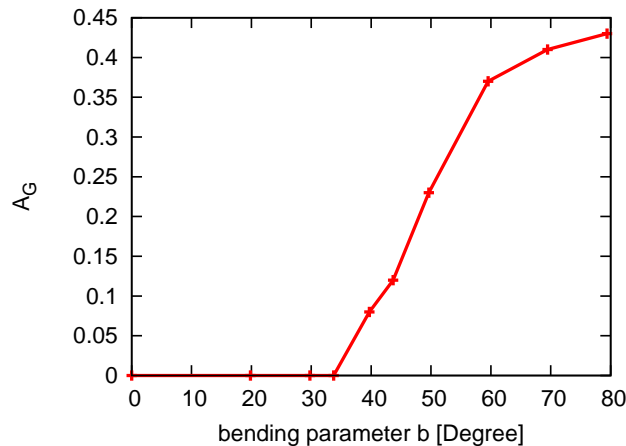


Figure 3.8: The amplitude  $A_g$  of the director auto-correlation function oscillations show clearly the difference of the low-bent and high-bent regime.

### 3.2.2 Simulations without Hydrodynamics

As mentioned in Sec. 2.3.3, simulations of sperm without hydrodynamics allows to distinguish between “hydrodynamic interactions” and “friction effects”.

Without hydrodynamic interactions, the bulk motion shows an even more extreme increase in its trajectory parameters as function of the bending parameter (see Figs. 3.11 and 3.12). Again the amplitude of the director auto-correlation function oscillations  $A_G$  (Figs. 3.9 and 3.10) is suitable to distinguish whether the sperm points generally in the direction of movement, or whether it follows a large helix, with the tail pointing outward. Due to the lack of thermal fluctuations trajectory parameters can be determined more precisely, especially it is possible to determine the radius of the helix also in the weakly bent regime. Due to the lack of fluctuations, the transition point can be determined with higher accuracy. Qualitatively, we always observed a stepwise increase in the helix radius, the radius being largest close to the transition point.

Interestingly, the helix shape also depends on the friction coefficient (see especially Fig. 3.13). In laminar flow, one expects that the viscosity only influences the time scale, not the shape of the motion, if the forces are the same. However, two important points have to be considered:

- The forces are predefined, but changing in time. Thus a different velocity results in the same force acting at a different point in the trajectory, i.e.

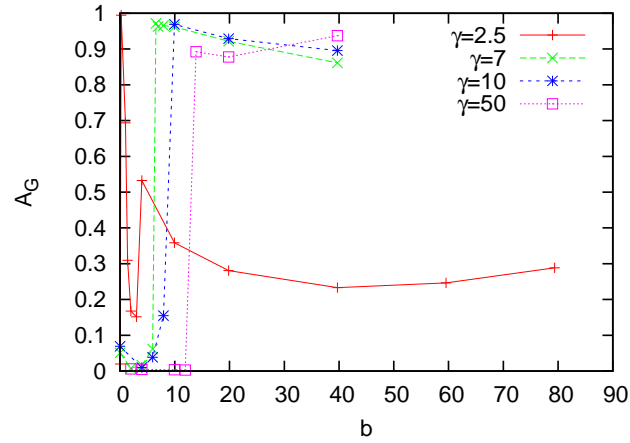


Figure 3.9: The amplitudes of the director auto-correlation function oscillations for sperm simulations without hydrodynamics with  $\gamma_{\perp}/\gamma_{\parallel} = 2$ , for various friction coefficients as indicated.

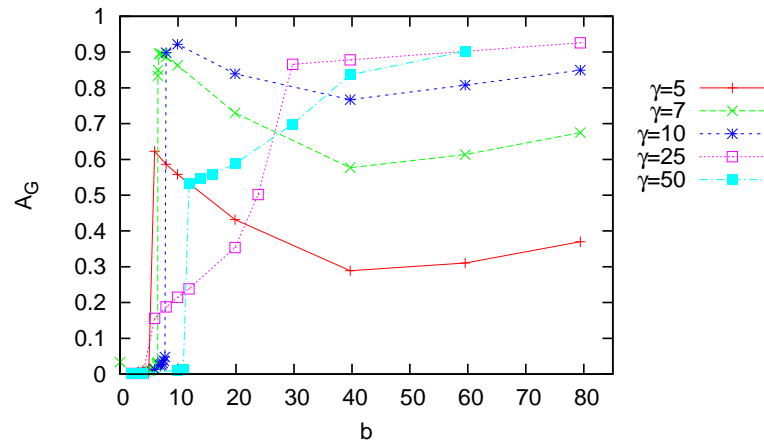


Figure 3.10: The amplitudes of the director auto-correlation function oscillations for sperm simulations without hydrodynamics with  $\gamma_{\perp}/\gamma_{\parallel} = 1.33$ , for various friction coefficients as indicated.

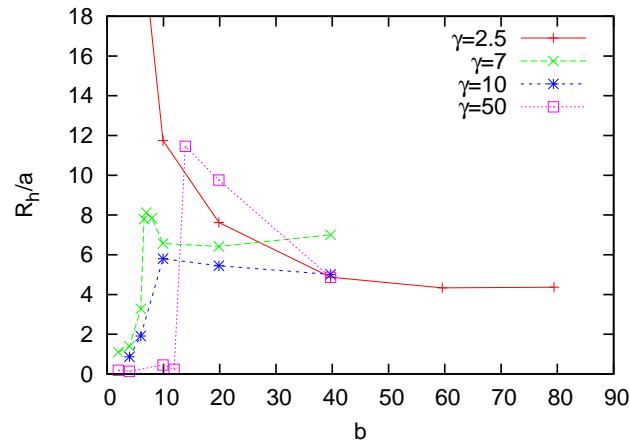


Figure 3.11: Radius of the helical trajectory vs bending parameter for sperm simulations without hydrodynamics with  $\gamma_{\perp}/\gamma_{\parallel} = 2$ , for various friction coefficients as indicated.

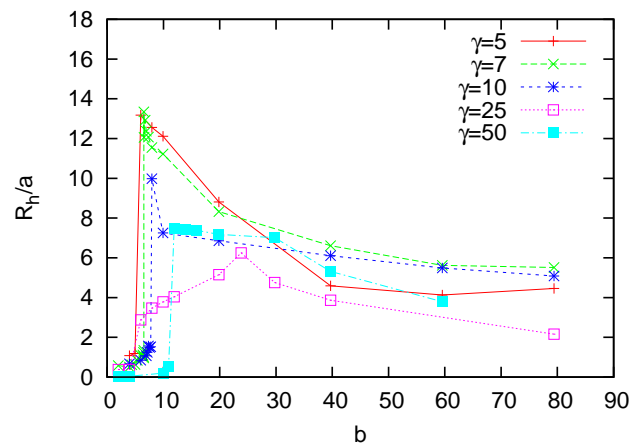


Figure 3.12: Radius of the helical trajectory vs bending parameter for sperm simulations without hydrodynamics with  $\gamma_{\perp}/\gamma_{\parallel} = 1.33$ , for various friction coefficients as indicated.

two time scales are present, one defined by the friction coefficient  $\gamma$ , the other by the beat frequency  $\omega$ .

- The model undergoes a change in shape under the force balance between elastic forces in the sperm and the viscous drag on the head.

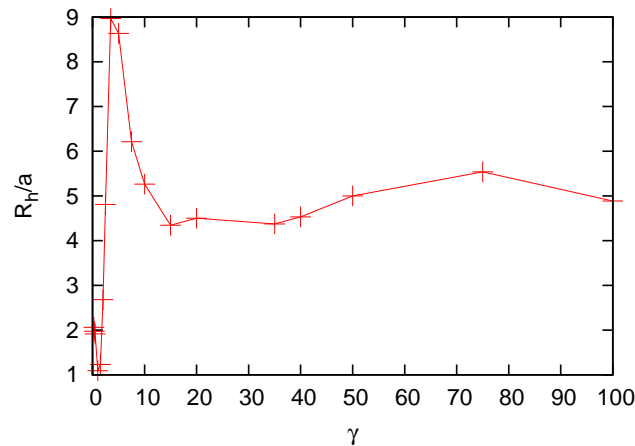


Figure 3.13: Radius of the helical trajectory  $R_h$  as a function of friction coefficient  $\gamma$  for sperm simulations without hydrodynamics with  $\gamma_{\perp}/\gamma_{\parallel} = 2$ . Bending parameter is  $b = 40^\circ$

Finally, it is possible to determine the curvature of sperm trajectories in simulations without hydrodynamics even for small bending parameters. The stepwise increase of the curvature at the transition can be clearly seen (see Figs. 3.14 and 3.15).

We emphasize that the data for sperm using high friction coefficients ( $\gamma > 20$ ) has to be interpreted with caution. For high friction coefficients, the sperm experiences sufficient mechanical stress that may influence its beat pattern. At  $\gamma = 100$ , the shape of the tail is not sinusoidal anymore; therefore this data is not presented here.

The simulations support the hypothesis that a shape change of sperm, caused by the drag of the head, causes the transition. Clearly, no hydrodynamic interactions, beyond those responsible for propulsion, are necessary for the helical movement.

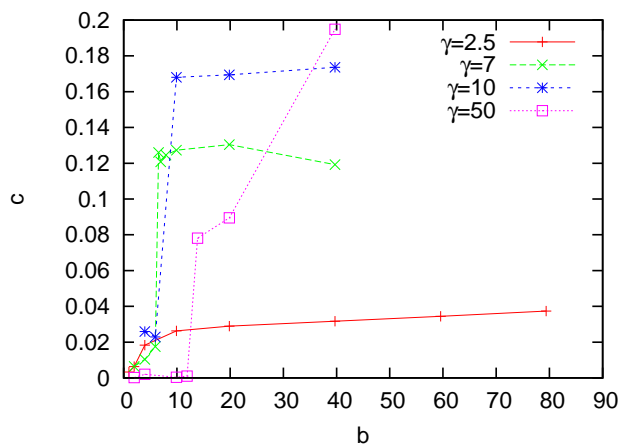


Figure 3.14: Curvature  $c$  of the helical trajectory as a function of bending parameter  $b$  for sperm simulations without hydrodynamics with  $\gamma_{\perp}/\gamma_{\parallel} = 2$ , for various friction coefficients as indicated.

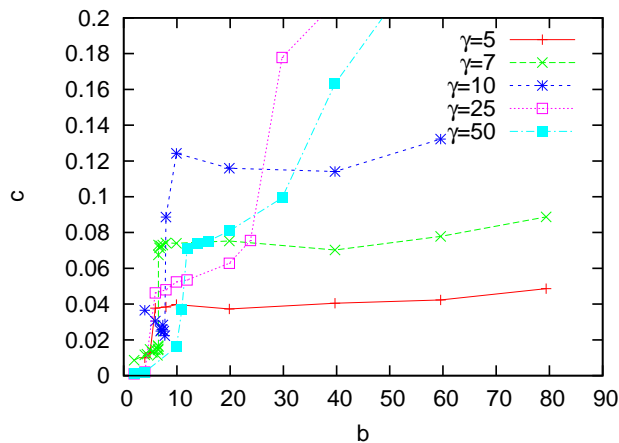


Figure 3.15: Curvature  $c$  of the helical trajectory as a function of bending parameter  $b$  for sperm simulations without hydrodynamics with  $\gamma_{\perp}/\gamma_{\parallel} = 1.33$ , for various friction coefficients as indicated.

### 3.2.3 Discussion

In bulk fluid, simulated sperm swim along helical trajectories. The helix parameters strongly depend on the asymmetry of the sperm. A change of the sperm shape causes a transition in the parameters of the trajectory as a function of the bending parameter. At the transition point the curvature, the director auto-correlation function, and the helix radius display a sudden increase. This transition is sharper in simulations without hydrodynamic interactions and thermal fluctuations. Figure 3.16 displays an overlay of snapshots from sperm simula-

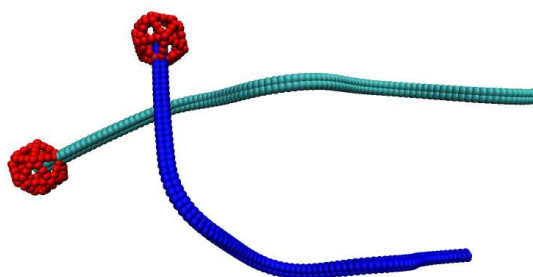


Figure 3.16: Overlay of snapshots from sperm simulations without hydrodynamics with bending parameters  $b = 6.51^\circ$  (cyan tail) and  $b = 6.53^\circ$  (blue tail),  $\gamma = 7, \gamma_\perp/\gamma_\parallel = 1.33$ . Visualization using VMD [38].

tions without hydrodynamics for two different bending parameters to visualize the transition. A slight increase from  $b = 6.51^\circ$  to  $b = 6.53^\circ$  leads to this drastic change in shape. We assume that the viscous forces on the sperm, especially the propulsive force of the tail and the drag of the head, cause internal stresses, that eventually break a threshold to bent the sperm further. Once they start to bent the sperm even further, the increased leverage leads to an even stronger deformation.

## 3.3 Confined Movement

Most experimental studies of sperm are performed in confined geometries. Interesting phenomena like accumulation of sperm at surfaces or their circular swimming at the surface are related to surface interactions. To study these phenomena, we simulated sperm between two planar walls, separated by a distance  $d = 50a$ . The results of these simulations are presented in this section. We begin

with some general observations, then turn our attention to surface adhesion and circular motion. Finally we discuss the increased velocity of sperm in thin films as observed in immersed boundary simulations by Fauci and McDonald [20].

### 3.3.1 General Observations

We observe a strong surface adhesion for sperm in all parameter regimes. Figure 3.17 shows the average distance  $d_h$  of the head from the wall, in units of the head radius.

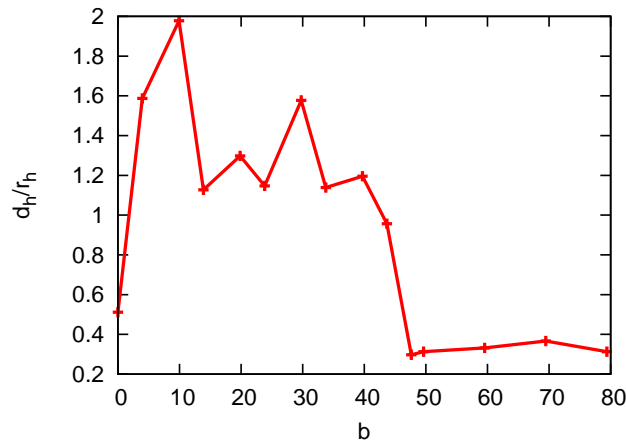


Figure 3.17: Average scaled surface distance  $d_h/r_h$  of the head versus bending parameter  $b$ .

For all bending parameters, the head is close to the surface. Besides one simulation, the sperm never left a surface after it had been close to it for a while. Therefore,

- hydrodynamic interactions are sufficient to capture the sperm at the surface. Direct attractive interactions between sperm and wall are not necessary for adhesion.

Furthermore, the trajectories illustrate that bent sperm move in oriented circles at the wall, always clockwise when observed from inside the fluid. Figure 3.18 shows a plot of the radius of these circles.

Figs. 3.17 and 3.18 give rise to two questions:

1. Why do sperm stay at the surface?

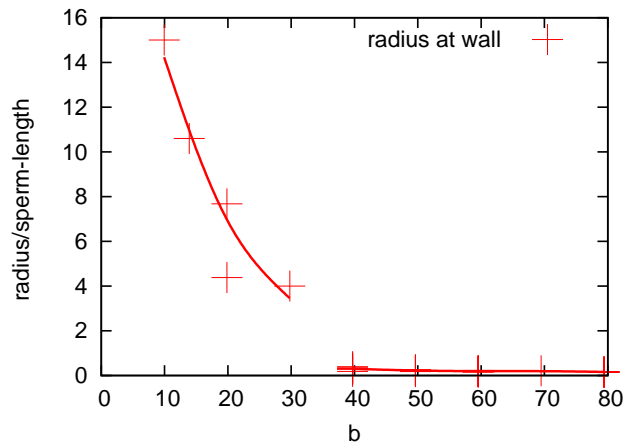


Figure 3.18: The radius of the circles drawn at the wall as a function of bending parameter. Solid lines are guides to the eye. The radius for the sperm close to the transition point ( $b = 40^\circ$  and  $44^\circ$ ) is determined while the sperm is in a regular motion close to the wall. Irregular motion (see Sec. 3.3.3 below) is ignored.

2. What is the origin of the strong dependence on the bending parameter?

We will address these questions in the following sections.

### 3.3.2 Surface Adhesion

Independent of the bending parameter, sperm stay at the surface. A histogram of the director to wall angle  $\alpha_d$  (see Figs. 3.19 and 3.20) shows that sperm, on average, point towards the surface. At small bending parameters, sperm are rather flat moving across the surface, while with increasing bending parameter its director angle towards the surface increases. Only the sperm with bending parameter of  $b = 40^\circ$  and  $44^\circ$ , being between the two regimes, show irregular paths and a broad peak in the director distribution.

The forward thrust of the sperm has a component  $F_\perp$  perpendicular to the wall. This component will keep sperm at the surface, provided it is pointing towards the surface (see Fig. 3.21). But because the reaction force of the wall acts on the head, we expect a torque, turning the sperm head away from the surface. This torque must be compensated by an interaction between the wall and the sperm tail, indicated by  $F_{tail}$  in Fig. 3.21.

Two interactions can be responsible for the necessary force on the tail:

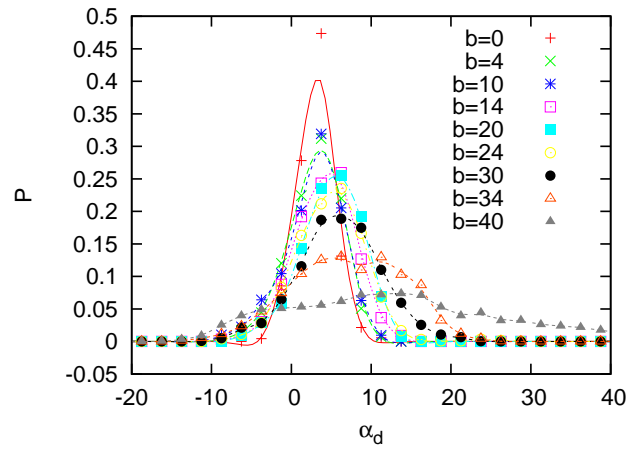


Figure 3.19: Probability distribution  $P$  of the director angle  $\alpha_d$  for sperm before the transition point ( $b < 40^\circ$ ), for various bending parameters, as indicated.

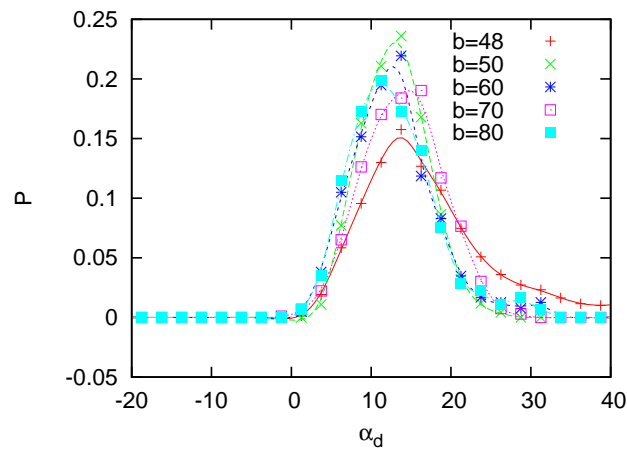


Figure 3.20: Probability distribution  $P$  of the director angle  $\alpha_d$  for sperm before the transition point ( $b > 40^\circ$ ), for various bending parameters, as indicated.

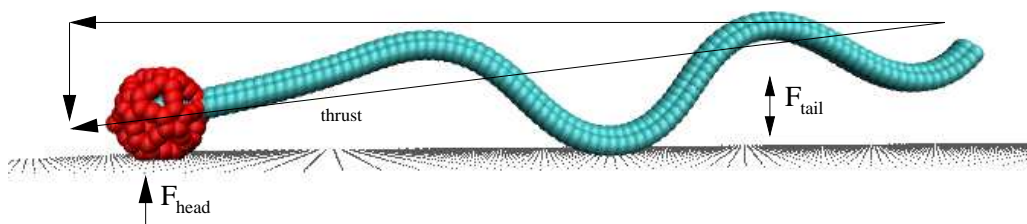


Figure 3.21: Forces between wall and sperm. Visualization using VMD [38].

- Hydrodynamic interactions between the wall and tail.
- Steric interactions. When parts of the oscillating tail hit the wall, they are repelled.

We simulated without hydrodynamics to distinguish between these effects. Figure 3.21 shows a snapshot from simulations without hydrodynamic interactions. The average distance from the wall for systems without hydrodynamics can be rather large (see Fig. 3.22).

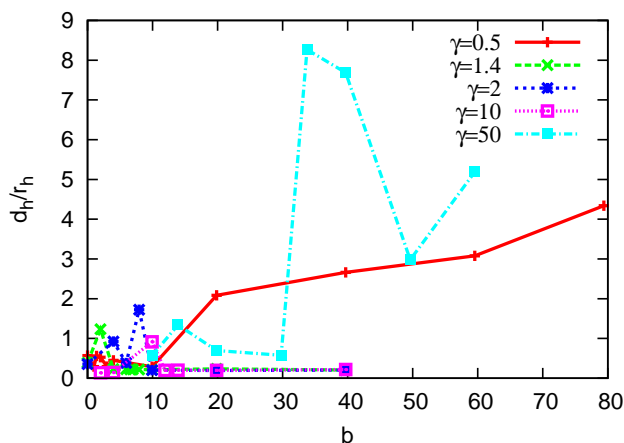


Figure 3.22: Average of scaled surface distance  $d_h/r_h$  of the head versus bending parameter  $b$  for sperm simulations without hydrodynamics with  $\gamma_{\perp}/\gamma_{\parallel} = 2$ , for various friction coefficients as indicated.

Obviously, the sperm can adhere to the surface without hydrodynamic interactions, although less tightly. In particular, there were many instances where the sperm regularly detached from the wall again.

Considering the sperm conformation, we observe another important effect: With hydrodynamic interactions, the non-bent sperm adheres with the beating plane parallel to the surface. In Fig. 3.23 we show a snapshot of a simulation with hydrodynamics. If the bending parameter vanishes, the beating plane is parallel to the surface. Obviously in this case hydrodynamic interactions are responsible for the adhesion.

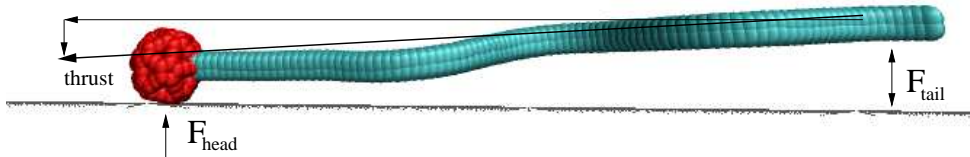


Figure 3.23: Simulation snapshot of a sperm with hydrodynamic interactions at a wall,  $b = 0$ . Visualization using VMD [38].

Furthermore, we can estimate the importance of steric interactions in the hydrodynamic simulations by determining the distance between the tail monomers and the wall. The distance between wall and monomer has to be smaller than the Lennard-Jones repulsion cutoff length of 0.25 for steric interactions to play a role. After wall adhesion, we detect only few instances where a monomer is closer to the surface than the cutoff length. These instances were only found in the regime of intermediate bending parameters near the transition where the sperm behaves erratically (see Fig. 3.34 in Sec. 3.3.3). In both, the strongly and weakly bent regimes, the sperm tail does not touch the wall.

We conclude that hydrodynamic interactions are responsible for the surface adhesion by *repelling* the tail sufficiently far from the wall. This repulsion creates a torque, turning the head, and thus the thrust, towards the wall.

### Rocket-Model

In order to understand these results better, we introduce a simplified model in which the sperm is described as a self-propelling rod. In the rocket-model

(see Sec. 2.3) the sperm is a rod, propelling itself forward by pushing the fluid around it backwards. We simulate these rods with and without hydrodynamics. Because in the short simulation times accessible with hydrodynamics the results did not differ significantly from those without hydrodynamics, we only present the results for simulations without hydrodynamic interactions. Fig. 3.24 shows the  $z$  component of the rods center of mass for a short time section for a typical run. Clearly the rod is more often close to the wall than in the center of the

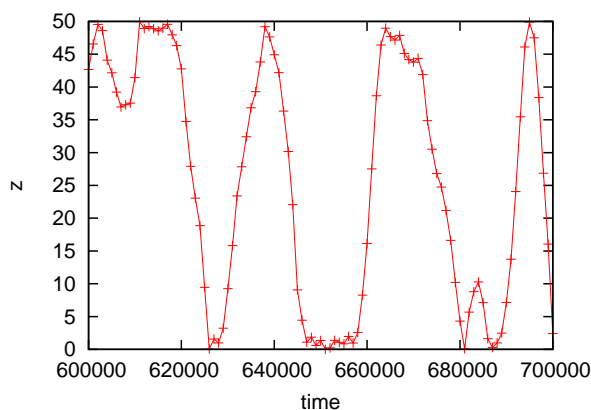


Figure 3.24:  $z$  component of the center of mass of a hydro rocket with  $F_t = 5$ . Rod length is  $10a$  and the walls are at  $z = 0a$  and  $z = 50a$ .

fluid film, but it does not stay at the wall almost all the time like the sperm in both previous models. To quantify the surface localisation we define the surface excess,

$$s = \int_0^\infty [P(z) - P(\infty)] dz \quad (3.5)$$

where  $P(z)$  is the probability density to find the rod at a distance  $z$  from the surface and  $P(\infty)$  is the bulk probability density. Examples of  $P(z)$  are given in Figure 3.25.  $P(\infty)$  is measured in the simulations by averaging the probability density in the range  $z > 10$ .

$$P(\infty) = \frac{1}{d/2 - 10} \int_{10}^{d/2} P(z) dz \quad (3.6)$$

Thus  $s = 0$  is a homogeneous distribution, while  $s = 1$  is a delta distribution at the wall.

In Fig. 3.26 we plot the surface excess for different parameters. As expected the unpropelled rods  $F_t = 0$  show negative surface excess due to depletion

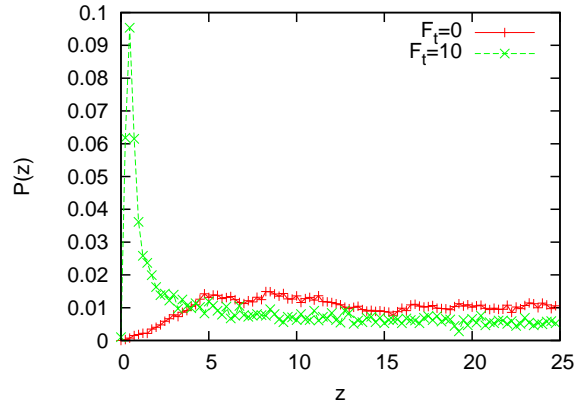


Figure 3.25: Probability density  $P(z)$  function of the hydrorocket being at different distances  $z$  from the surface for unpropelled rods (red) and a hydrorocket model with  $F_t = 10$ . Rod length  $L$  is  $10a$  and the walls are at  $z = 0a$  and  $z = 50a$ .

interaction. The errors for the unpropelled rods are rather large due to its slow movement. The propelled rods show a strong surface excess of about 40%, decreasing for very small rodlengths ( $L < 10a$ ) towards 0. There is a small maximum, depending on the propulsive force.

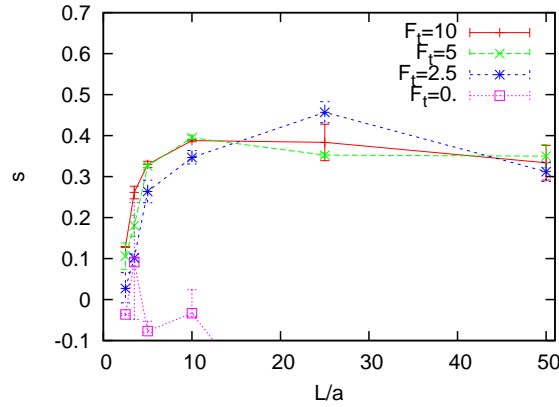


Figure 3.26: Surface excess  $s$  as a function of scaled rod length  $L/a$ , for different Forces per monomer bond as indicated. Wall distance is  $50a$ . Errorbars are results of two independent runs.

These simulations fit perfectly with our repulsion-adhesion hypothesis. In the rocket model, the tail is not repelled by the wall (besides the Lennard-Jones repulsion acting on all monomers). Without steric repulsion, only the reaction

force onto the tip of the rod creates a torque, but this time turning the rocket away from the surface. Therefore it leaves the wall after a while.

As a final check of our adhesion theory we have modified the rocket model, by adding a repulsive, constant force at the end of the rod. In the vicinity of the wall ( $d < 5a$ ) the three monomers at the end of the rod experience a repulsive force of magnitude  $f_w$ . By varying  $f_w$  we see a transition towards surface adhesion. Fig. 3.27 shows the reciprocal normalized average time at the wall ( $\tau_w(0)/\tau_w(f_w)$ ) versus the repulsive force  $f_w$ .

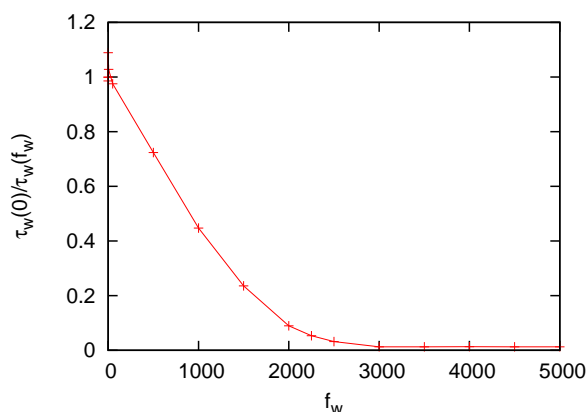


Figure 3.27: Reciprocal normalized average time at the wall ( $\tau_w(0)/\tau_w(f_w)$ ) versus the repulsive force  $f_w$ .  $L_r = 10$ ,  $d = 50$ .

### Discussion

By studying sperm motility, we have identified an adhesion mechanism that can be generalized to self-propelled particles. The mechanism of adhesion requires:

- unidirectional self propulsion, i.e. the propulsion must point in the direction of the particle orientation.
- Tail repulsion, i.e. the back end of the particle has to be repelled from the wall with a stronger force and a longer range than the front end.

The mechanism of adhesion can be described in the following way: the thrust  $\vec{F}_t$  has a component  $\vec{F}_\perp$  towards the wall (see Fig. 3.28). While  $\vec{F}_\perp$  keeps the particle at the surface, the reaction force  $\vec{F}_r$  of the wall creates a torque  $\vec{T}_r$ , turning the sperm's head away from the surface. Eventually this torque is compensated by the torque  $\vec{T}_w$  created by the repulsion  $\vec{F}_w$  of the tail. Now,

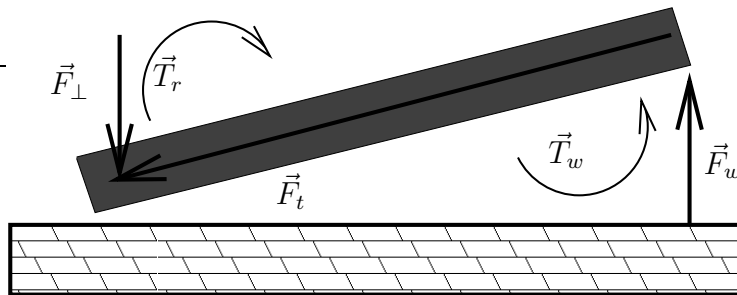


Figure 3.28: Scetch of forces responsible for adhesion, see text.

the system is in a stable state, where small fluctuations are quickly undone. If, for example, a fluctuation turns the head further away from the surface, this reduces  $\vec{F}_\perp$  which in turn reduces  $\vec{F}_r$  and  $\vec{T}_r$ . Therefore,  $\vec{T}_w$  is now larger than  $\vec{T}_r$ , turning the head back to its dynamic-equilibrium position. Only if the fluctuations are large enough to get the sperm cell out of reach of the wall repulsion, the sperm can detach. For this to happen, both the range and the magnitude of the repulsion are important, because they define the time within which the sperm is driven back to its dynamic-equilibrium position.

For sperm, the propulsion is caused by the beat of the flagellum, which at the same time repels the tail from the wall, causing adhesion. We have shown that this adhesion is stable even under strong thermal fluctuations. No other surface interaction or aplanar beat pattern is necessary to explain this effect!

Sperm can adhere even without hydrodynamic interactions, as long as propulsion is possible through asymmetric friction. Tail repulsion is then achieved by steric interactions. However, this adhesion is not as strong as with hydrodynamic interactions.

Another example of this adhesion mechanism was found for self-propelled rods with a constant tail repulsion. Here even the transition between adhesion and no adhesion as a function of the repulsive force can be observed.

This adhesion mechanism is rather universal and could also explain the adhesion of bacteria at solid walls. Other explanations like interactions between rotating helices and solid boundaries [55] are limited to rather specific systems.

### 3.3.3 Regimes of Motion

As outlined at the beginning of this chapter, two regimes of motion can be identified for sperm swimming close to a wall - the strongly and weakly bent

regime. In the strongly bent regime, the head is less than 0.2 head diameters away from the wall (see Fig. 3.17). In the weakly bent regime, the head is much farther away. This difference can be reflected in many other features of the trajectory as well.

The radius of the circular trajectory at the wall becomes much larger for weakly bent than for strongly bent sperm (see Fig. 3.18). This is the opposite of what we have observed for the helix radius of the freely moving sperm. Strongly bent sperm follow trajectories with small circles with a diameter of about half a sperm length. On the other hand, weakly bent sperm draw circles almost an order of magnitude larger than those with large bending parameter. The radius decreases with increasing bending parameter, but at the transition point a radius is difficult to define, because sperm move erratically, as shown at the end of this section.

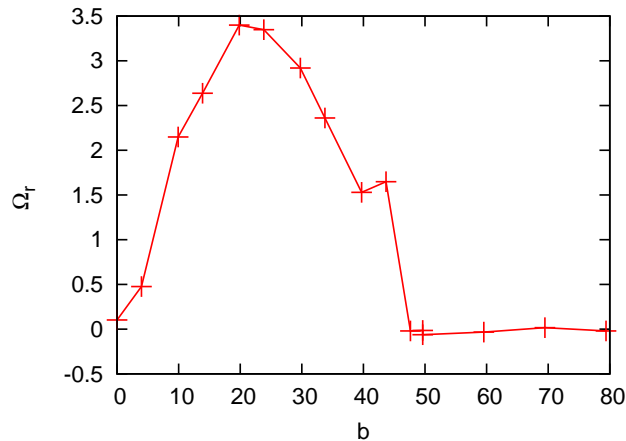


Figure 3.29: Rotation frequency  $\Omega_r$  vs. bending parameter. Only moderately bent sperm rotate at the wall. Weakly bent sperm do not rotate, strongly bent ones can not rotate at the wall.

In a plot of the sperm's rotation frequency  $\Omega_r$  at the wall (see Fig. 3.29), the difference between regimes becomes quite clear. Strongly bent sperm (bending parameter  $b \geq 45^\circ$ ) do not rotate at the wall. Their beating plane stays perpendicular to the surface for a long time.

These features can be analyzed further by a histogram of the wall-angle distribution  $p(\alpha_w)$  defined in Sec. 3.1. For strongly bent sperm, we observe a large peak at  $\alpha_w \approx 260^\circ$  in the wall angle distribution function (see Fig. 3.30) which corresponds to the beating plane being perpendicular to the surface. At this

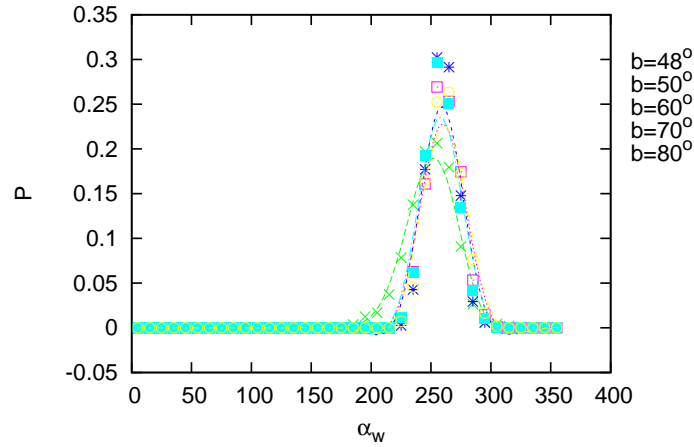


Figure 3.30: Probability distribution  $P$  of the wall angle  $\alpha_w$  for strongly bent sperm, for various bending parameters as indicated.

point the head is touching the surface, blocking further turns. In a snapshot of the simulation, we observe how the beating plane is perpendicular to the surface, and how the head touches the wall (see Fig. 3.31).

Weakly bent sperm ( $b < 45^\circ$ ) roll while at the surface (see Fig. 3.29). With increasing bending parameter, the sperm rotates faster until at approximately  $b = 20^\circ$  it reaches a maximum. After this point, the head starts to get stuck at the surface for short periods of time, thus slowing down the rotation.

Again these features are also reflected in the wall-angle distribution function  $p(\alpha_d)$ . Straight, or only slightly, bent sperm align with the beating plane parallel to the surface. In the wall-angle distribution function  $p(\alpha_w)$ , we observe peaks at 0 and 180 degrees (see Fig. 3.32 ).

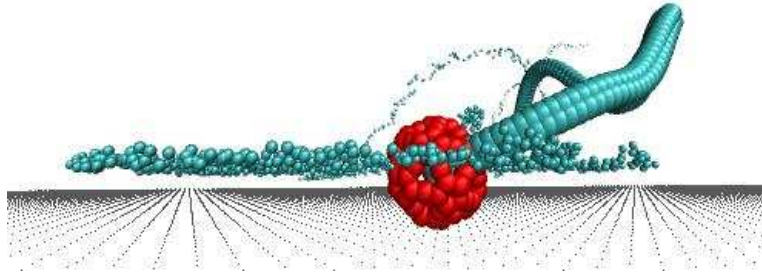


Figure 3.31: Strongly bent sperm (bending parameter  $60^\circ$ ) at a surface. The head touches the wall blocking further rotations. The beating plane is perpendicular to the surface. Visualization using VMD [38].

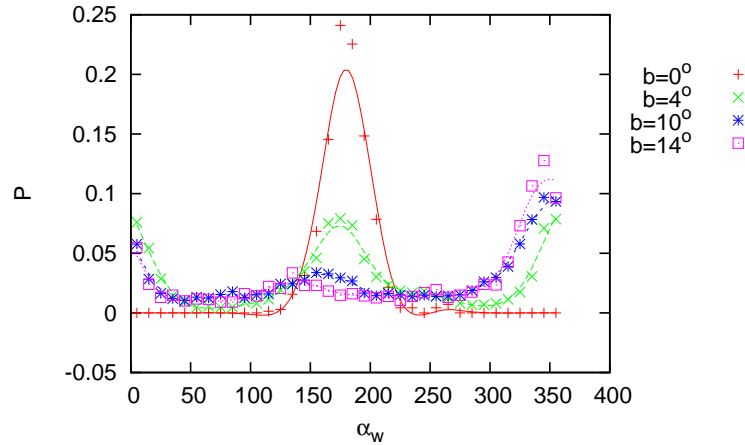


Figure 3.32: Probability distribution  $P$  of the wall angle  $\alpha_w$  for slightly bent sperm, for various bending parameters as indicated.

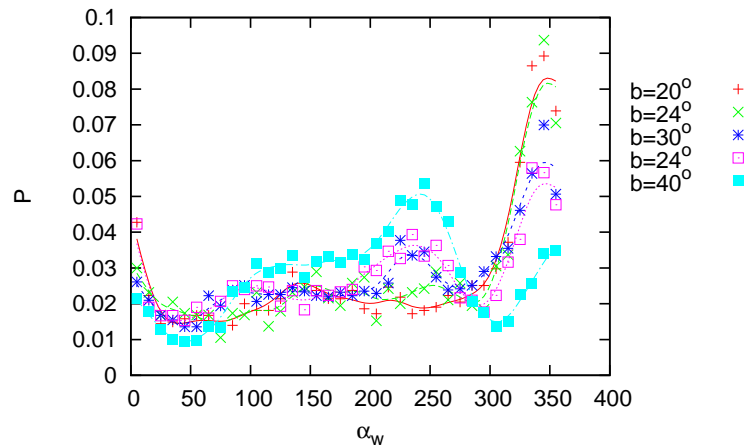


Figure 3.33: Probability distributions  $P$  of the wall angle  $\alpha_w$  for moderately bent sperm, for various bending parameters as indicated.

For moderately bent sperm ( $20^\circ \leq b \leq 40^\circ$ ), Fig. 3.33 shows a broad distribution. Peaks at  $\alpha_d = 0^\circ$  and  $\alpha_d = 180^\circ$  are still visible, but now there is also a peak at  $\alpha_d = 260^\circ$ , which indicates that the head gets stuck for a short time, when it touches the surface.

Close to the transition point ( $b \approx 45^\circ$ ), the sperm behaves irregular. The trajectory is not a regular circle, but occasionally has abrupt turns (see Fig. 3.34). Furthermore, it is of interest that only in this intermediate bending parameter regime (in the simulation with  $b = 30^\circ$ ) we observed that a sperm, being at one wall for a while, detached and moved to the opposite wall.

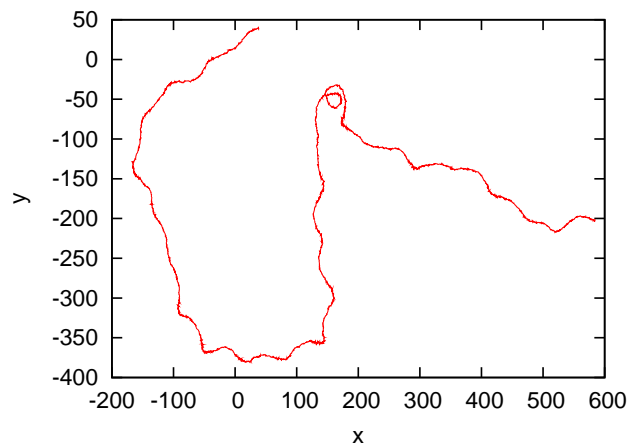


Figure 3.34:  $x$  and  $y$  component of the trajectory of the sperm with bending parameter  $b = 40^\circ$ .

### Discussion

The oriented circular motion is caused by the chirality of the sperm. This is illustrated for the strongly bent sperm. Figure 3.35 shows a strongly bent sperm (bending parameter  $60^\circ$ ) at the surface. The sperm “wants” to swim on a helical trajectory, but because the head hits the surface it cannot rotate. A torque on the sperm is generated by the appropriate reaction force, bringing the sperm onto a circular trajectory.

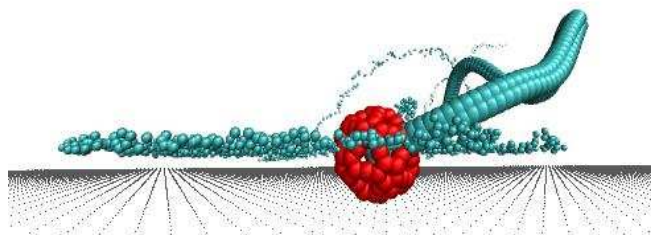


Figure 3.35: Strongly bent sperm (bending parameter  $60^\circ$ ) at surface. The head touches the wall and thus causes a bending moment on the sperm. Visualization using VMD [38].

In the weakly bent case, we observe that even at the surface the sperm rotates around itself. But still the head hits the wall periodically. In other words, the head touches the surface for a short time, exerts a little torque to bring the sperm onto a circular trajectory, but then slips through and goes straight for

another short bit. Thus we get a significantly larger radius of curvature.

At the transition point, the head can get stuck for long times until thermal fluctuations cause it to slip through once, creating this “erratic” behavior.

### 3.3.4 Velocity in Thin Films

We simulate sperm with a bending parameter  $b = 0$  in thin films. The separation  $d$  of the to infinite planes is varied  $5 < d < 50$ , and the swimming velocities are compared with the theoretical expression provided in Ref. [20],

$$v(d) = \frac{1}{c_1 d + c_2}. \quad (3.7)$$

As expected and explained in Ref. [20], this equation performs poorly for large wall separations  $d$ , because it results in  $v = 0$  for infinite wall separation. Adding another fitting parameter  $c_3$  to Eq.(3.7) works, not surprisingly, due the many fitting parameters.

Figure 4.21 displays a plot of the sperm swimming velocity as a function of channel width  $d$  and a fit to the latter expression. A clear peak is visible for a wall separation of  $7a$ , about 10% larger than free swimming velocity.

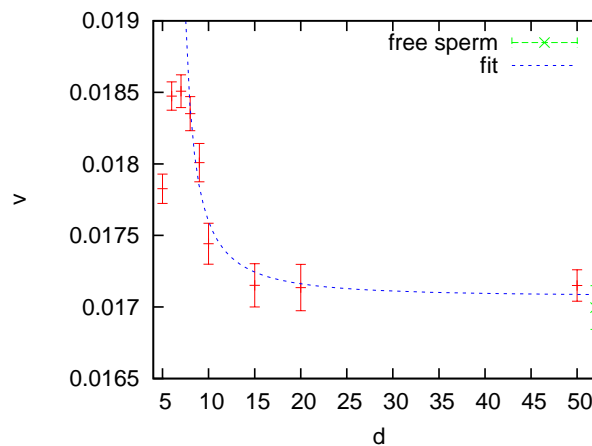


Figure 3.36: Swimming velocity  $v$  in a thin film of width  $d$ . In green we depicted the swimming velocity for a free sperm. The blue line is a fit of  $v(d) = \frac{1}{c_1 d + c_2} + c_3$  to the data in the range  $8 \leq d \leq 50$

Fig. 4.21 clearly shows the limits of the analytical expression for channel widths smaller than the beating amplitude. These channel widths are of course

not accessible in two-dimensional simulations where the beating plane is perpendicular to the surface. Three important differences between the theory and our simulations explain why the theory does not work so well. Besides our simulations being three-dimensional, our sperm swim with the beating plane parallel to the surface. Furthermore, the sperm swim, even at large wall separations, close to one wall, thus the swimming velocity is still enhanced compared to the free case, but not influenced by the wall separation anymore. However, it is interesting to note that the sperm swim faster in a thin film than in a free fluid.

## 4 Cilia Results

In this chapter, the simulation results for cilia arrays are presented. The main objective is to understand the formation of the metachronal wave, its parameters like the wavelength  $\lambda$ , and the effect of the metachronal wave on fluid transport and efficiency. We first introduce a way to quantify the metachronal wave and continue with simulation results for the influence of different input parameters on the wave characteristics. Finally, we turn our attention towards transport and efficiency, and how these are influenced by metachronal coordination.

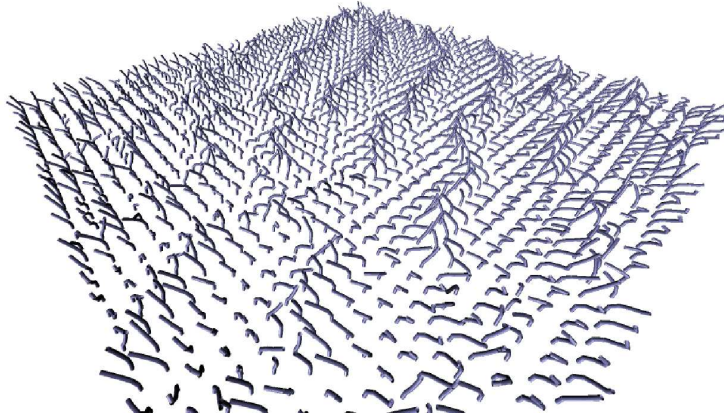


Figure 4.1: Simulation snapshot ( $40 \times 40$  cilia,  $h = 0.02$ ). Visualization using VMD [38].

### 4.1 How to Characterize Metachronal Waves

The metachronal wave can be seen nicely in simulation snapshots (see Fig. 4.1), but these waves look different in different systems, even within the same simulation at different times. Sometimes it is difficult to see whether metachronal coordination is present. In movies of most simulations, we see how the wave

develops in time. After the system has been started with all cilia in the same phase, regions of uncorrelated movement quickly grow, until, after some time, a metachronal wave appears. Quantification of the metachronal wave and its effects is the purpose of this section.

To characterize a metachronal wave, we need a scalar quantity for the phase of the beat. For this purpose we define the beat status

$$B = \cos(\Theta)\Delta x + \sin(\Theta)\Delta y \quad (4.1)$$

where  $\Delta x = x(\text{tip}) - x(\text{base})$   $\Delta y = y(\text{tip}) - y(\text{base})$  are the relative displacements of the tip of the cilium to its base. The direction of the effective stroke (see Fig. 4.2) is given by  $\Theta$ .  $B$  is the displacement of the tip in the direction of the effective stroke. The oscillations of the cilia can nicely be seen in the beat status

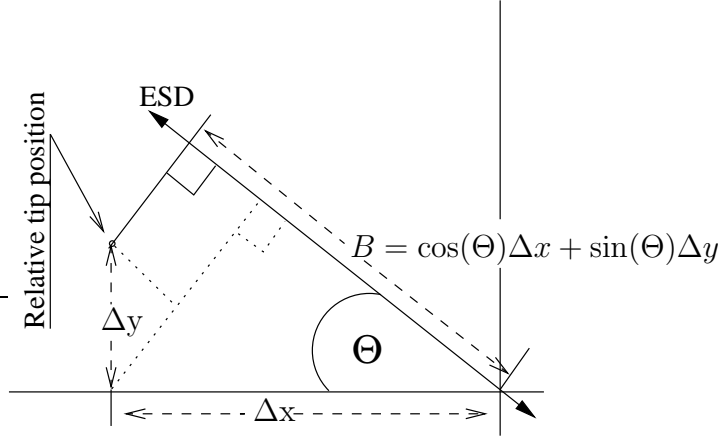


Figure 4.2: Definition of the beat status  $B$

(see Fig. 4.3). In movies of the beat-status field, the metachronal wave can be seen as well as in simulation snapshots.

The beat status is a scalar field, and allows a detailed analysis via correlation functions or Fourier transforms. The full correlation function  $G_c$  in  $x$ ,  $y$  and  $t$  has proven to be very effective. It is defined by

$$G_c(\Delta x, \Delta y, \Delta t) = \left\langle B^*(x, y, t) \cdot B^*(x + \Delta x, y + \Delta y, t + \Delta t) \right\rangle / \sigma^2 \quad (4.2)$$

where  $B^* = B - \langle B \rangle$ ,  $\sigma^2 = \langle B^2 \rangle - \langle B \rangle^2$  is the variance of  $B$  and the average runs over all cilia and 300 simulation snapshots, each  $100h$  apart.  $x$  and  $y$  indicate which cilium (counted in integer numbers) in  $x$  or  $y$  direction, accordingly  $\Delta x, \Delta y$  denote a displacement in the corresponding coordinate.

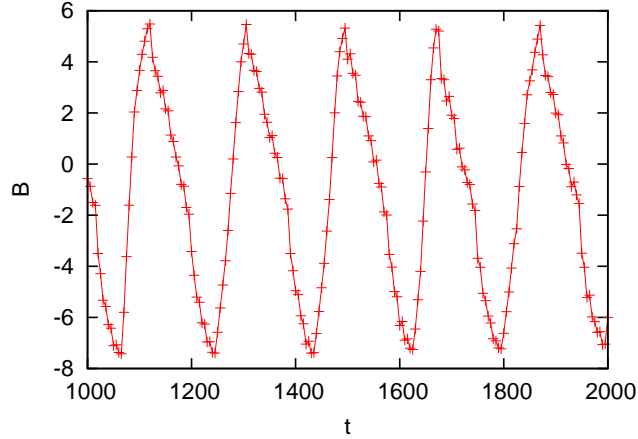


Figure 4.3: Beat status  $B$  of one cilium in the reference system as a function of time  $t$

How could this correlation function look like? First of all, if the cilia are coupled to a metachronal wave, it should be proportional to a cosine-like function

$$G_c(\Delta\vec{r}, \Delta t) \propto \cos(\vec{k} \cdot \Delta\vec{r} - \omega\Delta t). \quad (4.3)$$

where we restrict the angular frequency  $\omega$  to be positive, so the metachronal wave runs in the direction of the wave vector  $\vec{k}$ .

Because the wave is not perfect, having thermal fluctuations and defects like dislocations, it should decay with distance according to

$$G_c(\Delta\vec{x}, \Delta t) \propto \exp(-\sqrt{\Delta\vec{x}\mathfrak{X}\Delta\vec{x}}), \quad (4.4)$$

which is the two dimensional equivalent to  $\exp(-r/\xi)$  with elliptical symmetry, with a symmetric matrix  $\mathfrak{X}$ . The decay lengths  $\xi_{1/2}$  along the eigenvectors  $\hat{e}_{\lambda_{1/2}}$  are related to the eigenvalues  $\lambda_{1/2}$  of  $\mathfrak{X}$  by  $\xi_{1/2} = (\lambda_{1/2})^{-\frac{1}{2}}$ . The eigenvectors  $\hat{e}_{\lambda_{1/2}}$  represent the direction of weakest (subscript 1) and strongest (subscript 2) correlation, respectively.

It is not clear that the correlation has to have a finite correlation range. In principle long range and quasi long range correlations are also possible. As a first approximation we introduce a additive constant  $c_1$  that limits the decay of the correlation function.

$$G_c(\Delta\vec{x}, \Delta t) \propto (1 - c_1) \exp(-\sqrt{\Delta\vec{x}\mathfrak{X}\Delta\vec{x}}) + c_1 \quad (4.5)$$

From the simulations presented, it is not possible to distinguish whether a finite  $c_1$  stems from (quasi) long range correlations or finite size effects. Often we

observe the metachronal wave developing from a small domain, growing with time eventually over the system size. Thus, a large value of  $c_1$  indicates that finite-size effects are important (see Sec. 4.13). In the simulation results presented here,  $c_1$  is typically of the order of 0.1, but may vary between 0 and 0.5.

Of course the correlation function will also decay with time, thus:

$$G_c(\vec{\Delta x}, \Delta t) \propto \exp(-\Delta t/\tau) \quad (4.6)$$

Separate measurements of the decay time  $\tau$  (see Sec. 4.4) show that  $\tau$  is of the order of a few thousand  $\sqrt{ma^2/k_b T}$ . Due to the computational effort we determine the full correlation function  $G_c(\vec{\Delta x}, \Delta t)$  only up to  $\Delta t = 400\sqrt{ma^2/k_b T}$ . Hence we neglect the factor  $\exp(-\Delta t/\tau)$  in this short time analysis.

Combining Eq.(4.3) and Eq.(4.4) we get

$$G_c(\vec{\Delta x}, \Delta t) = \cos(\vec{k} \cdot \vec{\Delta x} - \omega \cdot \Delta t) \left[ (1 - c_1) \exp(-\sqrt{\vec{\Delta x} \mathfrak{X} \vec{\Delta x}}) + c_1 \right] \quad (4.7)$$

After some equilibration time, Eq.(4.7) describes correlations very well, leading to  $\chi^2$  less than 1, where

$$\chi^2 = \frac{\langle \left[ G_c(\Delta \vec{r}, \Delta t) - X(\Delta \vec{r}, \Delta t) \right]^2 \rangle}{\sigma^2(X)} \quad (4.8)$$

is the  $\chi^2$ -errorfunction,  $X$  the simulation result for  $G_c$ . A typical picture of a cut through the correlation function can be seen in Fig. 4.4. The quality of the fit can be seen better along just one axis (see Fig. 4.5), the agreement is excellent.

The good quality of the fit of Eq. (4.7) allows now a *detailed characterization of the metachronal wave*. This analyzing scheme is also well suited for experimental data provided a scalar quantity for the beat phase can be obtained. The fit leads to accurate, well defined measures. Other measures can be derived from these parameters. For example, Ref. [22] uses basically

$$\sup_{0 \leq \Delta t \leq \tau_b} \left( G_c(\vec{\Delta x}, \Delta t) \right) \quad (4.9)$$

(where  $\tau_b$  is the period of the ciliary beat). Together with the information which  $\Delta t$  belongs to the supremum,  $\vec{k}$  and other parameters can be computed. But because not all information of the measurements are used, larger errors can be expected.

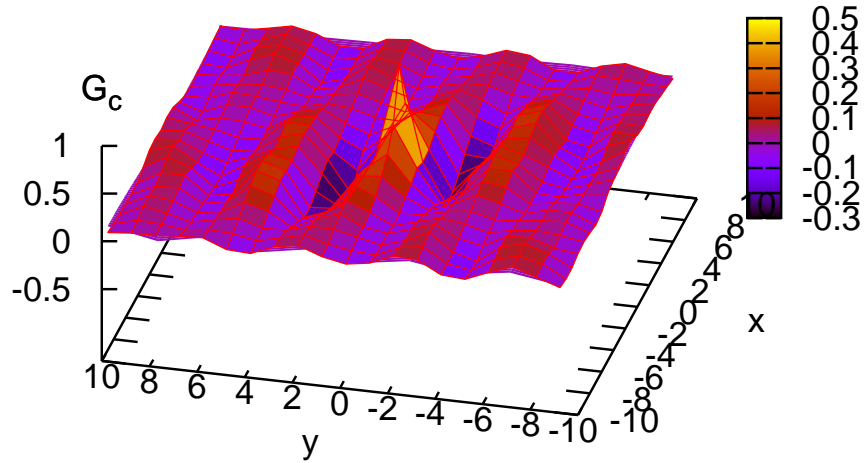


Figure 4.4: Cut through the correlation function at  $\Delta t = 0$ . Simulation results (red lines) and fit (colored surface) for the reference system. Color scheme indicates values of  $G_c$ .

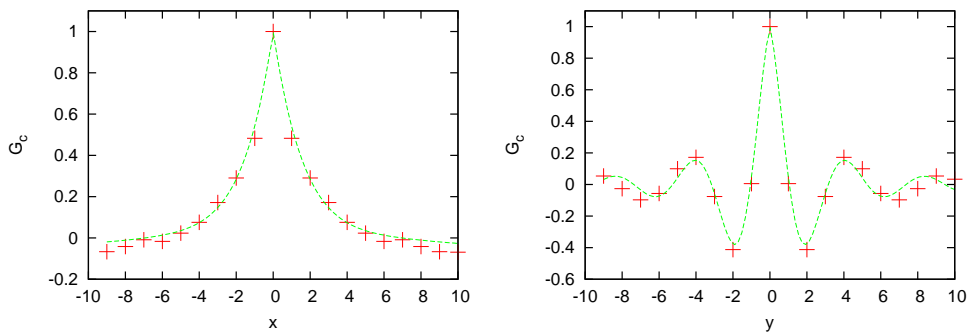


Figure 4.5: Cut through the correlation function at  $t=0$ . Fit (line) and simulation data (points) for the reference system.

## 4.2 Extraction of Metachronal Wave Effects

In the reference system (see Sec. 2.4.2), and thus in most simulations, an array of  $20 \times 20$  cilia is simulated. This number of cilia is sufficient for a metachronal wave to develop.

To study the effect of metachronal coordination it is useful to have a closely related system, in which the development of metachronal coordination is prohibited. We call these cilia systems *synchronous beating*. For this purpose, we simulate a single cilium with periodic boundary conditions, which represents a unit cell of an infinite system where all cilia beat synchronously, while all other input parameters are identical.

## 4.3 Beat Period

The beat of the cilium is slowed down by the drag of the fluid. Because we drive the cilia by internal forces we expect the beat period  $\tau_b$  to depend linearly on the viscosity  $\eta$ . This linearity on the viscosity is reproduced in simulations (see Fig. 4.6). Because the cilium also has to overcome internal friction and has a predefined recovery stroke speed (see Sec. 2.4.1) we find a finite period  $\tau_b$  if extrapolated to  $\eta = 0$ .

The internal friction can be understood in the following way. With vanishing viscosity, energy put into the system by changing the bond length dissipates into vibrational modes of the monomers. This energy dissipation, along with the decay of the vibrational modes due to the thermostat, cause an internal friction of the axoneme structure.

While beating synchronously the fluid moves with the beat of the cilium, slowing it down less than the cilia in metachronal coordination. The latter feel the opposing flow of neighboring cilia. This is also seen in simulations (see Fig. 4.6), including the fact that this effect should disappear as the viscosity approaches zero.

The distance  $d_c$  between cilia has a different effect on synchronously beating cilia than on cilia in metachronal coordination. The larger the system, the more fluid has to be moved by each cilium, slowing down synchronously beating cilia. On the other hand, a cilium in metachronal coordination feels the opposing flow of its neighbors less the larger the distance, thus beating faster. Therefore the period decreases slightly with increasing distance (see Fig. 4.7) for metachronal

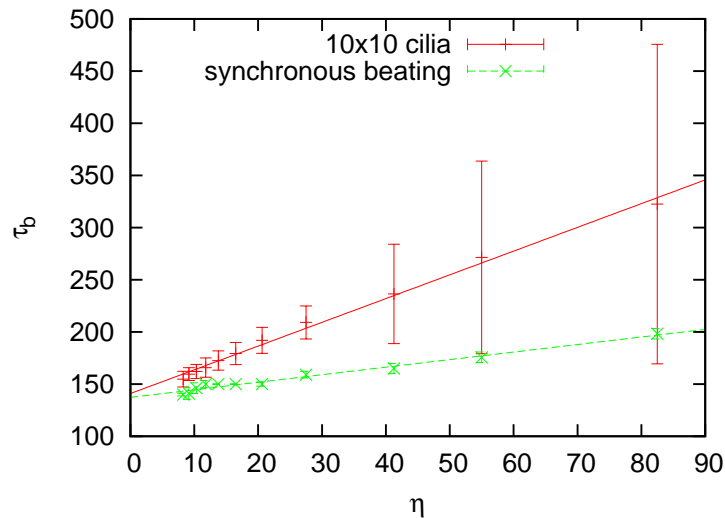


Figure 4.6: Mean beat period  $\tau_b$  of the cilia as a function of viscosity  $\eta$  with linear fit (solid lines) for systems of  $10 \times 10$  cilia and synchronous systems. All other parameters are according to the reference system. Error bars indicate the standard deviation of the distribution of periods for a single cilium. The standard error of mean is too small to be visible.

coordinated cilia, while it decreases for synchronously beating cilia. Also both approach the same value with larger distance, in agreement with above argument.

For synchronous beating cilia the period is not effected by the effective stroke direction. However, the period is found to be essentially independent of the effective stroke direction for cilia in metachronal coordination (see Fig. 4.8). We expect that the orientation of the cilia beat with respect to the lattice influences the metachronal wave and thus the period.

Furthermore, we notice that the standard deviation of the period is by far smaller for synchronous beating cilia then for cilia arrays (see Fig. 4.6, Fig. 4.7 and Fig. 4.8). The reason for this is that the synchronously beating cilia can stabilize their own beat, while the fluctuating metachronal wave may significantly influence the beat pattern.

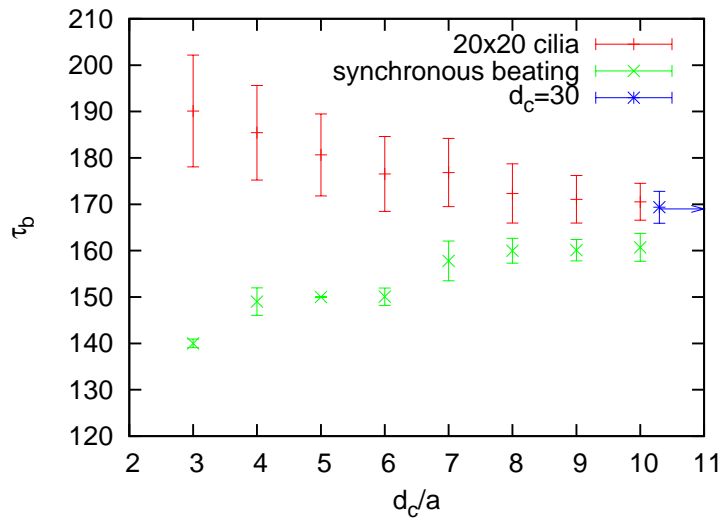


Figure 4.7: Period  $\tau_b$  versus cilia spacing  $d_c$ . All other parameters are according to the reference system. The data point indicated by the blue symbol is obtained for a synchronous system with  $d_c = 30$ . Error bars as in Fig. 4.6.

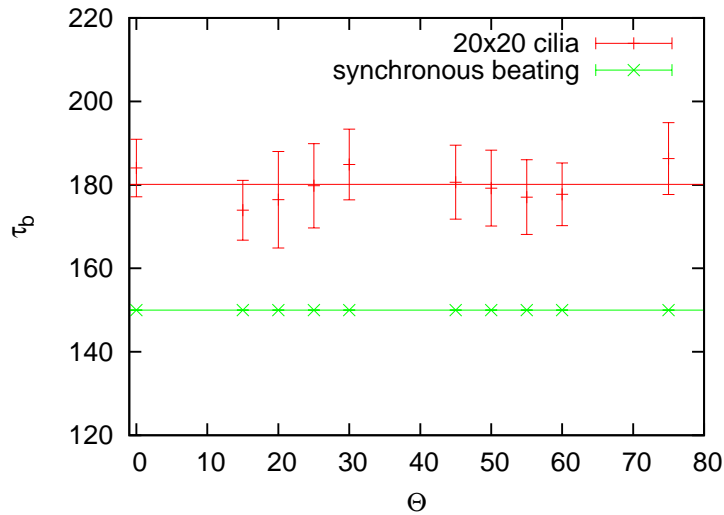


Figure 4.8: Period  $\tau_b$  versus effective stroke direction  $\Theta$ . All other parameters are according to the reference system. Error bars as in Fig. 4.6.

## 4.4 Auto-Correlation Function

The correlation function should decay as a function of time,

$$G_c(\vec{\Delta}x, \Delta t) \propto \exp(-\Delta t/\tau). \quad (4.10)$$

We focus here on this time decay the auto-correlation function

$$G_A(\Delta t) = G_c(\vec{0}, \Delta t) \quad (4.11)$$

because its timescale  $\tau$  is too large for a fit together with the space dependence. We fit simulation data to

$$G_A(\Delta t) = \cos(\omega\Delta t) \exp(-\Delta t/\tau) \quad (4.12)$$

via the angular beat frequency  $\omega$  and the decay time  $\tau$ .

For most simulations a fit of the auto-correlation function to Eq. (4.12) via  $\tau$  and  $\omega$  works very well. As an example, the auto-correlation function of the reference system is shown in Fig. 4.9. The result for  $\tau$  is typically on the order of a few  $1000\sqrt{ma^2/k_bT}$ . We could not find a systematic dependence of the decay time  $\tau$  on the parameters used.

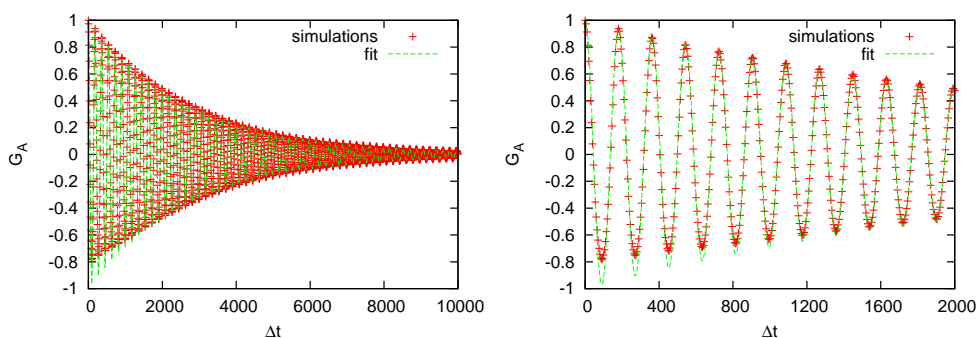


Figure 4.9: Auto-Correlation function  $G_A(\Delta t) = \cos(\omega\Delta t) \exp(-\Delta t/\tau)$  of the reference system. Fit with  $\tau = 2708$ ,  $\omega = 0.035$ . The right figure shows the short-time behavior in more detail.

However, the picture is not as simple for all systems. Some systems show additional oscillations on long timescales. The system with a cilia spacing of  $3a$  (see Fig. 4.10) shows further oscillations with a period of roughly  $2500\sqrt{ma^2/k_bT}$ . This could be explained by two oscillations contributing to the correlation function, similar to the beat heard when the sound waves of two tuning forks with

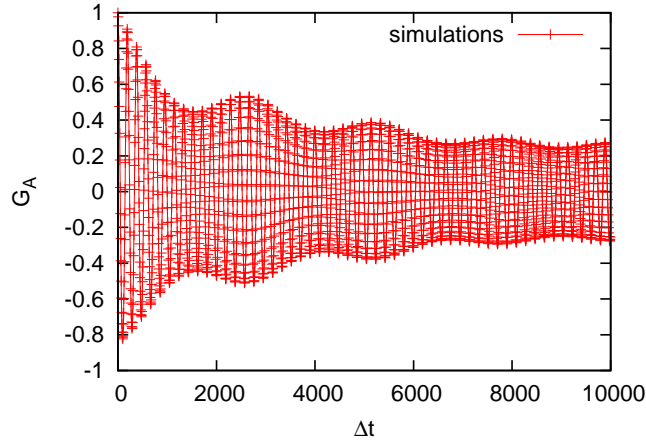


Figure 4.10: Auto-Correlation function  $G_A(\Delta t)$  for cilia spacing  $d_c = 3a$ .

slightly different frequency overlap. Additional oscillation frequencies found in the Fourier transform of the beat status of a single cilium (see Fig. 4.11) are a good indication for this hypothesis.

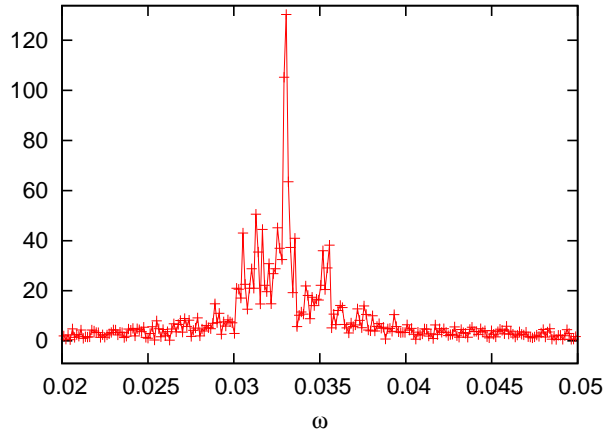


Figure 4.11: Fourier transform of the beat status of a single cilium from the simulations with cilia spacing  $d_c = 3a$ .

The synchronous cilia systems show almost no decay of the auto-correlation function within the simulation time. If a decay time  $\tau$  could be identified, it is larger than  $5000\sqrt{ma^2/k_bT}$ . It seems that due to the periodic boundary conditions the single cilium stabilizes its own beat. This fits with the observation of Sec. 4.3 that the variance of the beat period in these systems is very small.

## 4.5 Wavelength

The wavelength varies between  $\lambda = 10a$  and  $\lambda = 40a$ . No systematic dependence of the wavelength on the input parameters could be found (see Fig. 4.12), although the wavelength seems to increase with cilia spacing for  $d_c > 6a$ .

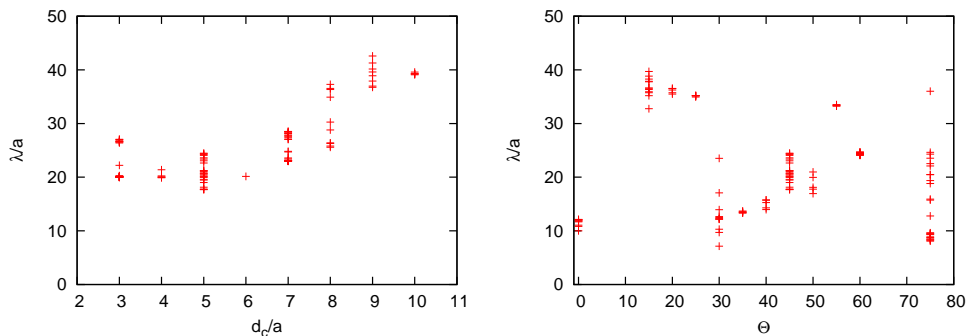


Figure 4.12: Scaled wavelength  $\lambda/a$  as a function of cilia spacing  $d_c$  (left) and effective stroke direction  $\Theta$  (right).

The wavelength is probably strongly effected by finite-size effects. The wave has to be commensurate with the cilia grid. In other words, the wave vector  $\vec{k}$  is restricted to the reciprocal lattice. If the systems “optimal”  $\vec{k}$ -vector is between two reciprocal lattice points, it chooses one of them randomly, but a small change in one parameter can suddenly favor a wave with a different  $\vec{k}$ -vector. We also observe changes in the metachronal wave over time, in this case the  $\vec{k}$ -vector jumps from one reciprocal lattice point to another due to fluctuations. For example in the simulation with a cilia spacing of  $d_c = 3$  the wavelength stabilizes for over  $10\,000\sqrt{ma^2/k_bT}$  on  $\lambda = 27.0(3)a$ , then abruptly changes to  $\lambda = 20.0(2)a$  for the rest of the simulation time ( $20\,000\sqrt{ma^2/k_bT}$ ).

## 4.6 Orientation of the Metachronal Wave

In our simulations the metachronal wave travels never exactly in the effective stroke direction (see Fig. 4.13). We expect the direction of the metachronal wave to be especially sensitive to finite-size effects (see Sec. 4.13 or Sec. 4.5), because the  $\vec{k}$ -vector has to be on the reciprocal lattice of the cilia lattice. Nevertheless we find that in most simulations the wave travels  $10^\circ$  to  $50^\circ$  to the right of the effective stroke direction. This means that the wave is somewhere between symplectic and laeoplectic metachronism.

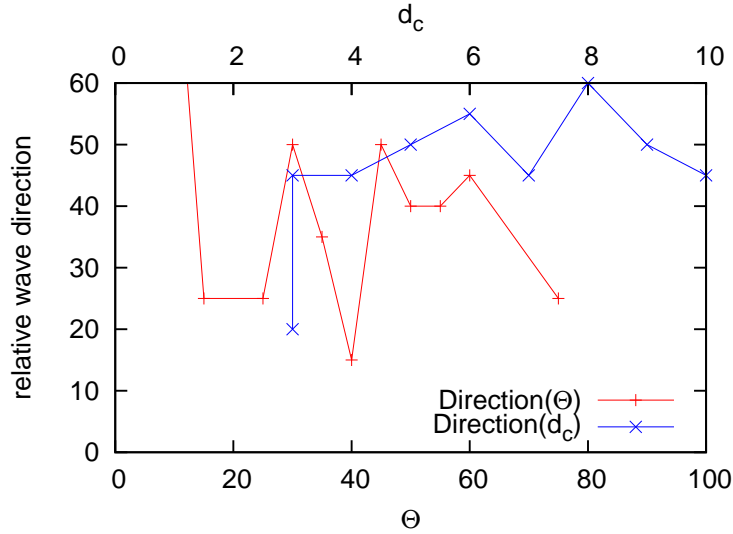


Figure 4.13: Traveling direction of the metachronal wave relative to the effective stroke direction. Data show estimates from time-dependent plots of the direction of the  $\vec{k}$ -vector. Errorbars are hard to estimate, but in the order of  $20^\circ$ . For  $d_c = 3a$  two points are provided because we see two rather stable waves at different simulation times.

A special case is the metachronal wave of the system with  $\Theta = 0$ . It is also oriented about  $35^\circ$  degrees clockwise from the effective stroke direction, but travels in the opposite direction. In other words  $215^\circ$  clockwise from the effective stroke direction.

## 4.7 Correlation Anisotropy

In experiments an anisotropy in the degree of correlation was found. For the experimental measurements in Ref. [22] the correlation function of reflected light intensity was measured in the effective stroke direction and perpendicular to it. Intermediate angles were not studied, but a clear anisotropy could be found. In these experiments correlations are larger in the direction of the effective stroke than perpendicular to it.

In our simulations, the anisotropy can be seen in the exponential term ( $\exp(-\sqrt{\Delta x \mathfrak{K} \Delta x})$ ) of the correlation function. In Fig. 4.14 this can be seen for the reference system. Obviously the correlation function is larger in the effective stroke direction. Due to the explicit fit, a more quantitative assertion can be

made.

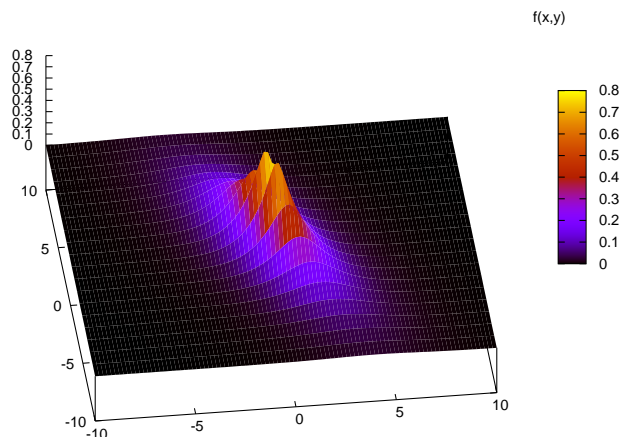


Figure 4.14: Spatial decay of the correlation function ( $\exp(-\sqrt{\Delta x \mathfrak{X} \Delta x})$ ) for the reference system. The effective stroke is from the bottom right to the top left.

As mentioned in Sec. 4.1 diagonalization of  $\mathfrak{X}$  yields the different decay lengths and their directions. Figure 4.15 shows the main correlation direction (direction of the eigenvector with the largest decay length) as a function of the effective stroke direction. As in the experiments of Ref. [22] the main correlation direction is roughly in the effective stroke direction. However, we do see a systematic deviations, caused by lattice effects.

## 4.8 Correlation Lengths

The correlation lengths  $\xi_{1,2}$  generally increase in time in our simulations (see Fig. 4.16). This means that throughout the simulation time we did not reach a stationary state in this parameter. The larger correlation length  $\xi_2$  eventually always increases above system size, which means that a stationary state in the correlation lengths will be dominated by finite-size effects. This leaves a detailed analysis of correlation lengths to simulations of larger systems. No general time dependence of this increase could be identified, because the curve often fluctuates a lot (see Fig. 4.16).

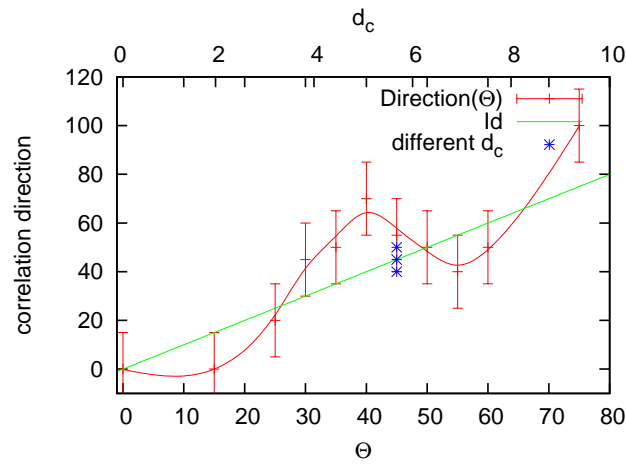


Figure 4.15: Main correlation direction vs effective stroke direction, solid line is a guide to the eye. Blue symbols are for different cilia spacings. The green line is the identity of correlation direction and effective stroke direction  $\Theta$ .

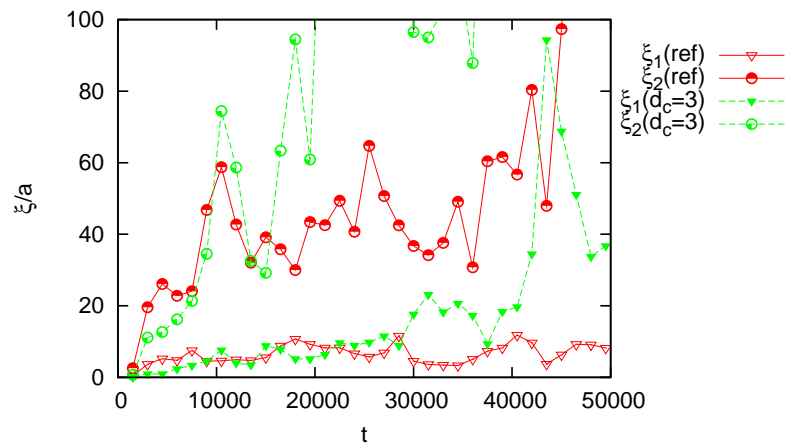


Figure 4.16: Correlation lengths  $\xi_{1/2}$  with  $\xi_1 \leq \xi_2$ , for the reference system (red) and a system with  $d_c = 3$ , as indicated.

## 4.9 Transport

We have explained in Sec 4.3 that the beat period should scale with the solvent viscosity  $\eta$ , because we impose forces on the cilium rather than a cilium shape and beat amplitude. The same argument as in Sec 4.3 leads to an inverse proportionality of the average fluid velocity with the viscosity. In other words

$$|v| = \frac{c_v}{\eta} \quad (4.13)$$

where  $|v|$  is the absolute value of the average fluid velocity and  $c_v$  some proportionality factor. This relation is also found in simulation results for both, cilia with and without metachronal coordination (see Fig. 4.17).

More importantly, metachronal coordination roughly doubles the average fluid velocity (see Fig. 4.18). Because synchronously beating cilia beat faster (see Sec 4.3), they might be expected to also pump the fluid faster. This is not the case. This is a very important result, for it shows that due to the metachronal wave, cilia can move fluid faster. In the remainder of this chapter we will see that this velocity gain prevails for many different parameter sets, ranging up to 3.2.

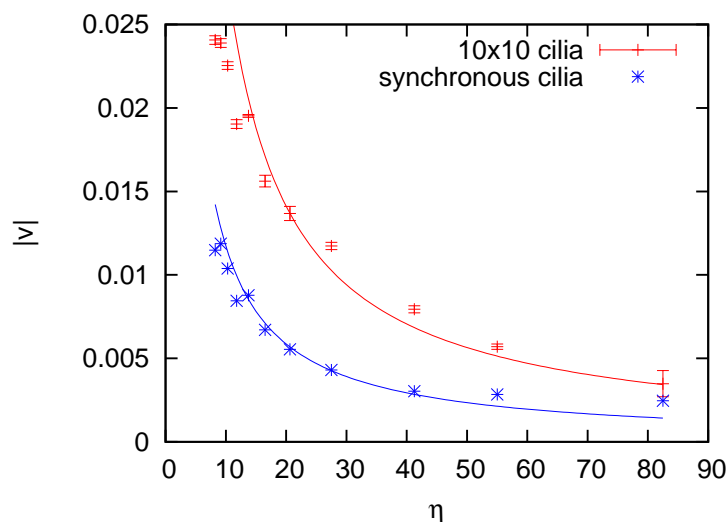


Figure 4.17: Average fluid velocity as function of viscosity  $\eta$ . Solid lines are fits to Eq. (4.13) with  $c_v = 0.28$  (red) and  $c_v = 0.12$  (blue). Systems are reference systems with  $10 \times 10$  cilia, or synchronously beating cilia, as indicated.

By changing the effective stroke direction the average velocity is only changed slightly, almost not at all for the synchronous cilia (see Fig. 4.19).

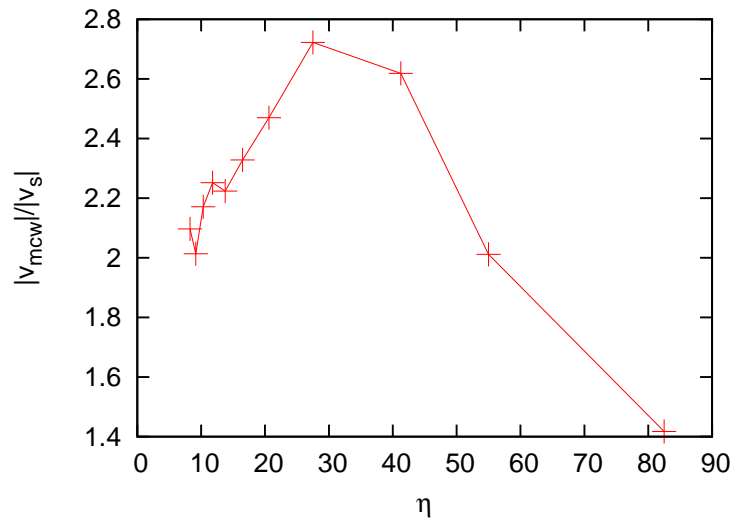


Figure 4.18: Gain in average velocity due to metachronal coordination as function of viscosity  $\eta$ . Velocity measurements have been performed on reference systems with  $10 \times 10$  cilia ( $v_{mcw}$ ) and synchronous beating cilia ( $v_s$ ).

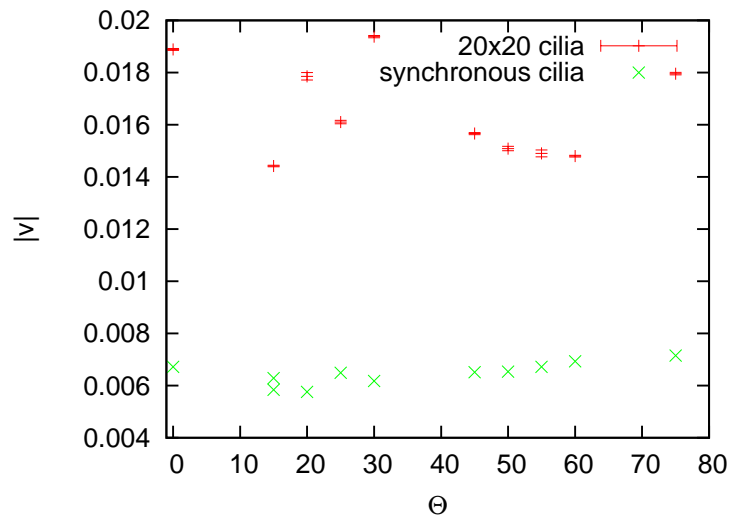


Figure 4.19: Velocity as function of effective stroke direction  $\Theta$  for reference systems with different  $\Theta$  (red) and corresponding synchronously beating cilia (green).

If each cilium has a certain pumping power, the average velocity increases with cilia density, until eventually the fluid moves at the maximum speed of this pump. In this simple picture we would expect a linear increase of the average velocity with cilia density, or

$$|v| \propto \frac{1}{d_c^2}. \quad (4.14)$$

until it saturates at a certain cilia spacing. This dependency could not be found, but a fit to

$$|v| = \frac{c_1}{(d_c)^{c_2}} \quad (4.15)$$

leads to  $c_2 = 1.4$  for  $20 \times 20$  cilia, and  $c_2 = 0.6$  for synchronously beating cilia (see Fig. 4.21).

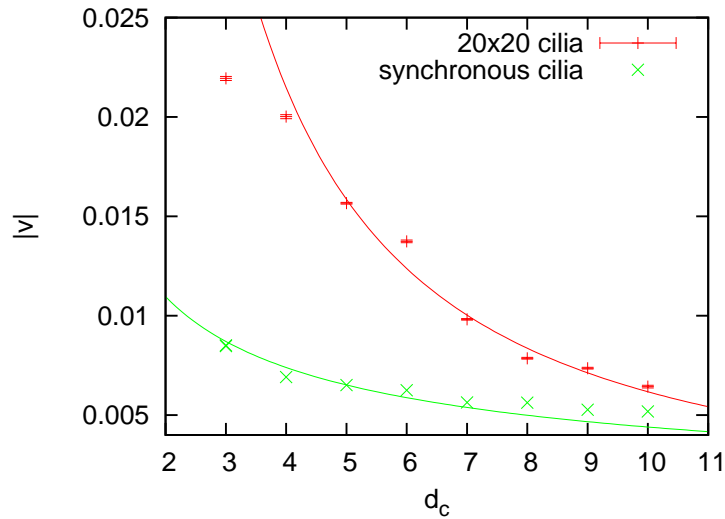


Figure 4.20: Average fluid velocity as function of cilia spacing  $d_c$  for reference systems (red) and corresponding synchronously beating cilia (green). Solid lines are fits to Eq. (4.15) (only to the data of  $d_c \geq 5$  for  $20 \times 20$  cilia).

Interestingly the fluid velocity increase with cilia density is much stronger for metachronal beating cilia than for synchronous beating, such that the velocities are almost identical at a cilia spacing  $d_c = 10a$ .

The reason for the average velocity being faster for metachronal coordinated cilia is clearly an effect correlations. A possible explanation for the transport

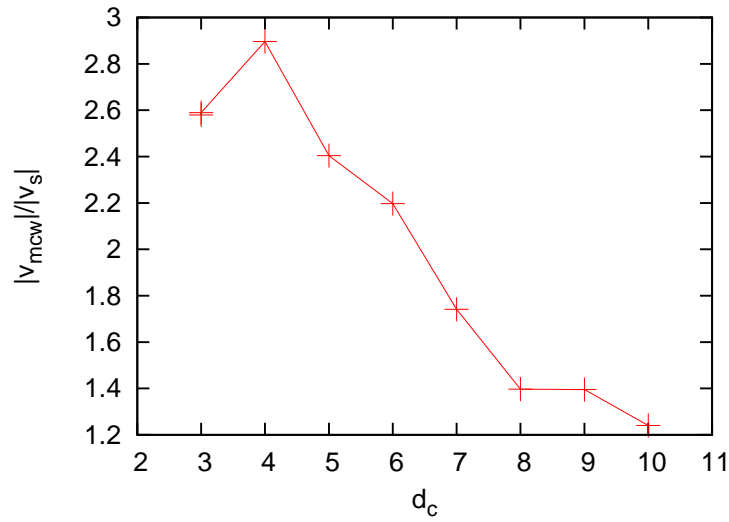


Figure 4.21: Ratio of the average fluid velocities for metachronally coordinated cilia  $|v_{mcw}|$  and synchronously beating cilia  $|v_s|$  as a function of cilia spacing  $d_c$ .

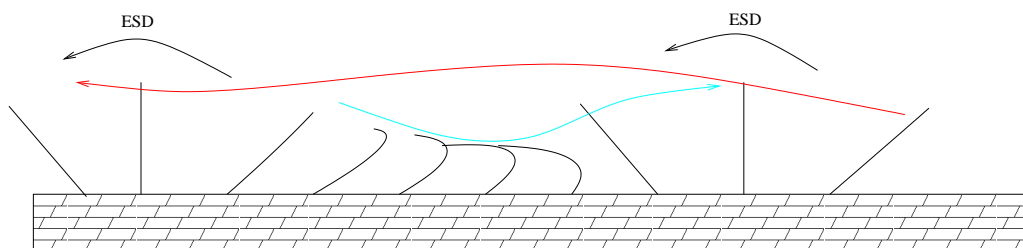


Figure 4.22: Schematic drawing of metachronal beating. Flow from the effective stroke (ESD) is depicted with a red arrow. The flow generated by the recovery stroke is illustrated by a blue arrow. See Text.

enhancement of metachrony is the following. In Fig. 4.23 a schematic two dimensional drawing of metachronal coordinated cilia is given. The flow generated by the cilia in the recovery stroke has to go upwards from the wall. During the effective stroke (ESD) the cilia feel this opposing flow of the neighboring cilia. Although this implies that they move slower, they work at full force against the flow, thus having a large effect on the fluid body

The flow generated by cilia in the effective stroke, also goes upwards away from the wall. This means though that during the recovery stroke the cilia feel a lot less the opposing flow of the neighboring cilia in the power stroke, because the recovery stroke is closer to the wall.

On the other hand, cilia in beating synchronously move, as shown above, a large part of the fluid body with them. Thus a cilium in the effective stroke feels a flow in the effective stroke direction. Although this results in faster movement, it also means it cannot exert the full force onto the fluid. Like a cyclist cycling in too low a gear, peddling is easy and fast, but velocity is small. This explanation is in good agreement with the observed higher beat frequency of the synchronous beating cilia.

## 4.10 Orientation of Transport

The transport direction is close to, but not exactly in the effective stroke direction. A little deviation was expected, because the recovery stroke is tilted to one direction, but the degree of deviation and its dependence on cilia spacing is surprising. Especially for the synchronously beating cilia, the transport direction can deviate strongly from the effective stroke direction.

A linear fit (see Fig. 4.23) shows that the metachronal correlated cilia propel on average the fluid  $1^\circ$  to the right of the effective stroke direction, whereas synchronously beating cilia propel the fluid on average  $11^\circ$  to the left of the effective stroke direction.

In Fig. 4.24 we plot the velocity direction for different cilia spacings. Especially for closely packed cilia the deviation from the effective stroke direction is large. When the cilia are further apart, the velocity direction almost coincides with the effective stroke direction. This indicates that the deviation is a collective phenomenon, and not only due to the out-of-plane motion of the recovery stroke. Still the effective stroke direction clearly dominates the average velocity direction.

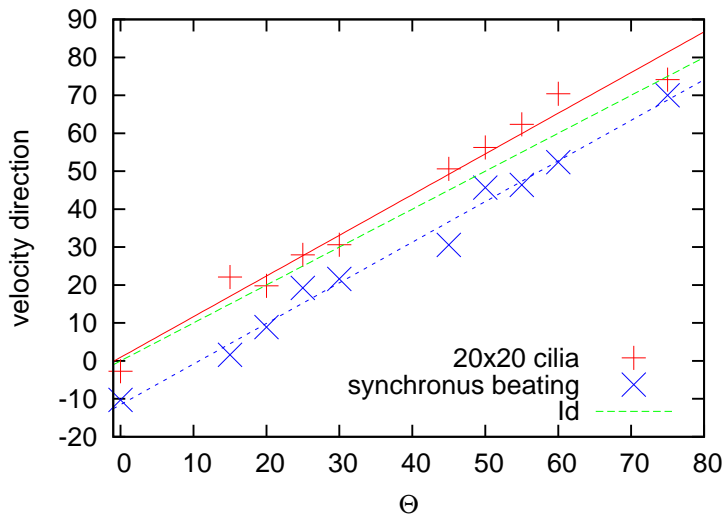


Figure 4.23: Velocity direction as a function of effective stroke direction  $\Theta$ . Otherwise reference system. Lines are linear fits.

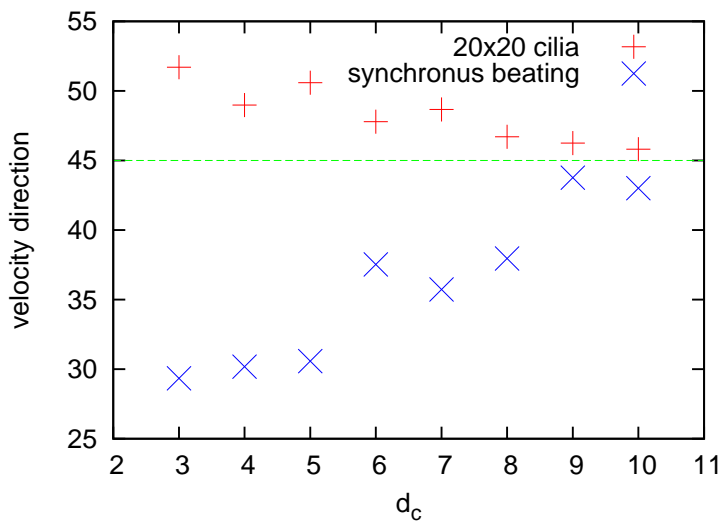


Figure 4.24: Velocity direction as a function of cilia spacing, the green line at  $45^\circ$  is the effective stroke direction.

## 4.11 Energy and Efficiency

In computer simulations the energy input is directly accessible. We calculate the energy input by adding up the energies we put into the system by changing the lengths of the springs. Also the energy output can be determined by recording the energy subtracted from the system during application of the thermostat. Both these energies agree well within the numerical uncertainty of the simulation.

The energy consumption per cilium per beat is relatively constant under changes of the effective stroke direction and cilia spacing (see Fig. 4.25), averages for different systems all being between  $15\,000k_B T/\text{beat}$  and  $15\,200k_B T/\text{beat}$ . This might seem large at first, but is actually surprisingly close to and below estimates of energy expenditure of the order of  $20\,000k_B T/\text{beat}$  [82] or  $200\,000k_B T/\text{beat}$  [31].

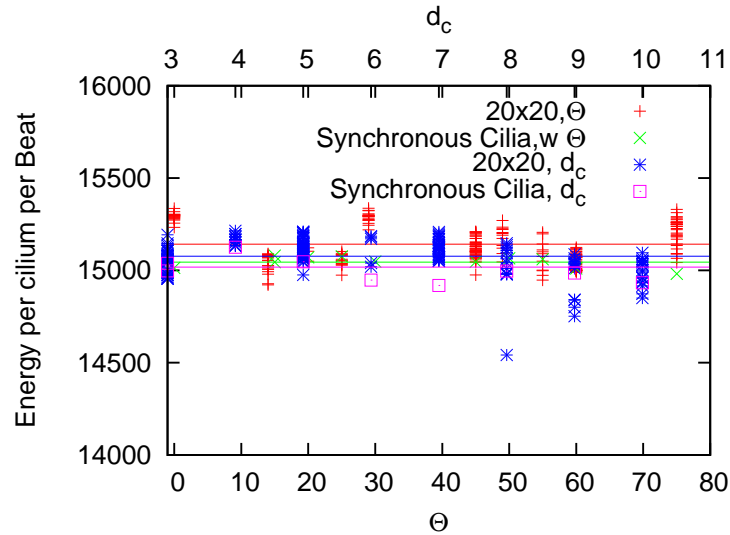


Figure 4.25: Energy consumption per cilium per beat as a function of effective stroke direction  $\Theta$  and cilia spacing  $d_c$  for reference like systems ( $20 \times 20$  and synchronous beating cilia as indicated). Lines are averages.

The increased load on the cilium at higher viscosity increases also the average energy consumption per cilium per beat roughly linearly (see Fig. 4.26). The finite value for  $\eta \rightarrow 0$  arises, as in Sec. 4.3, from internal friction.

The dimensionless efficiency defined in Eq. 2.40 by  $\epsilon = \frac{12\eta v^2 V}{Pd^2}$  is mainly effected by the cilia spacing (see Fig. 4.28) and has a small maximum at a cilia

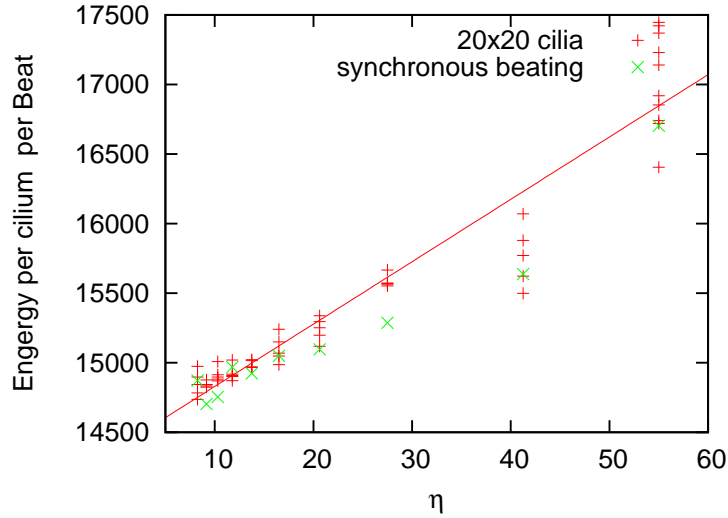


Figure 4.26: Energy consumption per cilium per beat as a function of viscosity  $\eta$ . Line is a linear fit.

spacing of  $4a$  or  $5a$  for metachronally coordinated cilia.

In systems of synchronous beating cilia the fluid swashes back and forth with the cilia beat. This is illustrated in Fig. 4.27, together with the velocity of the reference system relaxing into metachronal coordination. We see how in the reference system the cilia are started synchronously, moving the fluid with high speed in the effective stroke direction. Quickly the system falls into metachronal coordination, and the fluid flows with constant velocity in one direction. On the other hand the synchronous beating cilia constantly move the fluid back and forth at rather high velocities, causing higher shear, and thus more energy dissipation. The efficiency of synchronous beating cilia increases with cilia spacing because the larger fluid body reduces this swashing effect.

The viscosity does not affect the efficiency much up to rather high viscosities, where it decreases. Also the effective stroke direction does not affect the efficiency very much.

We have seen that the cilia in metachronal coordination are much more effective than the synchronous beating cilia. This gain in efficiency is seen best in a plot of the ratio of both efficiencies (see Fig. 4.29). As expected the ratio tends to one as the cilia spacing increases, while a maximum at  $d_c = 3$  of  $\epsilon(\text{metachronal})/\epsilon(\text{synchron})=4$  is found.

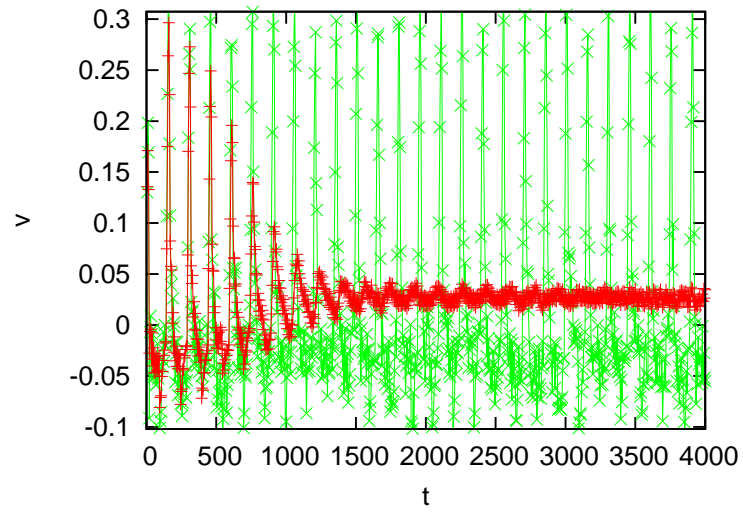


Figure 4.27: Average velocity in the effective stroke direction  $v$  for the reference system (red) and the corresponding systems with synchronous beating (green).

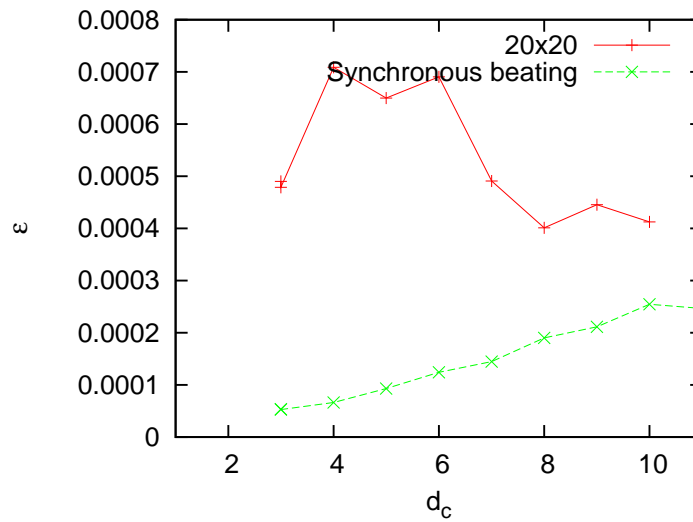


Figure 4.28: Dimensionless efficiency  $\epsilon$  as a function of cilia spacing  $d_c$ , as indicated for systems of  $20 \times 20$  cilia and synchronous beating cilia.

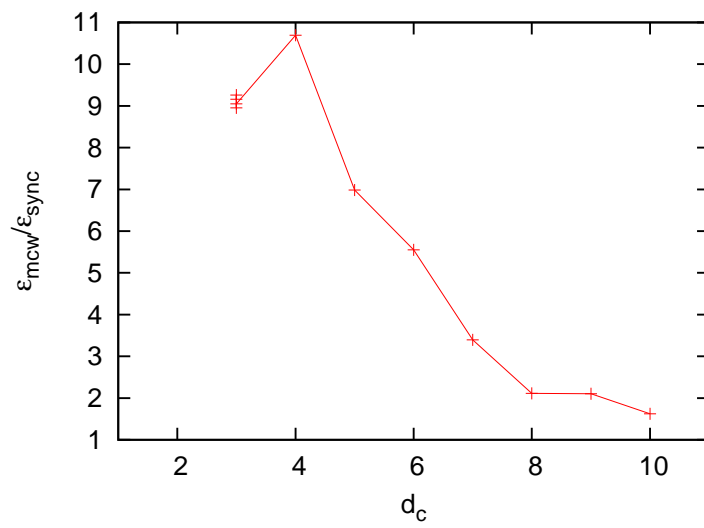


Figure 4.29:  $\epsilon(\text{metachronal})/\epsilon(\text{synchron})$  as a function of cilia spacing  $d_c$ .

## 4.12 Planar Beating

The theoretical work of Jülicher and Vilfan [91] suggests that aplanar beating cilia are more likely to show metachronal coordination than those with a planar beat. Thus we focused our research on aplanar beating cilia (with  $a_{apl} = 0.05$ ). However, it turns out that planar beating cilia  $a_{apl} = 0$  also show metachronal coordination. The main differences between planar and aplanar beating cilia are shown in this section. Planar beating cilia were only studied with cilia spacings  $d_c = 5$ .

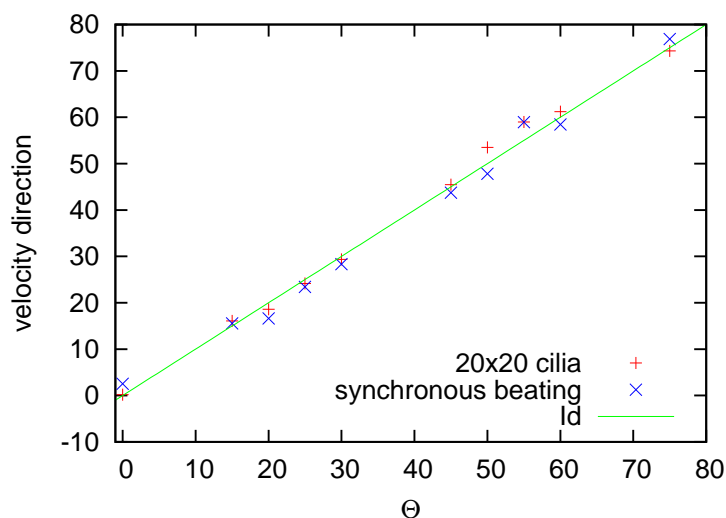


Figure 4.30: Velocity direction as a function of effective stroke direction  $\Theta$  for cilia with aplanarity parameter  $a_{apl} = 0$  (planar beat).

For planar beating cilia, the average velocity direction coincides with the effective stroke direction, both for synchronous beating cilia or cilia in metachronal coordination (see Fig. 4.30). Aplanar beating cilia showed significant deviation in the velocity direction, especially for synchronous beating cilia.

The average fluid velocity for planar beating cilia is slightly higher than for aplanar beating, while the energy consumption per beat is lower. Thus the efficiency of planar beating cilia is roughly 50% higher than for aplanar beating.

## 4.13 Finite-Size Effects

The cilia are arranged on a lattice, thus the metachronal wave is confined to a limited range of  $\vec{k}$  vectors. Typically we simulate arrays of  $20 \times 20$  cilia. Some

larger systems where simulated estimate these effects. Pictures become more clear, but a qualitative change could not be observed in most quantities. Mainly we expect the  $\vec{k}$  vector and the decay lengths of the metachronal wave to be influenced by the system size. As an example we provide a comparison of data obtained from the reference system, and a corresponding system with  $30 \times 30$  and cilia  $60 \times 60$  cilia.

	$20 \times 20$ cilia	$30 \times 30$ cilia	$60 \times 60$ cilia
wavelength $\lambda/a$	21(5)	22(2)	22.5
beat period $\tau_b/\sqrt{ma^2/k_bT}$	181	181	181
fluid velocity $ v /\sqrt{m/k_bT}$	0.0159	0.0167	0.0166
efficiency $\epsilon$	$0.65 \times 10^{-3}$	$0.73 \times 10^{-3}$	$0.71 \times 10^{-3}$

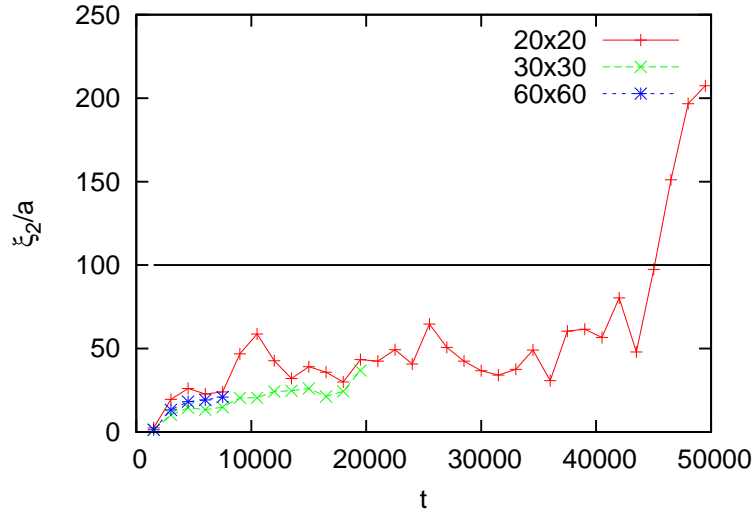


Figure 4.31: Correlation lengths  $\xi_2$  as a function of time for various system sizes, as indicated. The black line marks the size of the  $20 \times 20$  cilia system in box lengths  $a$ .

In most parameters no significant difference could be found. An indication that finite size effects are important is the larger correlation length  $\xi_2$  (see Fig. 4.31). It seems that the correlation length is in the order of  $50a$ . However, the system with  $20 \times 20$  cilia is only  $100a$  wide, which is in the order of  $2\xi_2$  (the width of the correlation function is  $2\xi_2$ ). This leads to a point at which correlations “feel” the finite system size and jump to large values. The larger systems show a similar value for  $\xi_2$ , but the  $60 \times 60$  cilia system has a lateral system size of  $300a$ , significantly larger than the correlation length. Simulations have yet to show if  $\xi_2$  reaches a steady state, but the preliminary results look

promising. The high computational effort of large systems (the data shown for the system of  $60 \times 60$  cilia required 5 000 CPU-hours) has so far prohibited a systematic study of many large systems.

Of course large systems do not affect the fact that the wave vector  $\vec{k}$  has to be commensurate with the cilia grid, so lattice effects are still expected in large systems.

## 4.14 Discussion

The results of our simulations allow the following main conclusions. First of all, we found metachronal coordination of cilia, solely through hydrodynamic interactions. This coordination is strong enough to couple large arrays of cilia, even in the presence of strong thermal fluctuations.

Secondly, our simulations showed that the average transport velocity is highest for cilia in metachronal coordination, up to a factor 3.2 higher than for synchronously beating cilia. The higher average velocity is what is most important for the cell. Typically the efficiency is (although also higher for the cilia in metachronal coordination) not so crucial because the cell uses only a small fraction of its available energy for propulsion [71]. Intuitively it is not obvious why metachronal coordinated cilia should create a higher fluid velocity, especially because the synchronously beating cilia beat faster, but a reasonable explanation is provided in which the decrease in beat frequency actually follows. We demonstrated that the pumping velocity and the gain through metachronal coordination grow with cilia density. We conclude that the enhancement of the average velocity essentially depends on the hydrodynamic interactions between the cilia.

Furthermore, our simulations revealed that the efficiency of cilia pumping is increased up to an order of magnitude through metachronal coordination. The cause of this efficiency increase was identified as the swashing of the fluid if the cilia beat synchronously. This swashing leads to higher velocity gradients, and thus to more energy dissipation through the fluid viscosity.



## 5 Conclusion and Outlook

We have constructed a minimalistic model axoneme that is used to study the behaviour of sperm and cilia by computer simulations. The axoneme is modeled as a semi-flexible polymer, where an active bending force can be imposed. Beat patterns are implemented to mimic the biological systems.

Hydrodynamic interactions are taken into account for by a powerful, particle-based, mesoscopic simulation technique called multi-particle collision dynamics. This method is very well suited to investigate hydrodynamics in systems with embedded mesoscopic objects in complex flow geometries. We successfully apply multi-particle collision dynamics to active biological systems for the first time.

We have demonstrated that this sperm model captures important features of sperm motion. In particular, we have unveiled how hydrodynamic interactions lead to an adhesion of sperm cells to a wall, and are able to explain this effective attraction by a combination of thrust and hydrodynamic repulsion of the tail from the wall. Furthermore, we find that the chirality of the sperm is the cause of the oriented circular motion at interfaces. Tuning this chirality, we find two regimes of motion. In the strongly bent regime, the sperm swims very close to the wall in tight circles, with a diameter smaller than the sperm length. The beating plane remains perpendicular to the wall. In the weakly bent regime, the sperm rotates around its longitudinal axis and follows large circles, up to an order of magnitude larger than in the strongly bent regime. Even though the sperm rotates around its longitudinal axis, the beating plane is most of the time parallel to the wall. The circular motion is caused by the head of the sperm touching the surface, creating a torque on the sperm. When the bending is strong enough, the head gets stuck at the wall, stopping further rotations. A transition is also observed for freely swimming sperm. In this case the strongly bent sperm swim in pronounced helices, whereas in the weakly bent regime the sperm swim almost in a straight line. We explain the transition between these two regimes of motion by a dynamic shape change of the sperm model.

In the cilia simulations, we present for the first time a two-dimensional array of

autonomously beating cilia, solely coupled by hydrodynamic interactions, that develop a metachronal wave. Many different wave and transport parameters are studied. Most importantly it is found that the transport velocity increases up to a factor 3.2 through metachronal coordination compared to synchronously beating cilia. A consistent explanation for the increased transport velocity is found in the interactions of neighboring cilia. In metachronal coordination the cilium can exert its full force onto the fluid, while in synchronous beating it moves mostly with the local fluid. Both, the transport velocity and the gain through metachronal coordination, are larger the closer the cilia are packed. As the transport velocity grows, and the energy consumption per time decreases through metachronal coordination, we also show that the efficiency increases up to an order of magnitude by metachronal coordination. The high power consumption of the synchronously beating cilia arises due to back and forth swashing of the fluid during the beat. This leads to higher energy dissipation compared to the relatively steady flow generated by metachronally beating cilia. Furthermore we characterize transport and wave properties as a function of the viscosity, effective stroke direction and cilia spacing. For example, we show that the main correlation direction roughly coincides with the effective stroke direction, that the beat frequency decreases through metachronal coordination while the energy consumption per beat is basically independent of cilia spacing, effective stroke direction and metachronal coordination.

So far our model sperm uses a sinusoidal bending wave as its beat pattern. Although this resembles the observed beat shape in experiments, it suppresses any feedback of the hydrodynamics on the beat pattern. In the future we intend to implement a more realistic axoneme model as presented in the literature [36].

Chemotaxis of sperm is an important question in current biology. Detailed data is available today how the sperm trajectory changes in chemotaxis [85], due to a gradient of a chemical attractant. But how a sperm performs the necessary tight turns and straight paths has yet to be investigated in detail. By tuning the bending parameter, our model sperm is able to change direction in response to external stimuli. We will elaborate on the connection between chemical signal, sperm shape change and the resulting movement.

The system sizes studied so far in simulations are too small to capture the decay of the correlations between the cilia. We want to examine larger systems in the future and identify correlation lengths and their dependency on viscosity, cilia arrangement and beat parameters.

---

Finally, it was suggested that the aplanarity of the ciliary beat strongly influences the metachronal wave pattern [1]. Within the present model, different beat patterns can be implemented. We want to study their effect on the metachronal wave and transport.



## 6 Acknowledgments

First and foremost, I thank Prof. Dr. Gerhard Gompper for introducing me to this interesting field of research. I highly appreciate the time and help I got from him throughout the last three years. Within his whole group, I enjoyed a great and friendly working atmosphere. Patiently they listened to my questions regarding important, and not so important, aspects of my research. Special thanks go to “Brokoli” Sebastian Messlinger for bearing me as an office mate, it was a great time. Marisol Ripoll and Gerrit Vliegthart not only for proofreading, but also for scientific discussions and help during my time in Jülich. Without the administrative help of Helga Paffen, I would have been lost in several occasions.

Gratefully I acknowledge Prof. Dr. Benjamin Kaupp for discussions regarding the biological aspects of this work. It is from him, and members of his group, namely Dr. Martin Böhmer and Dr. Ingo Weyand, that I learned a lot about the fascinating biology of sperm.

Furthermore a running computer system is obviously essential for simulations. Good work here typically remains unnoticed. Thanks for the high uptime and the help on computer operation related questions to the network and numerics team of the IFF and ZAM.

Last but not least, I would like to thank my friends and family. Thanks to the gamers and the cooking crew, I quickly felt at home in Cologne. Denise, I thank you for being who you are, in every aspect. And finally, I want to express my gratitude towards my parents for their love and support over the years on my way to become a scientist.



# 7 Appendix

## 7.1 Parallelization

Due to the large systems required a large computational power is necessary, this is achieved by parallelization. The code is parallelized using OpenMP, a shared memory Application Program Interface (API) for C++ (and others). Compared to MPI, OpenMP is less powerful but more easy to implement. Its most important feature is the automatic loop parallelization. Its main drawback is its restriction to shared memory parallelization, thus limiting the number of processors to be used.

MPCD is very well suited for a shared memory parallelization because many steps in the algorithm can be calculated independently on different processors if the system state is available for reading for all processors.

In general a good OpenMP code can run both on a parallel and a serial machine. Parallelization is achieved by distributing different iterations of a loop on different processors, while the system state is stored in shared memory. Here an example:

```
#pragma omp parallel for
for (i=0..1000){
    do_something(i)
}
```

If the program reaches this point it will fork of in different threads, each doing `do_something(i)` for different `i`. Of course this can only work if `do_something(i)` is independent of `do_something(j)`. Otherwise, for example, so called race conditions can happen. The result of the simulation depends on which processor “wins the race” to first do `do_something(i)`. An example:

```
#pragma omp parallel for
for (i=1..1000){
```

```
    n[i]=n[i-1]+1;
}
```

Obviously here the `do_something(i)` is not independent of the other steps. If `n[0]=0`, `n[i]` should be `i`. But most likely one processor or the other will compute some `n[i]` before `n[i-1]` is computed. Thus starting at zero again. In the end `n[i]` could have the entries

```
0 1 2 3 4 5 0 1 2 3 ...
```

or similar.

A more subtle mistake is shown in the next example which computes  $\sum_{i=1}^{100} i$ :

```
#pragma omp parallel for
for (i=1..100){
    a=a+i;
}
```

Because the sum is commutative, the result does not depend on the order of execution. However it can happen that one processor writes to variable `a` while another is trying the same. This also causes run-dependent results.

Luckily most of the steps in MPCD are independent. The main, non independent step is connected to calculating the average box velocity, where a similar problem to the last example exists. OpenMP provides so called locks, to lock a variable while writing to it, thus circumventing the problem. In principal all of these problems can be solved, but always at the cost of so called “parallel overhead” i.e. extra commands not needed for serial computation.

The molecular dynamics part of the code is more difficult to parallelize efficiently for two reasons:

First there are fewer particles, and therefore each processors gets smaller chunks of work, before it has to wait for the other processors to finish.

Second the force calculation is by definition strongly depending on other particles. Therefore dependencies grow.

The speedup  $S$  of a parallel program can be determined by dividing the time the job takes on one processor  $t(1)$  by the time  $x$  processors need  $t(x)$

$$S(x) = \frac{t(1)}{t(x)} \quad (7.1)$$

in a first approximation the run time consists of a serial ( $s$ ) and a parallel ( $p$ ) time. Only the latter decreases with the number of processors. Thus

$$t(x) = s + \frac{p}{x} \quad (7.2)$$

which leads to

$$S(x) = \frac{s + p}{s + p/x} = \frac{1}{1 - f + f/x} < x \quad (7.3)$$

where  $f$  is the parallel fraction of the code. This is known as Amdahls Law. With it the “quality of parallelization” can be measured by the parallel fraction  $f$ . For our code  $f$  depends on the system. Larger systems perform better because the chunks going to each processor are larger. Also the sperm simulations perform better than the cilia, because the ratio MPCD particles/monomers is larger.

Generally  $f$  ranges from 95% to 99% in our simulations. As an example a speedup plot for cilia is given in figure 7.1. These data come from the simulation times of systems equivalent to the reference system ( only with different effective stroke directions). The fit of Amdahls Law leads to a parallel fraction of 98%. As mentioned before the speedup strongly depends on the system. Larger systems and sperm perform better, smaller systems worse.

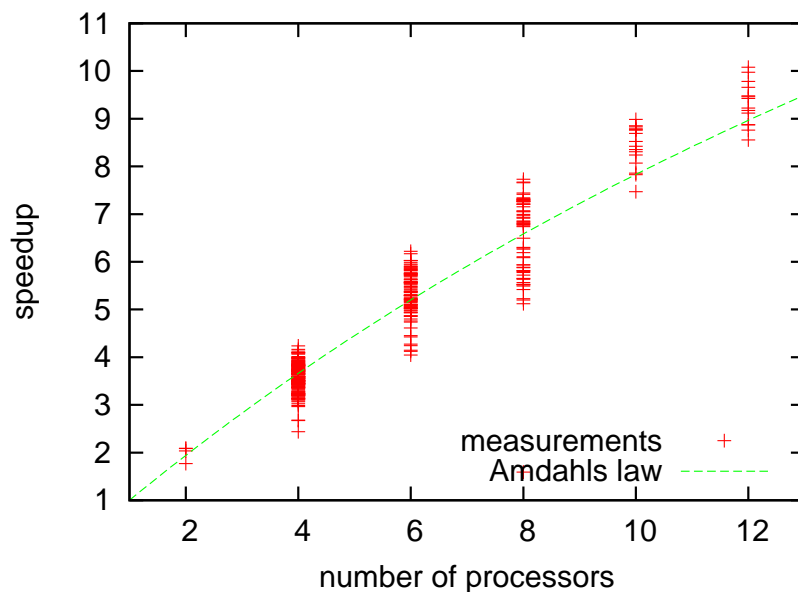


Figure 7.1: parallel performance of the reference system of cilia



# Bibliography

- [1] E. Aiello and M. A. Sleight. Metachronal wave of lateral cilia of *mytilus-edulis*. *J. Cell Biol.*, **54**:493, 1972.
- [2] B. Alberts, D. Bray, A. Johnson, J. Lewis, M. Raff, K. Roberts, and P. Walter. *Essential Cell Biology*. Garland Publishing, Inc., 1998.
- [3] I. Ali, D. Marenduzzo, and J. M. Yeomans. Polymer packaging and ejection in viral capsids: Shape matters. *Phys. Rev. Lett.*, **96**:208102, 2006.
- [4] M. P. Allen and D. J. Tildesley. *Computer simulation of liquids*. Oxford : Clarendon Press, 1989.
- [5] M. S. Bretscher. The molecules of the cell membrane. *Scientific American*, **253**:100, 1985.
- [6] C. J. Brokaw. *Cilia and Flagella*, chapter 5: Movement of the flagellum of some marine invertebrate spermatozoa, page 93 to 108. Academic Press, 1974.
- [7] C. J. Brokaw. Calcium-induced asymmetrical beating of triton-demembrated sea-urchin sperm flagella. *J. Cell Biol.*, **82**:401–411, 1979.
- [8] C. J. Brokaw. The sea-urchin spermatozoon. *Bioessays*, **12**:449–452, 1990.
- [9] C. J. Brokaw. Computer simulation of flagellar movement: VII. conventional but functionally different cross-bridge models for inner and outer arm dyneins can explain the effects of outer arm dynein removal. *Cell Motil. Cytoskeleton*, **42**:134–148, 1999.
- [10] C. J. Brokaw. Computer simulation of flagellar movement VIII: Coordination of dynein by local curvature control can generate helical bending waves. *Cell Motil. Cytoskeleton*, **53**:103–124, 2002.

- [11] C. J. Brokaw. Computer simulation of flagellar movement IX. Oscillation and symmetry breaking in a model for short flagella and nodal cilia. *Cell Motil. Cytoskeleton*, **60**:35–47, 2005.
- [12] J. Cosson, P. Huitorel, and C. Gagnon. How spermatozoa come to be confined to surfaces. *Cell Motil. Cytoskeleton*, **54**:56–63, 2003.
- [13] E. N. Cytrynbaum, J. M. Scholey, and A. Mogilner. A force balance model of early spindle pole separation in Drosophila embryos. *Biophys. J.*, **84**:757–769, 2003.
- [14] A. Czirok, A. L. Barabasi, and T. Vicsek. Collective motion of self-propelled particles: Kinetic phase transition in one dimension. *Phys. Rev. Lett.*, **82**:209–212, 1999.
- [15] J. K. G. Dhont. *Computational Condensed Matter Physics, Lecture notes of the 37th IFF spring school*, chapter B1 Statistical Mechanics. Forschungszentrum Jülich, 2006.
- [16] R. H. Dillon, L. J. Fauci, and C. Omoto. Mathematical modeling of axoneme mechanics and fluid dynamics in ciliary and sperm motility. *Dynam. Cont. Dis. Ser. A*, **10**:745–757, 2003.
- [17] M. R. D’Orsogna, Y. L. Chuang, A. L. Bertozzi, and L. S. Chayes. Self-propelled particles with soft-core interactions: Patterns, stability, and collapse. *Phys. Rev. Lett.*, **96**:104302, 2006.
- [18] R. Dreyfus, J. Baudry, M. L. Roper, M. Fermigier, H. A. Stone, and J. Biette. Microscopic artificial swimmers. *Nature*, **437**:862–865, 2005.
- [19] P. Espanol and P. Warren. Statistical-mechanics of dissipative particle dynamics. *Europhys. Lett.*, **30**:191–196, 1995.
- [20] L. J. Fauci and A. McDonald. Sperm motility in the presence of boundaries. *B. Math. Biol.*, **57**:679–699, 1995.
- [21] J. T. Finer, R. M. Simmons, and J. A. Spudich. Single myosin molecule mechanics - piconewton forces and nanometer steps. *Nature*, **368**:113–119, 1994.

- [22] L. Gheber and A. Korngreen and Z. Priel. Effect of viscosity on metachrony in mucus propelling cilia. *Cell Motil. Cytoskeleton*, **39**:9, 1998.
- [23] L. Gheber and Z. Priel. Metachronal activity of cultured mucociliary epithelium under normal and stimulated conditions. *Cell Motil. Cytoskeleton*, **28**:333–345, 1994.
- [24] L. Gheber and Z. Priel. Extraction of cilium beat parameters by the combined application of photoelectric measurements and computer simulation. *Biophys. J.*, **72**:449–462, 1997.
- [25] R. Golestanian, T. B. Liverpool, and A. Ajdari. Propulsion of a molecular machine by asymmetric distribution of reaction products. *Phys. Rev. Lett.*, **94**:220801, 2005.
- [26] J. Gray. The movement of sea-urchin spermatozoa. *J. Exp. Biol.*, **32**:775–800, 1955.
- [27] J. Gray and G. J. Hancock. The propulsion of sea-urchin spermatozoa. *J. Exp. Biol.*, **32**:802–814, 1955.
- [28] S. W. Grill, K. Kruse, and F. Jülicher. Theory of mitotic spindle oscillations. *Phys. Rev. Lett.*, **94**:108104, 2005.
- [29] R. D. Groot and P. B. Warren. Dissipative particle dynamics: Bridging the gap between atomistic and mesoscopic simulation. *J. Chem. Phys.*, **107**:4423–4435, 1997.
- [30] S. Gueron and K. Levit-Gurevich. Computation of the internal forces in cilia: Application to ciliary motion, the effects of viscosity, and cilia interactions. *Biophys. J.*, **74**:1658–1676, 1998.
- [31] S. Gueron and K. Levit-Gurevich. Energetic considerations of ciliary beating and the advantage of metachronal coordination. *P. Natl. Acad. Sci. USA*, **96**:12240–12245, 1999.
- [32] S. Gueron and K. Levit-Gurevich. A three-dimensional model for ciliary motion based on the internal 9+2 structure. *P. Phys. Soc. Lond. B*, **268**:599–607, 2001.

- [33] S. Gueron and K. Levit-Gurevich. The three-dimensional motion of slender filaments. *Math. Method Appl. Sci.*, **24**:1577–1603, 2001.
- [34] S. Gueron and N. Liron. Ciliary motion modeling, and dynamic multicilia interactions. *Biophys. J.*, **63**:1045–1058, 1992.
- [35] E. Hildebrand and U. B. Kaupp. Sperm chemotaxis a primer. *Ann. NY. Acad. Sci.*, **1061**:221–225, 2005.
- [36] A. Hilfinger. *Dynamics of Cilia and Flagella*. PhD thesis, Max-Planck-Institut für Physik komplexer Systeme, 2005.
- [37] P. J. Hoogerbrugge and J. M. V. A. Koelman. Simulating microscopic hydrodynamic phenomena with dissipative particle dynamics. *Europhys. Lett.*, **19**:155–160, 1992.
- [38] W. Humphrey, A. Dalke, and K. Schulten. VMD – Visual Molecular Dynamics. *Journal of Molecular Graphics*, **14**:33–38, 1996.
- [39] T. Ihle and D. M. Kroll. Stochastic rotation dynamics: A Galilean-invariant mesoscopic model for fluid flow. *Phys. Rev. E*, **63**:020201, 2001.
- [40] T. Ihle and D. M. Kroll. Stochastic rotation dynamics. I. Formalism, Galilean invariance, and Green-Kubo relations. *Phys. Rev. E*, **67**:066705, 2003.
- [41] T. Ihle and D. M. Kroll. Stochastic rotation dynamics II: Transport coefficients, numerics, long time tails. *Phys. Rev. E*, **67**:066706, 2003.
- [42] K. Inaba. Molecular architecture of the sperm flagella: Molecules for motility and signaling. *Zoological Science*, **20**:1043–1056, 2003.
- [43] Y. Inoue, Y. Chen, and H. Ohashi. A mesoscopic simulation model for immiscible multiphase fluids. *J. Comp. Phys.*, **201**:191–203, 2004.
- [44] F. Jülicher and J. Prost. Spontaneous oscillations of collective molecular motors. *Phys. Rev. Lett.*, **78**:4510–4513, 1997.
- [45] U. B. Kaupp, E. Hildebrand, and I. Weyand. Sperm chemotaxis in marine invertebrates - molecules and mechanisms. *J. Cell. Physiol.*, **208**:487–494, 2006.

- [46] U. B. Kaupp, J. Solzin, E. Hildebrand, J. E. Brown, A. Helbig, V. Hagen, M. Beyermann, F. Pampaloni, and I. Weyand. The signal flow and motor response controlling chemotaxis of sea urchin sperm. *Nature Cell Biol.*, **5**:109–117, 2003.
- [47] N. Kikuchi, C. M. Pooley, J. F. Ryder, and J. M. Yeomans. Transport coefficients of a mesoscopic fluid dynamics model. *J. Chem. Phys.*, **119**:6388–6395, 2003.
- [48] M. Kim, J. C. Bird, A. J. Van Parys, K. S. Breuer, and T. R. Powers. A macroscopic scale model of bacterial flagellar bundling. *P. Natl. Acad. Sci. USA*, **100**:15481–15485, 2003.
- [49] Y. W. Kim and R. R. Netz. Pumping fluids with periodically beating grafted elastic filaments. *Phys. Rev. Lett.*, **96**:158101, 2006.
- [50] S. Kobayashi, O. Takizawa, and H. Morikawa. Simulation study of elastic micropropulsion mechanism modeled on bending mechanism of eukaryotic flagella in liquid. *JSME Int. J. C-Dyn. Con.*, **43**:845–852, 2000.
- [51] M. C. Lagomarsino, P. Jona, and B. Bassetti. Metachronal waves for deterministic switching two-state oscillators with hydrodynamic interaction. *Phys. Rev. E*, **68**:021908, 2003.
- [52] P. Lallemand and L. S. Luo. Theory of the lattice Boltzmann method: Dispersion, dissipation, isotropy, Galilean invariance, and stability. *Phys. Rev. E*, **61**:6546–6562, 2000.
- [53] A. Lamura, G. Gompper, T. Ihle, and D. M. Kroll. Multi-particle collision dynamics: Flow around a circular and a square cylinder. *Europhys. Lett.*, **56**:319–325, 2001.
- [54] L. Landau and E. Lifschitz. *Fluid mechanics*. Oxford : Pergamon Press, 1987.
- [55] E. Lauga, W. R. DiLuzio, G. M. Whitesides, and H. A. Stone. Swimming in circles: Motion of bacteria near solid boundaries. *Biophys. J.*, **90**:400–412, 2006.
- [56] C. B. Lindemann. A geometric clutch hypothesis to explain oscillations of the axoneme of cilia and flagella. *J. Theor. Biol.*, **168**:175–189, 1994.

- [57] C. B. Lindemann. Testing the geometric clutch hypothesis. *Biol. Cell*, **96**:681–690, 2004.
- [58] C.B. Lindemann. Geometric clutch model version 3: The role of the inner and outer arm dyneins in the ciliary beat. *Cell Motil. Cytoskeleton*, **52**:242, 2002.
- [59] H. Löwen. Anisotropic self-diffusion in colloidal nematic phases. *Phys. Rev. E*, **59**:1989–1995, 1999.
- [60] A. Malevanets and R. Kapral. Mesoscopic model for solvent dynamics. *J. Chem. Phys.*, **110**:8605–8613, 1999.
- [61] A. Malevanets and J. M. Yeomans. Dynamics of short polymer chains in solution. *Europhys. Lett.*, **52**:231–237, 2000.
- [62] M. Manghi, X. Schlagberger, and R. R. Netz. Propulsion with a rotating elastic nanorod. *Phys. Rev. Lett.*, **96**:068101, 2006.
- [63] G. R. McNamara and G. Zanetti. Use of the Boltzmann-equation to simulate lattice-gas automata. *Phys. Rev. Lett.*, **61**:2332–2335, 1988.
- [64] G. Nägele. *Computational Condensed Matter Physics, Lecture notes of the 37th IFF spring school*, chapter B4 Brownian Dynamics Simulations, page B4. Forschungszentrum Jülich, 2006.
- [65] H. Noguchi and G. Gompper. Fluid vesicles with viscous membranes in shear flow. *Phys. Rev. Lett.*, **93**:258102, 2004.
- [66] H. Noguchi and G. Gompper. Shape transitions of fluid vesicles and red blood cells in capillary flows. *P. Natl. Acad. Sci. USA.*, **102**:14159, 2005
- [67] J. T. Padding and A. A. Louis. Hydrodynamic and brownian fluctuations in sedimenting suspensions. *Phys. Rev. Lett.*, **93**:220601, 2004.
- [68] C. S. Peskin. Numerical analysis of blood flow in heart. *J. Comp. Phys.*, **25**:220–252, 1977.
- [69] C. S. Peskin. The immersed boundary method. *Acta Numerica*, **11**:479–517, 2002.

- [70] T. R. Powers. Role of body rotation in bacterial flagellar bundling. *Phys. Rev. E*, **65**:040903, 2002.
- [71] E. M. Purcell. Life at low Reynolds-number. *Am. J. Phys.*, **45**:3–11, 1977.
- [72] S. M. Rafelski and J. A. Theriot. Crawling toward a unified model of cell motility: Spatial and temporal regulation of actin dynamics. *Annu. Rev. Biochem.*, **73**:209–239, 2004.
- [73] P. Reimann. Brownian motors: noisy transport far from equilibrium. *Phys. Rep.*, **361**:57–265, 2002.
- [74] M. Ripoll. *Computational Condensed Matter Physics, Lecture notes of the 37th IFF spring school*, chapter B5 Mesoscale hydrodynamics simulations, page B5. Forschungszentrum Jülich, 2006.
- [75] M. Ripoll, K. Mussawisade, R. G. Winkler, and G. Gompper. Low-Reynolds-number hydrodynamics of complex fluids by multi-particle collision dynamics. *Europhys. Lett.*, **68**:106–112, 2004.
- [76] M. Ripoll, K. Mussawisade, R. G. Winkler, and G. Gompper. Dynamic regimes of fluids simulated by multiparticle-collision dynamics. *Phys. Rev. E*, **72**:016701, 2005.
- [77] M. Ripoll, R. G. Winkler, and G. Gompper. Star polymers in shear flow. *Phys. Rev. Lett.*, **96**:188302, 2006.
- [78] L. Rothschild. Sea-urchin spermatozoa. *Biol. Rev.*, **26**:1, 1951.
- [79] L. Rothschild. Non-random distribution of bull spermatozoa in a drop of sperm suspension. *Nature*, **198**:1221, 1963.
- [80] W. S. Ryu, R. M. Berry, and H. C. Berg. Torque-generating units of the flagellar motor of escherichia coli have a high duty ratio. *Nature*, **403**:444–447, 2000.
- [81] T. Sakai, Y. Chen, and H. Ohashi. Real-coded lattice gas model for ternary amphiphilic fluids. *Phys. Rev. E*, **65**:031503, 2002.
- [82] M.A. Sleight. *The Biology of Cilia and Flagella*, chapter 2: The Structure of Cilia, pages 11–75. Pergamon Press, Oxford, 1962.

- [83] M.A. Sleight. *Cilia and Flagella*, chapter 4: Patterns of movement of cilia and flagella, page 79 to 92. Academic Press, 1974.
- [84] Y. Sowa, A. D. Rowe, M. C. Leake, T. Yakushi, M. Homma, A. Ishijima, and R. M. Berry. Direct observation of steps in rotation of the bacterial flagellar motor. *Nature*, **437**:916–919, 2005.
- [85] T. Strunker, I. Weyand, W. Bonigk, Q. Van, A. Loogen, J. E. Brown, N. Kashikar, V. Hagen, E. Krause, and U. B. Kaupp. A K<sup>+</sup>-selective cGMP-gated ion channel controls chemosensation of sperm. *Nature Cell Biol.*, **8**:1149, 2006.
- [86] S. L. Tamm and G. A. Horridge. Relation between orientation of central fibrils and direction of beat in cilia of opalina. *P. Phys. Soc. Lond. B*, **175**:219, 1970.
- [87] M. M. Tirado, C. L. Martinez, and J. G. Delatorre. Comparison of theories for the translational and rotational diffusion-coefficients of rod-like macromolecules - application to short DNA fragments. *J. Chem. Phys.*, **81**:2047–2052, 1984.
- [88] K. Tucci and R. Kapral. Mesoscopic multi-particle collision dynamics of reaction-diffusion fronts. *J. Phys. Chem. B*, **109**:21300–21304, 2005.
- [89] E. Tüzel, T. Ihle, and D. M. Kroll. Constructing thermodynamically consistent models with a non-ideal equation of state. *Mathematics and Computers in Simulation*, **72**:232–236, 2006.
- [90] E. Tüzel, M Strauss, T. Ihle, and D. M. Kroll. Transport coefficients for stochastic rotation dynamics in three dimensions. *Phys. Rev. E*, **68**:036701, 2003.
- [91] A. Vilfan and F. Jülicher. Hydrodynamic flow patterns and synchronization of beating cilia. *Phys. Rev. Lett.*, **96**:058102, 2006.
- [92] R. G. Winkler, K. Mussawisade, M. Ripoll, and G. Gompper. Rod-like colloids and polymers in shear flow: A multi-particle collision dynamics study. *J. Phys.: Condens. Matter*, **16**:S3941–S3954, 2004.

- [93] R. G. Winkler, M. Ripoll, K. Mussawisade, and G. Gompper. Simulation of complex fluids by multi-particle-collision dynamics. *Comput. Phys. Commun.*, **169**:326–330, 2005.
- [94] D. M. Woolley. Motility of spermatozoa at surfaces. *Reprod.*, **126**:259–270, 2003.



# Kurzzusammenfassung

Spermien schwimmen durch Flüssigkeiten mithilfe einer aktiven schlangenförmigen Bewegung ihres Schwanzes, dem Flagellum. Experimentell hat sich herausgestellt, dass sich Spermien stets an Oberflächen ansammeln. An der Oberfläche schwimmen sie dann in einer kreisförmigen Bewegung, deren Ausrichtung von der Spezies abhängt.

Zilien sind haarähnliche Zellfortsätze, die mit einer peitschenförmigen Bewegung Flüssigkeit, oder die Zelle, bewegen. Zilien finden sich in den verschiedensten Organismen. Zum Beispiel benutzt das Pantoffeltierchen Zilien zur Fortbewegung, während in der menschlichen Lunge Zilien Schleim und Fremdkörper heraus transportieren. Das spannendste Phänomen, welches man bei Zilien beobachten kann, ist wohl die “Metachronal Wave”. Wenn viele Zilien gemeinsam schlagen, bildet sich spontan ein Wellenmuster aus, ganz ähnlich dem eines Weizenfeldes im Wind. Zilien und Flagellen haben eine gemeinsame Struktur, das Axonem.

Wir simulieren ein Modellaxonem aus drei semiflexiblen Polymerstäben die zu einer kranähnlichen Struktur zusammengefasst sind. Mithilfe einer mesoskopischen Simulationsmethode, genannt Multi-Particle Collision Dynamics (MPCD), werden hydrodynamische Wechselwirkungen berücksichtigt. Im Zuge dieser Arbeit wird MPCD zum ersten Mal erfolgreich auf aktive biologische Systeme angewandt.

In Simulationen von Spermien wird die Axonemstruktur chiral um einen Kopf ergänzt. Es zeigt sich, dass die Schwimmtrajektorie des Spermiums stark vom Grad der Chiralität abhängt. In freier Flüssigkeit finden wir einen dynamischen Übergang der Trajektorie zwischen einer ausgeprägten Helix und einer fast geradlinigen Bewegung. In der Nähe einer Wand können wir sowohl die Adhäsion an der Grenzfläche, als auch die orientierte kreisförmige Bewegung reproduzieren. Die Ursache für die Adhäsion an der Wand findet sich interessanterweise in der *Abstoßung* des Flagellums von der Wand. Kreisförmige Bewegung und Richtung werden hingegen von der Chiralität des Spermiums bestimmt.

Zur Untersuchung der Ziliendynamik wird ein Gitter von typischerweise 20 mal 20 Zilien betrachtet, in dem Axonemstrukturen senkrecht auf einer Wand verankert werden. Das Schlagmuster der Zilien wird der biologischen Situation nachempfunden. Dabei ist entscheidend, dass das Schlagmuster durch äußere

Einflüsse modifiziert werden kann, so dass die Entstehung einer Metachronal Wave durch Synchronisation verschiedener Zilien ermöglicht wird. Zum ersten Mal sind wir in der Lage, die Metachronal Wave auf einer ausgedehnten Fläche unabhängig schlagender Zilien in Simulationen zu beobachten. Es zeigt sich, dass die Metachronal Wave gravierende Auswirkungen auf Transportgeschwindigkeit und Effizienz hat. Die durchschnittliche Geschwindigkeit der Flüssigkeit steigt durch die Metachronal Wave um bis zu einem Faktor 3.2 im Vergleich zu einem gleichartigen, synchron schlagenden System. Da gleichzeitig die Leistungsaufnahme sinkt, steigt zudem die Effizienz um bis zu einer Größenordnung. Weiterhin charakterisieren wir Transport und Welleneigenschaften als Funktionen der Schlagrichtung, dem Zilienabstand und der Viskosität der Flüssigkeit. Wir sind überzeugt, dass sowohl die Effizienz als auch im besonderen die Transportgeschwindigkeit entscheidend sind für die Fitness der Zelle. Die Metachronal wave ist daher von großer funktionaler Bedeutung für Zellen mit Zilien.

# Erklärung

Ich versichere, da ich die von mir vorgelegte Dissertation selbständig angefertigt, die benutzten Quellen und Hilfsmittel vollständig angegeben und die Stellen der Arbeit - einschließlich Tabellen, Karten und Abbildungen -, die anderen Werken im Wortlaut oder dem Sinn nach entnommen sind, in jedem Einzelfall als Entlehnung kenntlich gemacht habe; da diese Dissertation noch keiner anderen Fakultät oder Universität zur Prüfung vorgelegen hat; da sie - abgesehen von unten angegebenen Teilpublikationen - noch nicht veröffentlicht worden ist sowie, da ich eine solche Veröffentlichung vor Abschluß des Promotionsverfahrens nicht vornehmen werde. Die Bestimmungen dieser Promotionsordnung sind mir bekannt. Die von mir vorgelegte Dissertation ist von Prof. Dr. G. Gompper betreut worden.